POLITECNICO DI TORINO

Department of Mechanical and Aerospace Engineering

Master's Degree in Aerospace Engineering

Numerical and Experimental Investigation of Small Propellers in Ground Effect

Supervisors:
Prof. Gioacchino Cafiero
Dr. Vincenzo Muscarello
Prof. Pier Marzocca

Student:
Nicoleta Railean
326423

Thesis in collaboration with
RMIT University

Academic Year 2024/2025

Acknowledgements

I would like to express my sincere gratitude to all the people who supported me throughout this thesis and during my academic journey.

I wish to thank Professor **Cafiero** for his guidance throughout this academic path. My deepest and most heartfelt thanks go to Professor **Muscarello**, whose continuous support, insightful advice, and genuine enthusiasm were fundamental to the development of this work. I am especially grateful for the trust he placed in me and for believing in my potential, including encouraging me to present this research at international venues such as the AIAA and ICAS 2026 conferences.

A special acknowledgment goes to **Paul**, whose patience, availability, and constant support played a crucial role in this project. His dedication and willingness to assist at every stage made this experience both motivating and enriching. I am also sincerely grateful to Professor **Marzocca**, for giving me the opportunity to experience one of the most formative and exciting periods of my life by welcoming me to RMIT University in Melbourne.

Finally, I would like to express my gratitude to my *family* and *friends*, including those I met during my university years. Their constant support and encouragement have been an essential source of strength throughout this journey.

This achievement is also yours.

Nicoleta

Abstract

In recent years, the widespread growth of drones and multirotor aircraft has brought renewed attention to the aerodynamic phenomena governing their performance and efficiency. Among these, the *ground effect* plays a crucial role, as it enhances thrust and reduces power consumption when operating near the ground. However, classical formulations, originally developed for rotors used in helicopters, fail to accurately capture the behavior of small fixed-pitch propellers typically employed in modern drone applications.

This thesis investigates the *ground effect* on a small hovering propeller through a combined numerical and experimental approach, representative of the operating conditions of UAVs and eVTOL platforms. Following a comprehensive review of existing theoretical models, a dedicated test bench was designed and built to measure thrust, torque, and power at various distances from the ground. In parallel, a numerical model was developed using the **DUST** code, a mid-fidelity solver capable of reproducing the flow field through a free-vortex formulation.

The analysis reveals a strong dependence of the *ground effect* on the propeller geometry and rotational speed, exhibiting behaviors that deviate significantly from classical correlations. The excellent agreement between experimental measurements and numerical simulations validates the proposed methodology and paves the way for the development of more accurate predictive models for coaxial and multirotor configurations, enabling a more efficient and realistic aerodynamic design of next-generation drones and eVTOL systems.

Sommario

Negli ultimi anni la rapida espansione dei droni e dei velivoli multirotore ha reso sempre più centrale lo studio dei fenomeni aerodinamici che ne determinano le prestazioni e l'efficienza. Tra questi, l'*effetto suolo* riveste un ruolo cruciale, poiché comporta un incremento della spinta e una riduzione della potenza richiesta in prossimità del suolo. Le formulazioni classiche, sviluppate per i rotori impiegati negli elicotteri, non descrivono tuttavia in modo accurato il comportamento delle piccole eliche a passo fisso utilizzate nei droni di nuova generazione.

Questa tesi affronta il problema mediante un'analisi numerica e sperimentale del *ground effect* su una piccola elica in hover, rappresentativa delle configurazioni tipiche di UAV e piattaforme eVTOL. Dopo una revisione dei principali modelli teorici presenti in letteratura, è stato realizzato un banco prova dedicato per misurare spinta, coppia e potenza a diverse altezze dal suolo. Parallelamente, è stato sviluppato un modello numerico con il codice **DUST**, un solutore a media fedeltà capace di riprodurre il campo di moto mediante una formulazione a vortici liberi.

I risultati evidenziano una marcata dipendenza del *ground effect* dalla geometria e dalla velocità di rotazione dell'elica, con comportamenti che si discostano sensibilmente dalle correlazioni classiche. La coerenza tra dati sperimentali e simulazioni numeriche conferma la validità dell'approccio adottato, ponendo le basi per lo sviluppo di modelli più accurati applicabili a configurazioni coassiali e multirotore per una progettazione più efficiente e realistica dei droni eVTOL.

Table of Contents

List of Tables

List of Figures

Chapter 1

Introduction

1.1 Multirotor drones and Hovera

The term *drone* is commonly used to refer to a type of aircraft that does not require a pilot or crew on board. More formally, these vehicles are known as Unmanned Aerial Vehicles (UAVs) and are defined as aerial systems capable of flight without a human occupant. UAVs utilize aerodynamic forces to lift off and navigate through the air, either autonomously or under remote control.

The concept of unmanned flight dates back to the early experiments with remotely controlled aircraft, originally developed for military purposes. Over the decades, UAVs have evolved significantly, encompassing a wide range of sizes, configurations, and capabilities. Modern UAVs are used in a variety of applications, including surveillance, scientific research, and aerial surveying, demonstrating their versatility and rapid technological advancement.

(a) Military Drone

(b) Irrigation Drone

Figure 1.1: Examples of drones with different applications.

To fully understand UAVs, it is useful to classify them according to attributes such as size, flight autonomy, payload, and range. This classification enables a more precise analysis of rotor performance and aerodynamics, which is the focus of the present study on the Hovera drone.

1.1.1 The Hovera eVTOL Platform

The **Hovera** vehicle is an electric Vertical Take-Off and Landing (eVTOL) aircraft developed in 2019 by a multidisciplinary team of students from *RMIT University* (Melbourne, Australia) for the international *GoFly Prize* competition sponsored by Boeing. The objective of the competition was to design a safe, lightweight and highly efficient personal air vehicle capable of carrying a single passenger over a prescribed mission without refuelling or recharging.

Hovera features a distinctive **ducted coaxial contra–rotating propulsion system**, integrated within the central fuselage. This configuration was chosen to enhance aerodynamic efficiency, reduce tip–vortex losses, and increase stability in hover and transition flight. The duct also serves a structural role, providing mechanical protection for the rotors while contributing to thrust augmentation through pressure–recovery effects.

Figure 1.2: Images of the Hovera platform developed by the RMIT student team for the GoFly Prize.

According to the official Hovera progress documentation [1], the vehicle was extensively developed through **additive manufacturing tecniques**. Composite-reinforced polymer components were used for the duct, central hub and several structural interfaces, while the landing system combined 3D-printed joints with lightweight aluminium tubing. This approach enabled rapid prototyping, modularity and reduced production costs.

The digital twin of Hovera (Fig. 1.3) provides a clear representation of the overall architecture: a large central duct enclosing the coaxial rotor system, mounted on a square landing frame equipped with shock absorbers and 3D-printed mechanical joints. The structural configuration reflects the design strategy adopted by the RMIT team to maximise robustness, pilot safety and ease of assembly during testing.

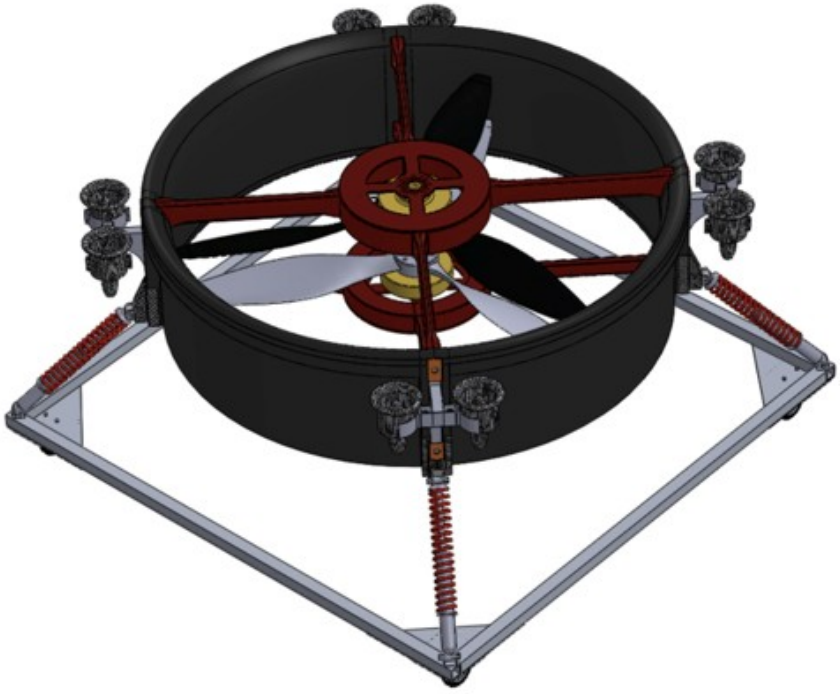

Figure 1.3: Digital twin of the Hovera eVTOL platform as reported in the RMIT GoFly Progress Report [1].

The full-scale prototype of Hovera was built and tested by the RMIT team. However, the COVID-19 pandemic led to the interruption of the GoFly competition, preventing the vehicle from participating in the final flight demonstrations. As

a result, despite the significant progress achieved in design and manufacturing, the aerodynamic behaviour of Hovera in ground effect has never been formally investigated. This gap motivates the present study.

While the available documentation includes CAD models, engineering drawings and high-level configuration data, **the detailed geometry of the coaxial rotors, such as blade twist, airfoil definition, and chord distribution, is not publicly disclosed**. This limitation prevents the direct reconstruction of the propulsion system for mid- and high-fidelity aerodynamic simulations.

For these reasons, this thesis adopts a **surrogate modelling strategy**. Instead of analysing the complete Hovera configuration, the ground-effect behaviour is examined using a **single three bladed propeller** representative of the rotor class employed on the vehicle. This controlled setup enables the isolation of the fundamental physical mechanisms governing thrust augmentation, wake contraction and near-ground flow redistribution.

A first experimental campaign investigates an *open propeller* configuration, followed by a second campaign with a *ducted arrangement*, reproducing the most relevant aerodynamic features of Hovera's architecture. Once validated, the integrated numerical–experimental methodology developed here can be extended to a complete reconstruction of the Hovera rotor system, should the missing blade geometry become available.

1.2 Ground effect

The **ground effect** refers to the aerodynamic phenomenon that occurs when a rotorcraft operates in close proximity to the ground, modifying the induced flow field and the rotor wake structure. As a result, the lift (or thrust) is generally enhanced, and the power required to hover is reduced compared with free-air conditions. While this effect has been extensively studied for conventional helicopters, its manifestation in multirotor unmanned aerial vehicles (UAVs) is significantly more complex due to the presence of additional aerodynamic interactions between rotors and with the airframe.

Classical analytical formulations, such as the Cheeseman–Bennett equation, provide a first-order estimate of the thrust increase in ground effect as a function of rotor height above the ground. However, these models were originally developed for

single rotor helicopters and do not fully capture the intricate flow interactions that arise in multirotor configurations. Conyers *et al.* [2] experimentally assessed the applicability of helicopter based ground effect models to small scale rotorcraft and reported significant deviations, emphasizing that mutual rotor interference and airframe effects introduce additional complexities not accounted for in classical theory.

Recent studies on advanced UAV architectures further demonstrate these limitations. Xu *et al.* [3] investigated coaxial counter-rotating propeller systems in eVTOL vehicles and showed that ground proximity strongly influences lift distribution and overall efficiency. Similarly, Li *et al.* [4] performed experimental analyses on ducted coaxial rotor UAVs, revealing that both thrust and hover performance are highly sensitive to ground clearance. These works highlight that the ground effect in multirotor and ducted configurations constitutes a distinct aerodynamic regime, requiring dedicated investigation rather than direct extrapolation from helicopter theory.

For large UAVs such as *Hovera*, understanding and accurately modeling the ground effect is crucial and is therefore central to the present research. Reliable prediction of this phenomenon enables more accurate estimation of aerodynamic performance, supports design optimization, and ensures safe and efficient operation during take-off, landing, and low altitude flight.

1.2.1 Approaches to the Study of Ground Effect in multirotor UAVs

The investigation of ground effect in multirotor UAVs has been approached through both experimental and numerical methods, each providing complementary insights. Experimental studies allow direct measurement of thrust, power consumption, and flow characteristics in controlled laboratory conditions, while numerical simulations enable detailed analysis of the flow field and aerodynamic interactions that are difficult to capture experimentally.

Conyers et al. [2] conducted an experimental study on small-scale rotorcraft operating in ground effect. Their measurements quantified the thrust increase and revealed significant deviations from classical helicopter models, providing essential reference data for the validation of numerical simulations. This work underscores the importance of combining experimental tests with CFD or other computational methods to achieve accurate predictions of ground effect phenomena in multirotor UAVs.

On the numerical side, computational fluid dynamics (CFD) and lattice Boltzmann methods (LBM) have been widely used to simulate rotorcraft in ground effect. Xu et al. [3] performed CFD analyses on coaxial contra-rotating propellers in eVTOL vehicles, revealing how ground proximity alters lift distribution and efficiency. Similarly, Delgado-Gutiérrez et al. [5] applied a GPU-accelerated Lattice Boltzmann Method to simulate fluid flows in irregular domains, achieving high computational performance. Combining experimental measurements with mid-fidelity numerical simulations provides an effective framework to validate aerodynamic models, investigate flow structure interactions, and improve the understanding of near-ground phenomena relevant to UAVs such as *Hovera*.

Since no small-scale prototype of the *Hovera* UAV is currently available, the investigation of the ground effect was carried out through a simplified experimental setup based on a single three-bladed propeller. This approach enabled a controlled analysis of the aerodynamic behavior in ground proximity, isolating the influence of key parameters such as pitch, clearance, and rotational speed. The study was first conducted on an *open propeller* configuration, to characterize the isolated aerodynamic response and validate the numerical predictions against experimental measurements. Subsequently, the analysis was extended to a *ducted propeller* arrangement, allowing a more representative assessment of the aerodynamic behavior of the *Hovera* UAV, whose configuration integrates coaxial counter-rotating rotors within a duct.

Numerically, the simulations were performed using DUST, a mid-fidelity potential flow solver developed at Politecnico di Milano, which provides an efficient and physically consistent representation of rotor aerodynamics while preserving a low computational cost. The experimental measurements, conducted under comparable operating conditions, were used to validate the numerical results and assess the solver's capability to capture the main trends of the ground effect. Once validated on the open and ducted propeller test cases, this combined numerical and experimental methodology can be confidently extended to the complete *Hovera* UAV configuration, supporting the analysis and optimization of its aerodynamic performance in near-ground flight regimes, where safety margins and thrust efficiency are most critical.

Chapter 2

Theoretical models for the study of propellers

In this chapter, the main theoretical models employed for the study of propeller performance are described. The discussion begins with the three classical models for propeller performance: *Momentum Theory*, *Blade Element Theory* and *Blade Element Momentum Theory*, which form the foundation for analyzing rotor thrust and torque. In addition, more advanced formulations based on *Vortex Theory* are introduced, providing a higher-fidelity description of the induced flow and wake dynamics. Subsequently, models specifically developed to investigate *ground effect*, such as the Cheeseman–Bennett formulation and Lighthill's approach, are presented and discussed in relation to experimental evidence available in the literature.

The chapter then proceeds to outline the main propeller configurations and the aerodynamic advantages of ducted designs, with particular attention to coaxial contra-rotating rotors, as featured in the Hovera UAV. Throughout the discussion, reference is made to previous experimental and numerical studies, highlighting the discrepancies between theoretical predictions and observed performance.

2.1 Momentum Theory – Actuator Disk Theory

The theoretical study of propeller performance dates back to the 19th century. In 1865, Rankine formulated the *Momentum Theory*, which models the thrust generated by a propeller as the reaction to the acceleration of air in the opposite direction, in accordance with Newton's Third Law [2]. This approach represents the propeller as a thin disk of diameter D across which the air velocity and pressure increase.

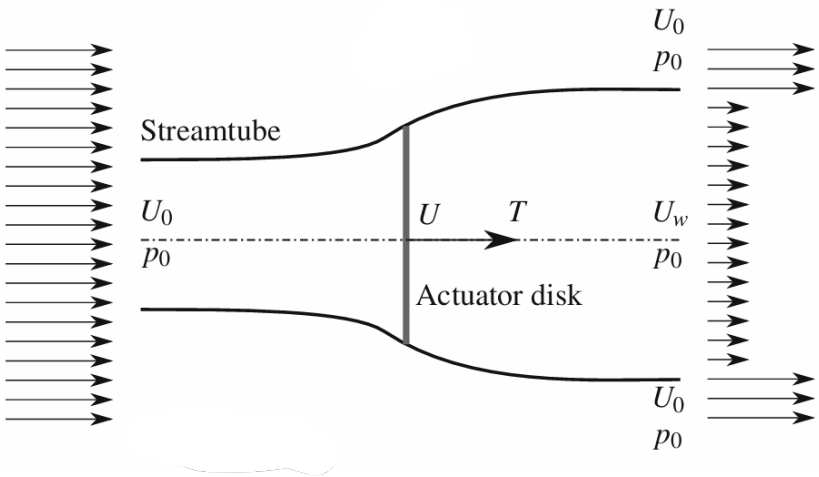

Figure 2.1: Idealized flow through an actuator disk according to Momentum Theory [6].

The main assumptions of the theory are:

1. The flow is steady, incompressible, and inviscid.
2. The flow through the actuator disc is uniform.
3. The disc is infinitely thin and induces no rotation in the wake.
4. Far upstream and downstream, the flow is undisturbed by the rotor.

Under these hypotheses, Bernoulli's equation can be applied on both sides of the actuator disk, leading to the following relations [6]:

$$p_0 + \frac{1}{2}\rho U_0^2 = p_+ + \frac{1}{2}\rho U^2 \tag{2.1}$$

$$p_- + \frac{1}{2}\rho U^2 = p_w + \frac{1}{2}\rho U_w^2 \tag{2.2}$$

Assuming the far-wake pressure equals the freestream value ($p_0 = p_w$), the resulting jump across the disk is:

$$\Delta p = p_+ - p_- = \frac{1}{2}\rho \left(U_0^2 - U_w^2\right) \tag{2.3}$$

By applying mass and momentum conservation on control volumes before and after the disk, the thrust T produced by the propeller is expressed as:

$$T = \dot{m}(U_0 - U_w) = \rho A U (U_0 - U_w) \tag{2.4}$$

where U_0 is the upstream freestream velocity, U_w is the far-wake velocity, U is the rotor velocity, A is the disk area, and $\dot{m}$ is the mass flow rate through the disk.

From energy conservation, the power extracted by the actuator disk is:

$$P = \frac{1}{2}\dot{m}\left(U_0^2 - U_w^2\right) \tag{2.5}$$

This can also be expressed as the work rate of the thrust:

$$P = TU = \dot{m}(U_0 - U_w)\, U \tag{2.6}$$

Equating these two expressions allows solving for the *rotor velocity*:

$$U = \frac{U_0 + U_w}{2} \tag{2.7}$$

This result shows that the rotor velocity is the mean between the freestream and far-wake velocities. **Momentum Theory** thus provides a **simple global estimate of thrust and power**, but it neglects blade geometry, viscous effects, and non-uniform inflow. These simplifications limit its applicability for detailed design or for analyzing complex multirotor interactions.

2.2 Blade Element Theory (BET)

The *Blade Element Theory (BET)*, introduced by *S. Drzewiecki* and *W. Froude* in 1909, was developed to overcome the limitations of Momentum Theory. Unlike Momentum Theory, which provides only a *global estimate* of thrust and power, BET allows for a *local analysis* of aerodynamic forces along the blade span [7].

In this approach, a blade is divided into infinitesimal elements of radial length dr and chord $c(r)$ located at a distance r from the rotation axis. Each element has a *relative velocity* U_{rel}, which can be decomposed into:

- a *normal component* U_n, perpendicular to the rotor disk,
- a *tangential component* U_t, lying in the rotor plane.

The kinematics of the blade element are described through a velocity triangle, which defines three angles:

- the **flow angle** φ, between the relative velocity and the rotor plane,
- the **twist angle** θ, between the chord line and the rotor plane,
- the resulting **angle of attack** $\alpha = \varphi - \theta$.

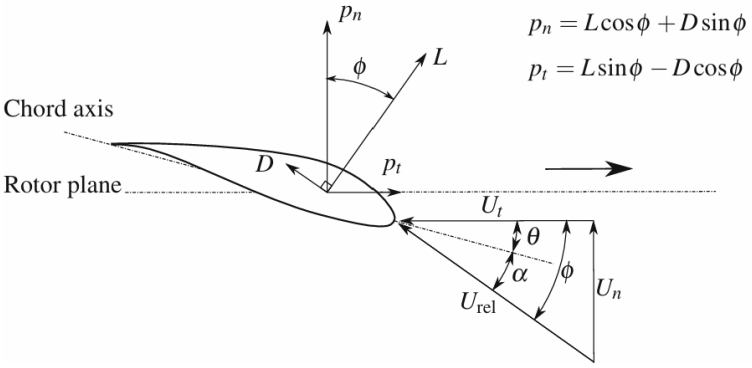

Figure 2.2: Blade velocity triangle and resulting aerodynamic forces [7].

Unlike Momentum Theory, which treats the propeller as an ideal actuator disk and neglects blade geometry, BET explicitly incorporates:

- the *local blade geometry* (chord distribution $c(r)$ and twist $\theta(r)$),
- the *aerodynamic characteristics* of the airfoil sections (lift and drag coefficients as functions of α),
- the integration of sectional forces along the span to obtain total thrust and torque.

For each blade element of surface $dS = c(r)dr$, the lift and drag forces are given by:

$$dL = \tfrac{1}{2}\rho U_{rel}^2\, c(r)\, C_l(\alpha)\, dr, \tag{2.8}$$

$$dD = \tfrac{1}{2}\rho U_{rel}^2\, c(r)\, C_d(\alpha)\, dr, \tag{2.9}$$

where $U_{rel} = \sqrt{U_t^2 + U_n^2}$ is the local relative velocity.

Projecting these forces onto the rotor axis (thrust direction) and onto the tangential direction (responsible for torque), the following expressions are obtained:

$$dT = dL\cos\varphi - dD\sin\varphi, \tag{2.10}$$

$$dQ = r\,(dL\sin\varphi + dD\cos\varphi). \tag{2.11}$$

Substituting dL and dD, the elemental contributions become:

$$dT = \tfrac{1}{2}\rho U_{rel}^2\, c(r)\Big[C_l(\alpha)\cos\varphi - C_d(\alpha)\sin\varphi\Big]dr, \tag{2.12}$$

$$dQ = \tfrac{1}{2}\rho U_{rel}^2\, c(r)\, r\Big[C_l(\alpha)\sin\varphi + C_d(\alpha)\cos\varphi\Big]dr. \tag{2.13}$$

The total thrust and torque of the rotor are then obtained by integrating along the blade span and multiplying by the number of blades B:

$$T = B\int_0^R dT, \tag{2.14}$$

$$Q = B\int_0^R dQ. \tag{2.15}$$

The overall procedure based on BET can be summarized as follows:

1. The blade geometry is specified through the chord distribution $c(r)$ and the twist angle $\theta(r)$.
2. The aerodynamic coefficients $C_L(\alpha)$ and $C_D(\alpha)$ of the airfoil sections are provided.
3. The inflow components (U_t, U_n), the flow angle φ and the angle of attack $\alpha = \varphi - \theta$ are determined.
4. The elemental thrust dT and torque dQ are evaluated at each blade section.
5. The total thrust T and torque Q are obtained by integration along the blade span and multiplication by the number of blades B.

Blade Element Theory provides a detailed local analysis of aerodynamic forces along the blade, accounting for blade geometry and airfoil characteristics. However, it requires knowledge of the induced velocity distribution U_n (or equivalently the inflow angle φ), which is not provided by the theory itself. For this reason, BET is often combined with Momentum Theory, leading to the *Blade Element Momentum Theory (BEMT)*.

2.3 Blade Element Momentum Theory (BEMT)

The *Blade Element Momentum Theory (BEMT)* was first introduced in the early twentieth century by Froude and later refined by Glauert, with the aim of providing a more complete description of rotor aerodynamics. Classical *momentum theory* models the rotor as an actuator disk and offers simple global estimates of thrust and power, but it does not take into account blade geometry or airfoil properties. In contrast, *blade element theory* considers the shape of the blades, their twist, and airfoil data, but it requires the inflow distribution as input. By combining the global balance from momentum theory with the sectional formulation of blade element theory, BEMT achieves a self-consistent determination of the inflow distribution and, as a result, enables the calculation of the rotor's thrust, torque, and power coefficients [8], [9].

In the BEMT formulation, the induced flow is described by two dimensionless induction factors: the *axial* factor a and the *tangential* factor a'. The inflow ratio is $\lambda = U_n/(\Omega R)$, with U_n the local axial velocity through the disk, and the radial coordinate is nondimensionalized as $r = \tilde{r}/R$, with $r \in [0,1]$; by convention, $r = 0$ at the hub and $r = 1$ at the tip. The local velocity components then read:

$$U_n = U_0\,(1 - a), \qquad U_t = \Omega R\, r\,(1 + a'), \tag{2.16}$$

where U_0 is the free-stream speed and Ω is the rotor angular speed. The inflow angle is defined as $\varphi = \arctan\Big(U_n/U_t\Big)$, and the angle of attack is $\alpha = \theta(r) - \varphi$, with $\theta(r)$ the local pitch.

In the **theoretical formulation of BEMT**, the rotor disk is divided into annular elements of thickness dr. On each annulus, the thrust increment is expressed in two different ways:

1. *From Blade Element Theory (BET):*

$$dC_T = dC_L \cos\varphi - dC_D \sin\varphi, \tag{2.17}$$

   where dC_L and dC_D are the sectional lift and drag contributions, and φ is the inflow angle.

2. *From Momentum Theory:*

$$dC_T = 4\lambda a r\, dr, \tag{2.18}$$

   with λ the inflow ratio and a the axial induction factor.

Equating these two expressions provides the equilibrium condition for the inflow distribution. In hover, where the climb inflow $\lambda_c = 0$, the solution reduces to [10]:

$$\lambda(r) = \frac{\sigma\, a_0}{16}\left[\sqrt{1 + \frac{32\,\theta(r)\,r}{\sigma\, a_0}} - 1\right] \tag{2.19}$$

where $\sigma = \frac{B\,c}{\pi R}$ is the rotor solidity (B blades, chord c, radius R), and a_0 is the two-dimensional lift-curve slope of the airfoil section (distinguished from the axial induction factor a).
Once $\lambda(r)$ is determined, the global aerodynamic coefficients are obtained by integration along the blade span. The thrust coefficient is:

$$C_T = \int_0^R dC_T\, dr, \tag{2.20}$$

The differential power coefficient is expressed as the sum of two contributions [10]:

$$dC_P = \lambda\, dC_T + \frac{\sigma C_d}{2}\, r^3\, dr, \tag{2.21}$$

Integrating along the span yields the total power coefficient:

$$C_P = \int_0^R dC_P\,. \tag{2.22}$$

Beyond these integral forms, a landmark analytical result was obtained by Glauert (1935) for the optimum actuator-disk loading in hover via a variational approach; this classical result has been revisited and extended by Tyagi & Schmitz (2025), who derived exact closed-form integrals for thrust and bending-moment coefficients, and an expression for the maximum power coefficient as a function of tip-speed ratio [11]. These findings confirm the historical importance of BEMT while also illustrating its fundamental limitations when compared to higher-fidelity approaches.

2.4 Vortex Methods

Although BEMT provides a practical balance between simplicity and accuracy, it is intrinsically limited by its assumption of axisymmetric and steady inflow, as well as by the use of empirical corrections. For more accurate predictions of rotor aerodynamics, especially in modern applications such as eVTOL vehicles and UAVs, vortex-based methods have become a widely adopted alternative [12].

These methods explicitly model the blade-bound circulation and the vortical wake shed by the rotor, thus enabling the prediction of non-uniform and unsteady inflow distributions. The fundamental relations are given by the *Kutta–Joukowski theorem*, which links the sectional lift to circulation

$$L' = \rho U_{\text{rel}}\,\Gamma \tag{2.23}$$

where L' is the lift per unit span, ρ the fluid density, U_{rel} the relative velocity seen by the blade element, and Γ the circulation around the section. The induced velocity field of vortex filaments is instead determined by the *Biot–Savart law*:

$$\mathbf{u}(\mathbf{x}) = \frac{1}{4\pi}\int_{\text{wake}} \frac{\Gamma\, d\boldsymbol{\ell} \times (\mathbf{x} - \mathbf{x}')}{|\mathbf{x} - \mathbf{x}'|^3}. \tag{2.24}$$

In numerical implementations, this expression is discretized into straight vortex segments. For a single segment, the induced velocity is given by the Biot–Savart relation reported in [13]:

$$\mathbf{V}_{\text{ind}} = \frac{\Gamma}{4\pi}\frac{(\mathbf{r}_1 + \mathbf{r}_2)\,(\mathbf{r}_1 \times \mathbf{r}_2)}{r_1 r_2 + \mathbf{r}_1 \cdot \mathbf{r}_2}, \tag{2.25}$$

where Γ is the strength of the vortex filament and $\mathbf{r}_1$, $\mathbf{r}_2$ are the distance vectors from the beginning and the ending of the vortex segment to the arbitrary evaluation point P, respectively (as reported in Anderson [13]).

In time-marching vortex-particle methods (VPM), the wake is represented by discrete particles whose positions are updated at each timestep according to the local convection velocity. This velocity includes contributions from the free-stream, from the self-induced motion of the particle, and from the velocity field induced by the rest of the wake. The governing relation is expressed as

$$\frac{d\mathbf{x}_i(t)}{dt} = \mathbf{u}(\mathbf{x}_i, t), \tag{2.26}$$

where $\mathbf{u}(\mathbf{x}_i, t)$ denotes the total velocity acting on the i-th particle [12]. This formulation provides a consistent way to simulate the roll-up and convection of the rotor wake in time.

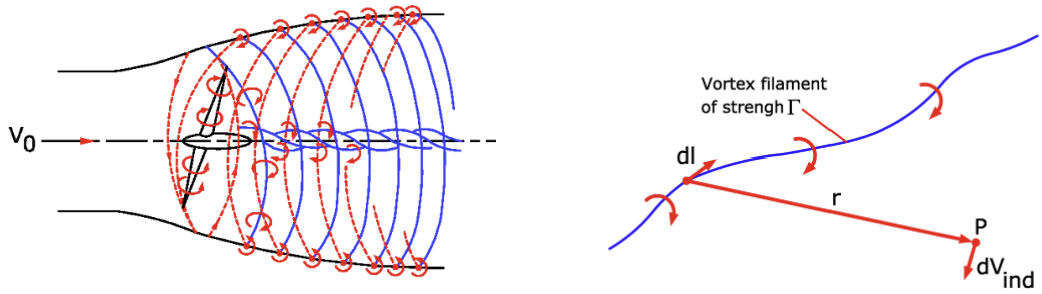

(a) Vortex wake. (b) Schematic for the Biot–Savart law.

Figure 2.3: Vortex wake behind the rotor blades, adapted from Hansen (a) and schematic for the Biot–Savart law adapted from Anderson (b) (as reported in [13]).

In prescribed-wake formulations, different levels of fidelity can be achieved depending on the blade and wake representation:

- *Lifting line models*, where each blade is represented as a bound vortex line, with trailing vortices shed into the wake.
- *Lifting surface models*, in which the blade is represented as a surface discretized into panels with distributed circulation.
- *Panel methods*, where both blade and wake are described by vortex ring elements, providing the highest fidelity among prescribed approaches.

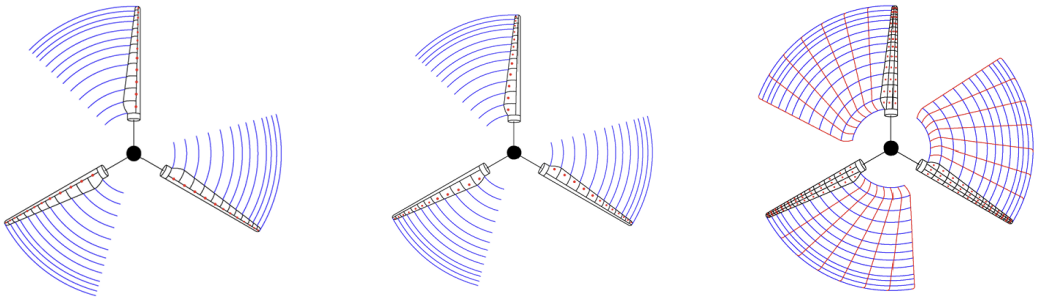

(a) Lifting line model. (b) Lifting surface model. (c) Panel method.

Figure 2.4: Schematic of prescribed wake models as reported in [13].

The same article also illustrates the corresponding blade and wake representations for each approach, highlighting how the bound circulation is modeled on the blade and how vortices are shed into the wake.

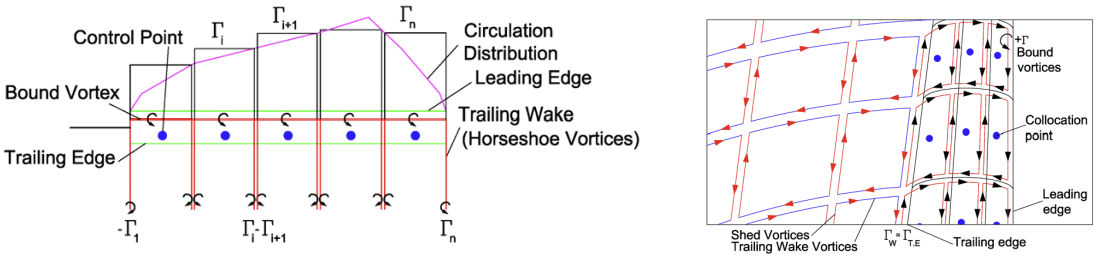

(a) Lifting surface model. (b) Panel method.

Figure 2.5: Schematic of blade and wake representation [13].

Beyond these representations, vortex methods are generally classified by the treatment of the wake geometry:

- *Prescribed-wake methods*, where the wake geometry is imposed. These methods are computationally efficient but less accurate in complex flow conditions.

- *Free-wake methods*, where the wake geometry evolves freely under the Biot–Savart law. This provides higher fidelity in predicting inflow and unsteady loads but at increased computational cost.

- *Hybrid or time-marching methods*, which combine prescribed initialization with subsequent free evolution, balancing efficiency and accuracy.

These approaches form the basis of modern vortex solvers for rotor aerodynamics. Lee et al. (2022) reviewed the state of the art in this field, emphasizing the central role of vortex methods in the design and analysis of eVTOL configurations [12].

Within this context, the mid-fidelity solver *DUST*, developed at Politecnico di Milano, represents a practical implementation of vortex-based methods. It couples a Vortex Lattice Method (VLM) for lifting surfaces with a Vortex Particle Method (VPM) for wake evolution, providing an efficient yet accurate framework to investigate complex rotor–wake interactions and aeroelastic coupling.

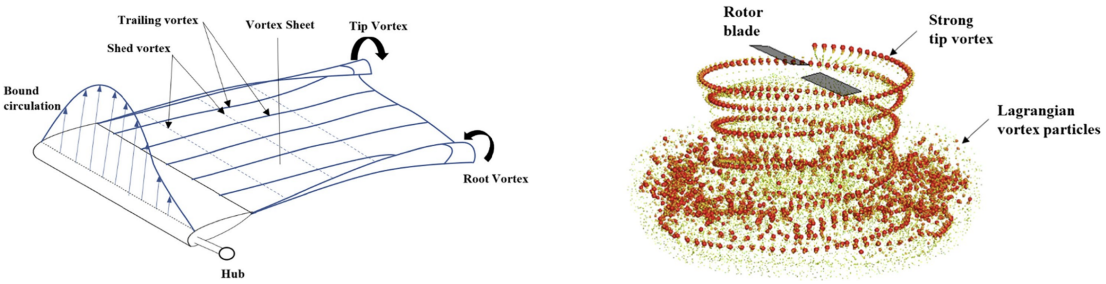

(a) Rotor wake model using FWM. (b) Rotor wake modeling using VPM.

Figure 2.6: Free–wake (FWM) and vortex–particle (VPM) wake modeling approaches from [12].

The effectiveness of VPM in capturing unsteady wake dynamics is illustrated in Fig. 2.7, which shows the progressive roll-up of tip vortices over successive rotor revolutions [12].

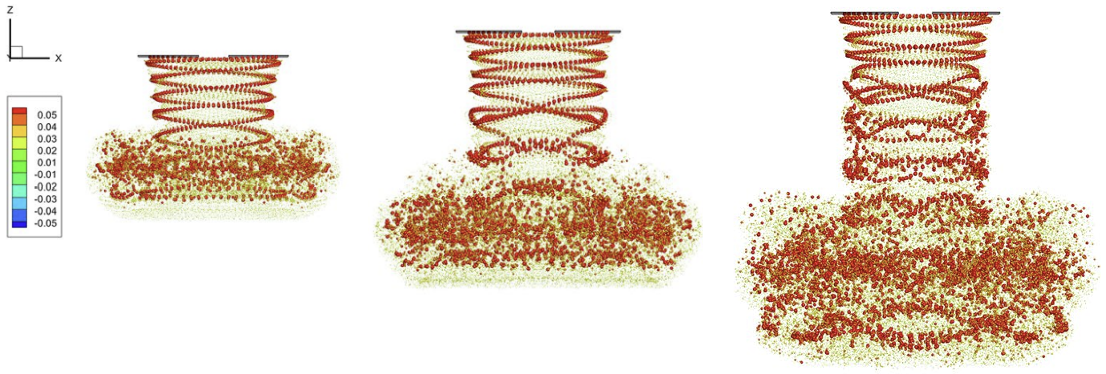

(a) 10 revolutions (b) 15 revolutions 20 revolutions

Figure 2.7: Evolution of rotor wake structures predicted with VPM [12].

Such accuracy is particularly relevant in the present thesis, where *DUST* will be employed to study the **ground effect** on the hovering propeller of the *Hovera*. By modeling the ground through the *method of images*, a physically consistent treatment of the wake–ground interaction can be achieved, while avoiding numerical instabilities typical of direct free-wake simulations.

2.5 Ground Effect models

The *ground effect* is a well-known aerodynamic phenomenon that occurs when a rotor operates in proximity to a solid boundary. As the rotor approaches the ground, the induced velocity is reduced and the effective thrust is enhanced, leading to improved aerodynamic efficiency. This effect is of particular importance in helicopters, drones, and eVTOL vehicles, as it strongly influences power requirements, stability, and control during hover and landing phases [14].

Experimental studies confirm the strong impact of ground effect on rotorcraft performance. For small-scale UAVs, Conyers et al. (2018) performed empirical measurements showing that the thrust increase near the ground does not always follow the predictions of classical analytical models, especially for multi-rotor drones [2]. This highlights the need for refined models and dedicated validation in drone applications.

From a modeling perspective, several analytical formulations have been proposed to quantify the effect of ground proximity. The classical Cheeseman-Bennett model (1957) is among the most widely adopted, expressing the thrust increment as a function of the rotor height-to-diameter ratio. However, as pointed out by Georgiev (2025), alternative models exist, including those of Zbrozek (1954), Hayden (1962), and the UMD formulation, each of which is better suited to specific ranges of collective pitch or rotor operating conditions [10]. Figure 2.8 illustrates the characteristic flow field generated by a rotor in hover, both out of ground effect (OGE) and in ground effect (IGE).

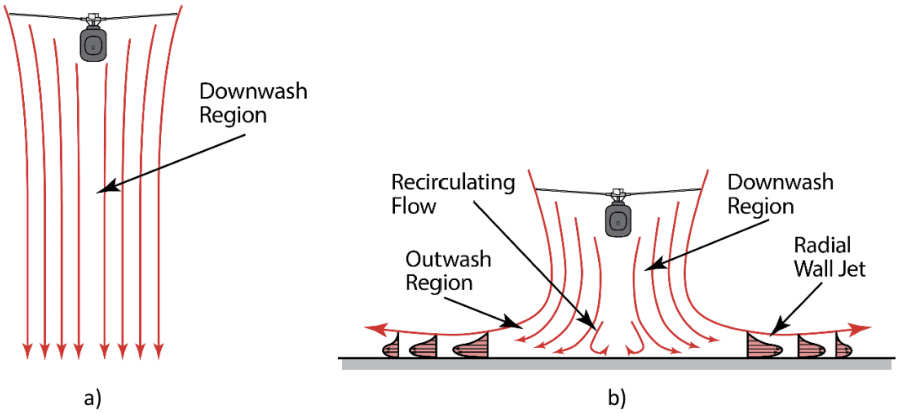

Figure 2.8: Wake from a hovering rotor: (a) out of ground effect (OGE) and (b) in ground effect (IGE) [3].

The qualitative flow features shown in Figure 2.8 provide the physical basis for analytical and semi-empirical models of ground effect, which aim to predict the induced velocity and thrust variations as a function of rotor height.

In his study, Georgiev applied a Blade Element Momentum Theory (BEMT) framework at low Reynolds numbers, comparing these models against experimental data and showing that no single formulation is universally valid, though the Cheeseman-Bennett model remains a robust baseline. A further contribution to the theoretical understanding of ground effect was given by Lighthill (1979), who introduced a simplified fluid flow model. In his formulation, ground effect is described as a perturbation of the induced velocity field caused by the presence of the solid boundary, thus linking vortex theory to ground interference effects [15].

2.6 Cheeseman Bennett model

Among the analytical models proposed to quantify the influence of ground proximity, the formulation by Cheeseman and Bennett (1957) is by far the most widely adopted. It expresses the thrust increment in ground effect as

$$\frac{T_{IGE}}{T_{OGE}} = \frac{1}{1 - \left(\frac{R}{4h}\right)^2}, \tag{2.27}$$

where T_{IGE} and T_{OGE} denote the thrust in ground effect and out of ground effect, R is the rotor radius, and h is the hub height above ground.

However, as emphasized by Conyers et al. [2], this model relies on assumptions that are strictly valid for conventional helicopters: a single rotor with uniform blades, constant rotational speed, and collective pitch control. Such assumptions are not met in multirotor UAVs, which typically employ fixed-pitch propellers operating at variable rotational speeds, with tapered geometries that alter both angle of attack and chord distribution.

For these vehicles, the Cheeseman–Bennett model often fails to reproduce the actual thrust increase in ground effect, and alternative formulations based on power consumption have been proposed [2]. Their model assumes a constant thrust condition (balancing the aircraft weight) and relates the power as

$$\frac{P_{IGE}}{P_{OGE}} = \frac{\omega_{OGE}}{\omega_{IGE}}, \tag{2.28}$$

where P_{IGE} and P_{OGE} are the power requirements in and out of ground effect, and ω_{IGE}, ω_{OGE} are the induced velocities in the two conditions. This formulation is especially relevant for electric multirotors, where the constant thrust assumption naturally holds due to the absence of fuel consumption and the steady weight during hover.

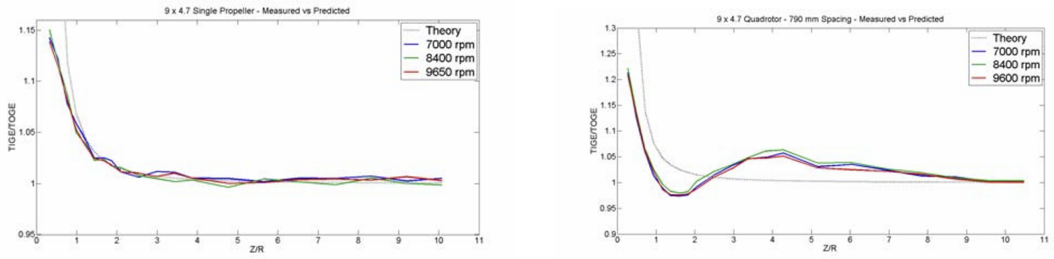

(a) Single isolated propeller. (b) Quadrotor configuration.

Figure 2.9: Comparison of ground-effect performance for different rotorcraft configurations [2].

As shown in Fig. 2.9, the thrust behavior in ground effect depends strongly on the rotor configuration. For a single isolated propeller, the experimental trend already follows the general shape predicted by the Cheeseman–Bennett model, although noticeable deviations appear when the rotor operates below $h/R = 0.25$, which represents the theoretical validity limit of the model. In contrast, for the quadrotor case, the discrepancy with the Cheeseman–Bennett prediction is much larger: the experimental curves diverge significantly, highlighting that the classical model is not valid for multirotor UAVs without corrective formulations.

2.6.1 Alternative ground effect models

A more detailed comparison of analytical formulations is provided by Georgiev (2025), who applied a Blade Element–Momentum Theory (BEMT) framework at low Reynolds numbers. His study compares the Cheeseman–Bennett relation with the alternative models of Zbrozek (1954), Hayden (1962), and the UMD formulation, under different collective pitch angles. As shown in Fig. 2.10, the correlation between analytical predictions and experimental data depends strongly on the collective pitch angle. According to Georgiev [10], the Hayden model is more suitable for inflow correction at low collective pitch values ($\theta < 18°$), while the Cheeseman–Bennett model provides a better fit for higher pitch angles ($\theta > 18°$), particularly under extreme ground-effect conditions.

This highlights that the validity of ground effect models is not universal; instead, it depends on both blade loading and flight regime.

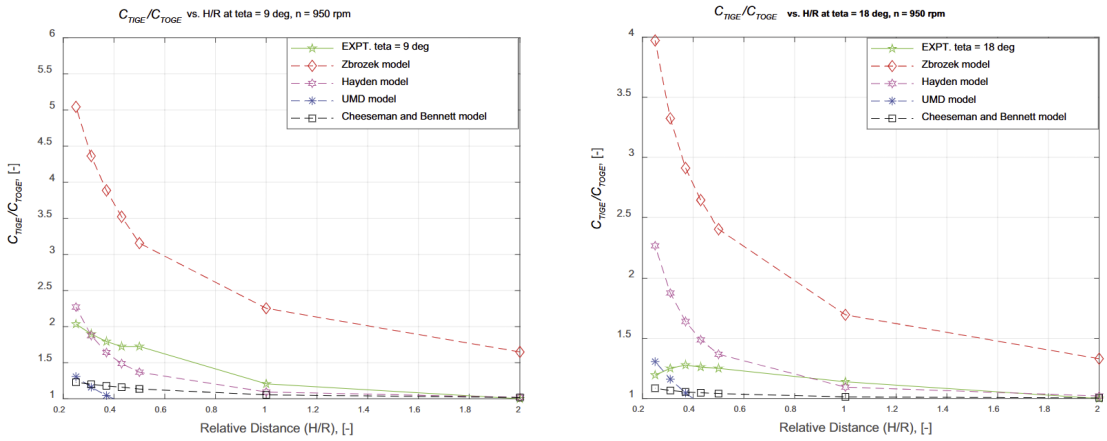

(a) $\theta = 9°$. (b) $\theta = 18°$.

Figure 2.10: Relative thrust coefficient in ground effect versus h/R, experimentally derived and empirically evaluated at two collective pitch angles [10].

2.6.2 Ground effect formulations for drones and eVTOLs

Building on the observations of Georgiev [10], who showed that the accuracy of classical ground-effect models depends strongly on the operating regime, Sánchez-Cuevas et al. (2017) [16] extended this line of research to multirotor UAVs.

Through an experimental campaign on two quadrotor platforms (PQUAD and AMUSE), they explicitly analyzed how ground proximity modifies thrust generation and, starting from the Cheeseman–Bennett relation, proposed an analytical extension based on potential flow and the method of images. This formulation incorporates the mutual interference of the four coplanar rotors, leading to the following expression:

$$\frac{T_{IGE}}{T_{OGE}} = \frac{1}{1 - \left(\frac{R}{4z}\right)^2 - R^2 \frac{z}{(d^2+4z^2)^{3/2}} - \frac{R^2}{2} \frac{z}{(2d^2+4z^2)^{3/2}}}, \tag{2.29}$$

where R is the rotor radius, z the hub height above the ground, and d the distance between adjacent rotor axes. The additional terms capture the aerodynamic interference in ground effect (the *fountain effect*), which increases thrust relative to the

single-rotor case.

As shown in Fig. 2.11, the single-rotor measurements (red error bars) follow the general trend predicted by the Cheeseman–Bennett relation (black dashed line), although the model slightly overestimates the thrust increment at very low altitudes.

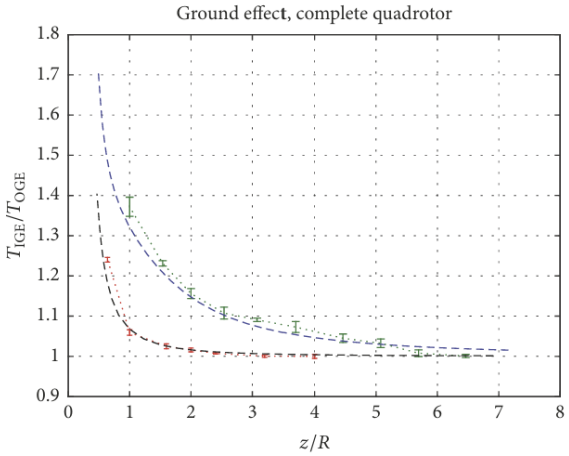

(a) Full quadrotor in ground effect: comparison between theory and experiments.

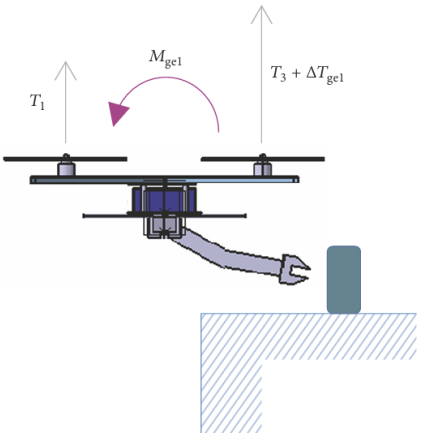

(b) Multirotor under partial ground effect.

Figure 2.11: Experimental and theoretical evaluation [16].

For the full quadrotor configuration (green error bars), the thrust increase is substantially larger due to rotor–rotor interference and the extended potential-flow formulation (blue dashed line) captures this behavior with good accuracy over most of the h/R range, but still underpredicts the measurements at small clearances, where additional mechanisms such as the fountain effect become dominant.

An additional phenomenon analyzed by Sánchez-Cuevas et al. (2017) [16] is the *partial ground effect*, typical of multirotors. Here only a subset of the rotors is influenced by ground proximity, as schematically illustrated in Fig. 2.11(b) of their work. A rotor closer to the ground (e.g., rotor 3) generates an extra thrust increment ΔT_{ge1}, which induces an asymmetric moment M_{ge1}. This unbalanced loading modifies the trim and can degrade stability, underlining the need to account for partial ground-effect conditions in multirotor control.

The response of the quadrotor under partial ground-effect conditions is illustrated in Fig. 2.12(a), where the PQUAD platform was intentionally tilted so that only a subset of the rotors interacted with the ground.

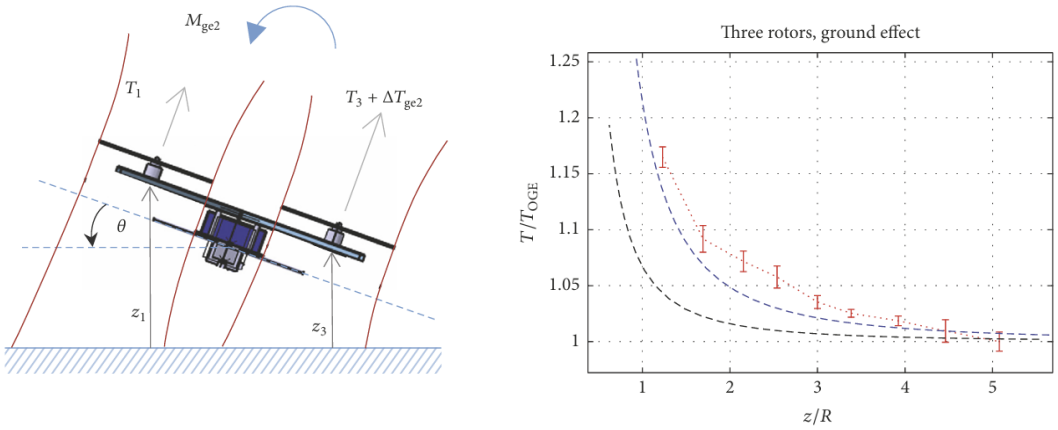

(a) Quadrotor response to partial ground effect (adapted from Fig. 9 in [16]).

(b) Increment in thrust for three rotors near the ground (red error bars), compared with PFI predictions for a single rotor (black dashed line) and for three rotors (blue dashed line) [16].

Figure 2.12: Partial ground-effect investigation: dynamic test configuration and corresponding results.

Two configurations were examined: one with a single rotor affected by ground proximity, and another with three rotors simultaneously influenced, the latter representing a realistic partial-support scenario.

Results for the three-rotor configuration show that partial ground effect enhances thrust compared to the single-rotor case, though with a lower amplification than in the fully symmetric quadrotor condition. The comparison with the potential-flow image (PFI) models further confirms this behavior: the experimental data (red error bars in Fig. 2.12(b)) lie above both the single-rotor (black dashed line) and the three-rotor predictions (blue dashed line), indicating that the measured effect was stronger than expected from the analytical model. This discrepancy is likely due to additional flow recirculation and rotor–wake interactions not captured by the potential-flow approximation.

Overall, these findings highlight that partial ground effect must be considered in multirotor modeling, as the resulting asymmetric thrust increments introduce moments that can strongly affect stability and control in realistic flight scenarios.

2.6.3 Lighthill's simplified fluid flow model

Beyond the previously discussed empirical models, a significant theoretical contribution to the understanding of ground effect was provided by Lighthill (1979).

He reformulated the actuator disk theory to account for the presence of the ground, treating the solid boundary as a mirror plane that reflects the rotor wake. This *image system* modifies the induced velocity distribution and, consequently, the rotor thrust, offering a simplified yet rigorous interpretation of the ground effect [15]. A central outcome of this formulation is the definition of the induced power coefficient, expressed as the ratio between the induced power in ground effect and in free hover:

$$c_p = \frac{P_{IGE}}{P_{OGE}} = f\left(\frac{h}{s}\right) \tag{2.30}$$

This formulation allows the effect of ground proximity to be quantified in terms of the additional energetic advantage gained by the rotor in hover, for support of a fixed weight W. The parameter is studied as a function of the nondimensional height-to-span ratio h/s, where h is the rotor height above ground and s the semi span of the actuator disk. Figure 2.13 shows the predicted behavior of c_p according to Lighthill's model, compared with helicopter data reported by Zbrozek (1950). The results highlight the progressive reduction of induced power as the rotor approaches the ground, consistent with experimental evidence.

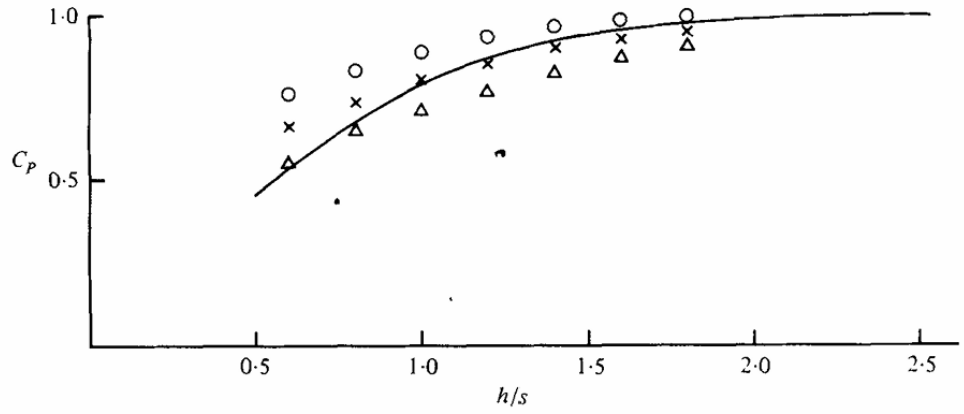

Figure 2.13: Induced power ratio in ground effect as a function of height-to-semi-span ratio h/s. Comparison between Lighthill's theoretical model and helicopter data from Zbrozek (1950) [15].

Although less immediately practical than correlations such as Cheeseman–Bennett, Lighthill's model provides a valuable theoretical foundation, explaining the power reduction in ground effect as a direct consequence of induced–velocity perturbations caused by the ground boundary.

2.7 Rotor Configurations and Duct Effects

The configuration of lifting rotors plays a decisive role in determining the aerodynamic behavior and overall efficiency of rotorcraft. According to their arrangement and level of integration, different solutions have been developed, ranging from classical single-rotor systems to coaxial contra-rotating layouts, ducted rotors, and multirotor ducted architectures. Each configuration presents specific aerodynamic advantages and limitations, which are especially relevant in UAV and eVTOL applications [3], [17], [18], [19], [20].

2.7.1 Open Rotor Configurations

The single main rotor configuration, typical of classical helicopters, is the simplest arrangement from an aerodynamic perspective. It provides lift and thrust from a single actuator disk, but requires a tail rotor or equivalent anti-torque device to balance the reactive moment. While efficient at large scales, this solution is less practical for UAVs due to stability and control issues, and is therefore rarely adopted in multirotor configurations [21].

Figure 2.14: Schematic of a quiet single-main rotor helicopter configuration (adapted from Johnson [21]).

2.7.2 Coaxial Contra-Rotating Rotors

The coaxial counter-rotating configuration consists of two rotors mounted on the same axis, rotating in opposite directions. This arrangement eliminates the reactive torque on the fuselage, removing the need for a tail rotor and thereby allowing a more compact configuration compared to single-main-rotor helicopters. In addition, the opposite rotation of the blades partially recovers the swirl losses in the wake, leading to a higher hovering efficiency and improved thrust-to-disk-area ratio [3]. These features make coaxial rotors particularly attractive for applications where vertical take-off capability must be combined with limited ground footprint, such as urban air mobility vehicles and UAVs.

Nevertheless, coaxial rotors also present notable aerodynamic and structural challenges. The strong aerodynamic interaction between the upper and lower rotors modifies the lift distribution and generates complex unsteady loads, often associated with increased vibration and higher noise emissions. At the structural level, the hub and transmission system must accommodate two concentric counter-rotating shafts, which increases design complexity and maintenance requirements. Despite these challenges, coaxial rotors remain a widely adopted solution, as their operational benefits frequently outweigh the associated disadvantages.

A schematic representation of an isolated coaxial-rotor system, together with its main geometric parameters, is reported by Li et al. [17] and shown in Fig. 2.15. This diagram provides a conceptual framework that clarifies the relative positioning of the upper and lower rotors and highlights the key design variables governing their aerodynamic performance, thereby facilitating the interpretation of experimental and numerical results.

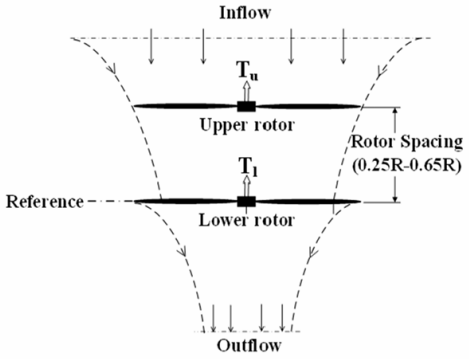

Figure 2.15: Schematic of an isolated coaxial-rotor system with design parameters (adapted from Li et al. [17]).

Building on this representation, Xu et al. [3] conducted a detailed numerical investigation of coaxial contra-rotating propellers in eVTOL applications, comparing their performance with that of isolated single rotors. Their analysis highlighted that the upper and lower propellers experience different lift distributions compared to a single rotor, due to mutual aerodynamic interference.

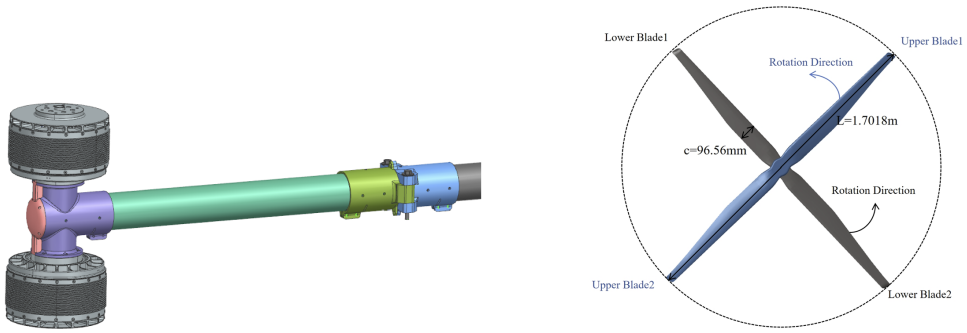

(a) Propeller arm assembly of a coaxial contra-rotating system.

(b) Top view of coaxial contra-rotating propellers.

Figure 2.16: Illustrations of coaxial contra-rotating rotor configuration (adapted from Xu et al. [3]).

Furthermore, Xu et al. [3] analyzed the aerodynamic interaction between the two rotors by simulating the flow field at four different rotational speeds, ranging from 1460 RPM to 2823 RPM. Their results showed that the downwash generated by the upper propeller strongly modifies the inflow conditions of the lower propeller, accelerating the incoming flow and deflecting it downwards. This interaction alters the effective angle of attack of the lower blades, which in turn reduces the extent of the high-pressure region on the lower surface and modifies the pressure distribution around the propeller disk.

The velocity and pressure maps reported in Fig. 2.17 provide a clear visualization of these mechanisms: the wake of the upper propeller directly affects the structure of the flow field around the lower propeller, generating turbulence and tip vortices that further disturb its aerodynamic performance. As a consequence, the lower propeller suffers from a significant loss of efficiency compared to the upper one.

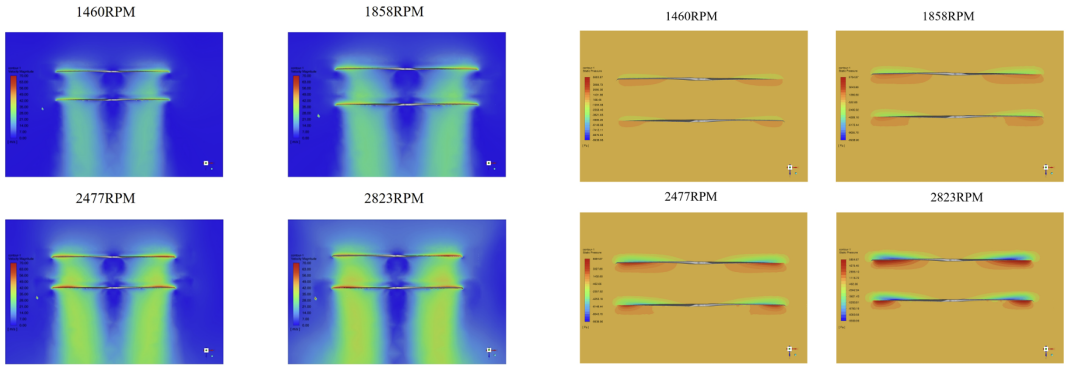

(a) Velocity distribution in the wake of coaxial contra-rotating propellers.

(b) Pressure contour map around coaxial contra-rotating propellers.

Figure 2.17: Flow-field analysis of coaxial contra-rotating propellers (adapted from Xu et al. [3]).

A quantitative analysis of lift and torque further confirmed these effects. The upper propeller exhibited only a modest loss of performance, with lift reduction below 5% compared to a single rotor. In contrast, the lower propeller showed a markedly stronger degradation, with lift losses reaching nearly 34% at the highest tested RPM. As a result, the total lift produced by the coaxial system is reduced by about 35–39% compared to the thrust that would be expected from the sum of two isolated rotors. Counter rotation cancels most of the net torque (over 93%), but a small residual moment persists due to the asymmetric flow conditions between the two propellers.

Overall, these results confirm that the principal drawback of coaxial contra-rotating systems lies in the aerodynamic interference between the two rotors, especially the downwash of the upper rotor on the lower one. To mitigate these effects, many UAV and eVTOL designs adopt **ducted coaxial configurations**, where the addition of a duct helps reduce tip losses, enhance thrust production, and lower noise emissions. The **Hovera UAV**, which constitutes the subject of this thesis, is a representative example of this combined design approach.

2.7.3 Ducted Rotors

The ducted rotor configuration deserves particular attention in this study, since the Hovera UAV combines a coaxial layout with ducted propellers. Ducts, also referred to as shrouds, surround the rotor disk and alter the flow distribution, effectively reducing tip losses and enhancing thrust efficiency. In addition, ducts can

contribute to noise attenuation and improved safety by shielding the blades. These features make ducted rotors an attractive choice for UAV and eVTOL applications.

A recent CFD based investigation [19] performed a parametric comparison between ducted and unducted rotors. The study clearly showed the advantages provided by the duct in terms of wake uniformity and thrust production. Figure 2.18 illustrates a 3D rendering of the ducted geometry, while Fig. 2.19 compares the flow structures in yawed inflow conditions, highlighting the differences between ducted and unducted cases. In particular, the duct suppresses the development of strong tip vortices, thereby reducing induced losses and stabilizing the wake.

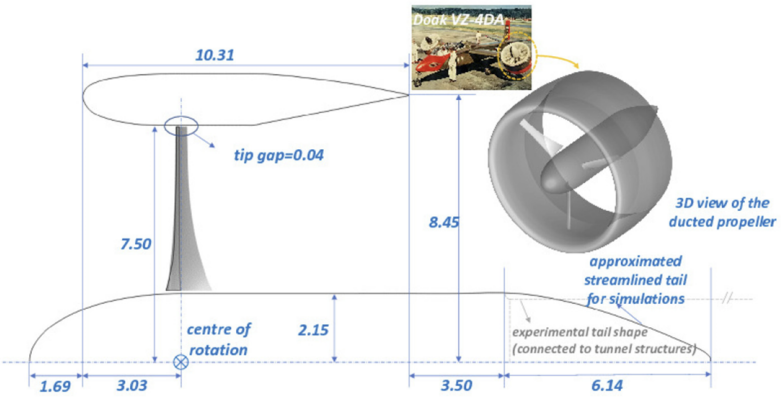

Figure 2.18: Ducted rotor configuration (adapted from Zhang et al. [19]).

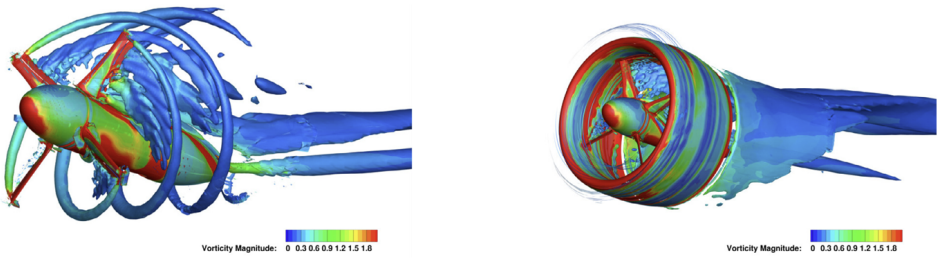

(a) Wake of the equivalent open rotor.

(b) Wake of the ducted rotor.

Figure 2.19: Comparison of flow structures between ducted and unducted rotors under yawed inflow (adapted from Zhang et al. [19]).

Alongside numerical simulations, experimental investigations provide valuable insight into the actual performance of ducted coaxial systems. Li et al. [17] developed

and tested a prototype of a ducted coaxial UAV. Figures 2.20 and **??** show, respectively, the vehicle prototype and the experimental test rig. The experimental campaign included tests on both single ducted rotors and ducted coaxial configurations, allowing a direct assessment of their relative performance.

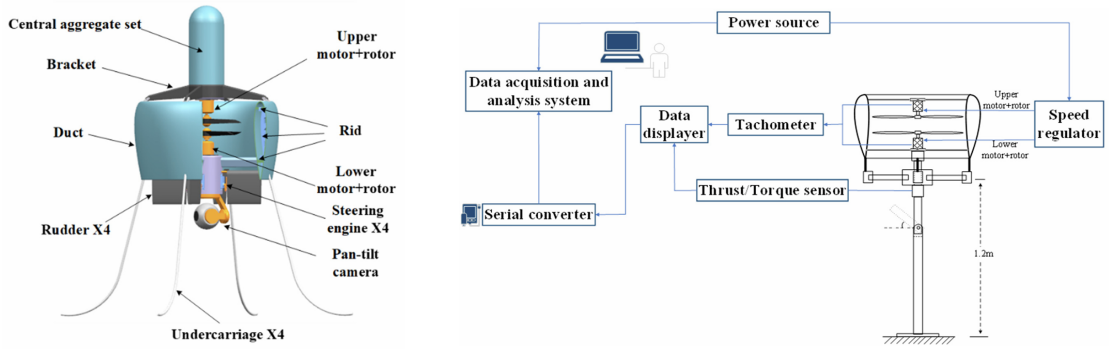

Figure 2.20: (a) Prototype of the ducted coaxial-rotor UAV. (b) Sketch of the experimental setup.

Figure 2.21: Experimental study of a ducted coaxial-rotor UAV [17].

Figure 2.22 provides a schematic comparison between a single ducted rotor and a ducted coaxial arrangement. In this context, the rotor position relative to the duct lip is identified as a critical design parameter, since it directly affects the aerodynamic performance of the system.

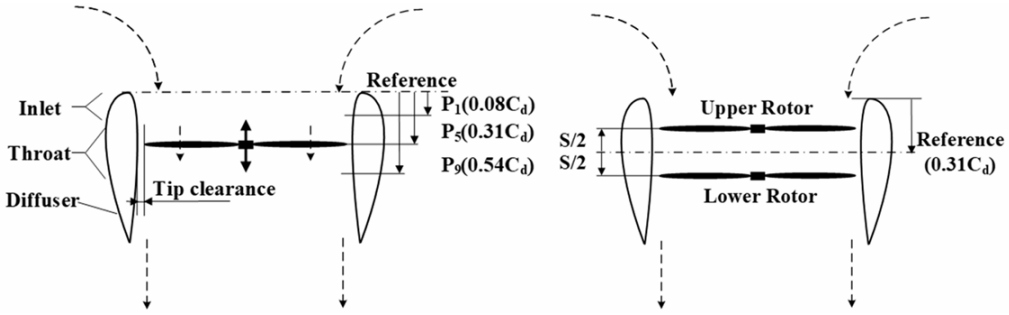

Figure 2.22: Comparison between ducted single-rotor and ducted coaxial-rotor configurations (adapted from Li et al. [17]).

Li et al. [17] first analyzed the ducted coaxial configuration, highlighting how the spacing between the two propellers strongly influences the distribution of thrust

within the system. The lower rotor was consistently penalized by the wake generated upstream, delivering a smaller share of the total lift, although both propellers were affected by mutual aerodynamic interference. In spite of these penalties, the coaxial arrangement exhibited higher overall propulsive efficiency than an isolated single rotor, primarily due to the increased power loading provided by the ducted configuration.

The same study then investigated ducted single rotor configurations by vertically sliding the rotor within the duct to different positions (P1–P5 for the upper rotor, P6–P9 for the lower rotor). The results, reported in Fig. 2.23, demonstrated that the duct consistently augmented thrust while reducing power requirements compared to the isolated rotor. In particular, the optimal performance occurred at the P5 location, where the small tip clearance ($\approx 1.4\%R$) effectively suppressed tip vortex leakage. At this position, the thrust of the ducted rotor was about 20% higher than that of the unducted rotor, with the duct itself contributing a significant portion of the total lift through rotor off-loading effects.

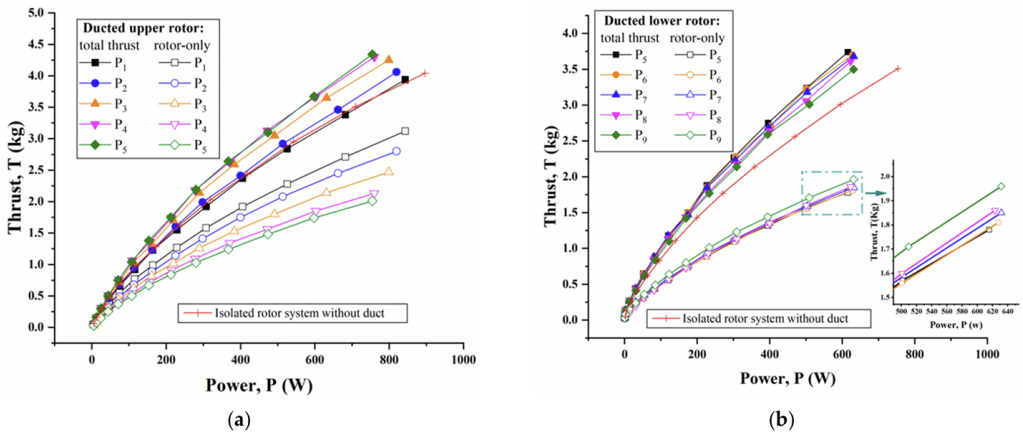

Figure 2.23: Static thrust performance of the ducted single-rotor system with variation in rotor–duct position. (a) Upper rotor positions P1–P5. (b) Lower rotor positions P6–P9. Comparison with unducted configuration included (adapted from Li et al. [17]).

Further measurements at constant power (600 W) confirmed that the thrust ratio of the ducted rotor to the isolated one peaked at the P5 location, with gains of approximately 20%.

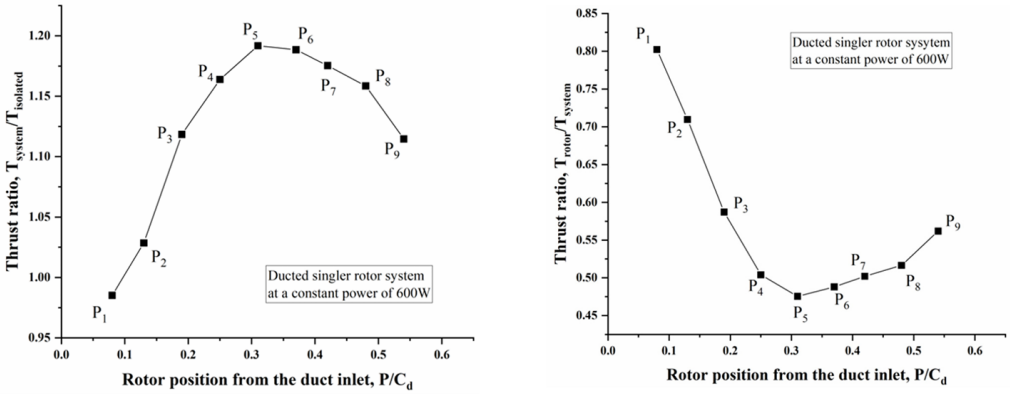

Figure 2.24: Hover performance of the ducted single rotor at constant power (600 W): (a) thrust ratio of the ducted system to the isolated rotor, (b) thrust ratio of the rotor contribution within the duct to the overall system [17].

This behavior was primarily attributed to the duct restraining tip vortex development and reducing inflow losses, while the exact rotor position introduced secondary but measurable effects on overall efficiency.

In summary, the combined numerical and experimental evidence leads to three key conclusions. First, the presence of a duct significantly enhances rotor performance by suppressing tip vortices and reducing leakage losses. Second, in coaxial ducted systems the spacing between the two propellers plays a decisive role in thrust sharing, with smaller separations generally leading to better efficiency. Finally, while torque cancellation is achieved to a large extent, the lower rotor remains penalized by the downwash of the upper one, which makes accurate aerodynamic optimization essential for practical applications in UAVs.

Chapter 3

Blade Element Momentum Theory (BEMT)

To evaluate the aerodynamic performance of the propeller, both theoretical and numerical approaches can be employed. In this study, a low–fidelity aerodynamic model based on the *Blade Element Momentum Theory (BEMT)* was implemented in MATLAB to estimate the thrust, torque, and power generated by a single three bladed propeller in hover. This preliminary approach provides a baseline for comparison with mid–fidelity numerical simulations performed with DUST, allowing an assessment of the model's accuracy and the influence of key parameters such as pitch, clearance, and rotational speed.

The theoretical framework of the underlying *Blade Element Theory (BET)* has been described in Chapter 2. Here, the emphasis is on its numerical implementation within the complete *Blade Element Momentum Theory (BEMT)* formulation, following the approaches outlined by Johnson [9] and Leishman [8]. The computation employs an iterative scheme to determine the induced velocity distribution along the blade span, inspired by the method proposed by Lucas [18] in his study of coaxial counter–rotating rotors. Although the present study focuses on a single open propeller, the same computational framework can be extended to more complex rotor configurations.

3.1 BEMT and Prandtl Tip-loss Correction

The numerical model divides the blade into N annular elements of equal radial length dr, each defined by its local chord $c(r)$ and aerodynamic coefficients C_L and C_D. For each element, the equilibrium between aerodynamic loads and the induced flow is solved iteratively through a Newton–Raphson procedure, enabling

the computation of local induced velocity w_i, relative velocity U_{rel}, and corresponding thrust and torque increments.

The main input parameters include the air density ρ, propeller geometry (radius R, chord distribution $c(r)$, and pitch angle θ), number of blades B, and angular velocity Ω. The freestream velocity V_∞ is set to zero to simulate hover conditions. The procedure computes the differential thrust and torque at each radial station and integrates them along the span to obtain the total thrust T, torque Q, and power P.

The MATLAB implementation was carried out for the same propeller model used in the experimental and numerical analyses, a three–bladed propeller with diameter 15″ and pitch 13.5″ (15×13.5×3). Three rotational speeds (4000, 5000 and 6000 RPM) were considered, matching the operating conditions later tested in the DUST simulations. The code also evaluates the thrust contribution at the blade tip and plots the radial load distribution $dT(r)$, which shows the increase in aerodynamic loading toward the outer blade sections.

3.1.1 BEMT without Prandtl Correction

The MATLAB script presented below implements the classical *Blade Element Momentum Theory (BEMT)* to predict the aerodynamic performance of the three–bladed propeller in hover. In this formulation, the inflow is assumed to be axisymmetric and steady across the rotor disk, neglecting viscous losses and the reduction in circulation near the blade tips.

This simplified model represents the reference configuration from which more accurate formulations, including the Prandtl tip–loss factor, actual chord and twist distributions, and induced power corrections, will be progressively introduced in the following sections.

```
1  %% Classical Blade Element Momentum (BEM) method - No Prandtl
       correction
2
3  clc;
4  clear all;
5  close all;
6
7  % -------------------- General parameters ---------------------
8
9  rho = 1.225;                    % air density [kg/m^3]
10 D_inch = 15;                    % propeller diameter [in]
11 D = D_inch * 0.0254;            % diameter [m]
```

```
R = D / 2;                          % radius [m]
B = 3;                              % number of blades
pitch_inch = 13.50;                 % geometric pitch [in]
pitch = pitch_inch * 0.0254;        % pitch [m]
theta_deg = atand(pitch / (2 * pi * R));
theta = deg2rad(theta_deg);         % pitch angle [rad]
RPM = 419 * 60 / (pi * 2);
Omega = RPM * 2 * pi / 60;          % angular velocity [rad/s]
V_inf = 0;                          % freestream velocity (hover)

% ---------------------- Discretization ----------------------

N = 50;                             % number of blade elements
r = ((0.5:N) / N) * R;              % element centroids
dr = R / N;                         % element length

% --------------- Geometry and aerodynamic data -------------

c = linspace(0.1, 0.02, N);         % chord distribution [m]
a0  = 2 * pi;                       % lift slope [1/rad]
CD0 = 0.014;                        % baseline drag coefficient
kCD = 0.02;                         % quadratic drag term
% ---------------------- Initialization ----------------------
dT = zeros(1, N);
dQ = zeros(1, N);
w_vector = zeros(1, N);

% ---------------------- Radial loop ----------------------

for i = 1:N
    w0 = 1; tol = 1e-4; h = 0.01;
    for k = 1:100
        V_tang = Omega * r(i);
        f = @(w) (8*pi*r(i) / (B*c(i))) * w ...
               - sqrt(1+(V_tang.^2)./(V_inf + w).^2).* ( ...
                 (a0.*(theta-atan((V_inf+w)./ V_tang))).*V_tang...
               -(CD0 + kCD .* (a0.*(theta-atan((V_inf + w)./V_tang
    ...
                 ... ))).^2).*(V_inf+w));
        fw = f(w0);
        df = (f(w0 + h) - f(w0 - h)) / (2 * h);
        w1 = w0 - fw / df;
        if abs(w1 - w0) < tol, break;
        end
        w0 = w1;
    end
    w_vector(i) = w1;

    V_tang = Omega * r(i);
```

```
60      phi = atan((V_inf + w1) / V_tang);
61      alpha = theta - phi;
62      CL_i = a0 * alpha;
63      CD_i = CD0 + kCD * CL_i.^2;
64
65      V_E = sqrt((V_inf + w1)^2 + V_tang^2);
66      L = 0.5 * rho * V_E^2 * c(i) * CL_i * dr;
67      D = 0.5 * rho * V_E^2 * c(i) * CD_i * dr;
68
69      dT(i) = L * cos(phi) - D * sin(phi);
70      dQ(i) = r(i) * (L * sin(phi) + D * cos(phi));
71  end
72
73  % ---------------------- Total forces ----------------------
74
75  Thrust = B * sum(dT)
76  Torque = B * sum(dQ)
77  Power  = Torque * Omega
78
79  % ----------------- Radial thrust distribution -----------------
80
81  figure; hold on; grid on; box on;
82  plot(r/R, dT, 'bo-', 'LineWidth', 1.5, 'MarkerSize', 6);
83  xlabel('$r/R$', 'Interpreter', 'latex', 'FontSize', 14);
84  ylabel("$dT$ [N]", "Interpreter", "latex", "FontSize",14);
85  title("Radial Thrust Distribution","Interpreter", "latex","
        FontSize",14)
86  fprintf("Thrust contribution at the tip (r=R): %.4f N\n", dT(end)
        )
```

Listing 3.1: MATLAB implementation of the Blade Element Momentum Theory (BEMT) method without Prandtl tip–loss correction.

The script above employs an iterative Newton–Raphson scheme to determine the induced velocity at each blade section, enforcing the local equilibrium between aerodynamic and momentum forces. The main physical quantities involved in the computation are summarized below:

- `r`: radial position of the blade element, measured from the hub.
- `c(r)`: local chord length of the blade section.
- `w_vector`: induced velocity distribution along the blade span, obtained iteratively.
- $V_{tang} = \Omega r$: local tangential velocity due to blade rotation.

- $V_{rel} = \sqrt{(V_\infty + w_i)^2 + (\Omega r)^2}$: resultant inflow velocity at each element.
- $\phi = \arctan\left(\frac{V_\infty}{\Omega r}\right)$: inflow angle between the relative velocity and the rotor plane.
- C_L , C_D: lift and drag coefficients of the airfoil section, assumed constant in this simplified implementation.
- `dT, dQ`: elemental thrust and torque contributions computed along the span.

These quantities are integrated along the radius to obtain the global propeller performance in terms of thrust, torque, and power:

$$T = B \sum_i dT_i, \qquad Q = B \sum_i dQ_i, \qquad P = Q\Omega$$

Results and Comparison with Reference Data

The MATLAB implementation of the BEMT provides an analytical estimation of the propeller's aerodynamic performance in hover. To evaluate the consistency of the results, the thrust, torque, and power computed with the MATLAB model were compared with both the manufacturer's reference data (provided by APC Propellers) and the predictions obtained from the mid-fidelity solver DUST. The reference values correspond to experimental performance curves available for the 15×13.5×3 propeller operating at the same rotational speeds considered in this study.

Table 3.1 reports the comparison between the results of the MATLAB BEMT model and the manufacturer's reference measurements, together with the relative percentage error defined as:

$$\text{Err } [\%] = \frac{|\text{Prediction} - \text{Ref}|}{\text{Ref}} \times 100. \tag{3.1}$$

where:

- Prediction denotes the value estimated through the MATLAB analysis;
- Ref corresponds to the experimental reference data provided by the manufacturer (APC Propellers);
- Err [%] represents the absolute percentage deviation between the predicted and reference quantities.

ω [rad/s]	Thrust [N]			Torque [Nm]			Power [W]		
	BEMT	Ref	Err [%]	BEMT	Ref	Err [%]	BEMT	Ref	Err [%]
419.0	20.52	17.85	15.0	0.541	0.517	4.64	226.77	216.50	4.74
524.0	32.12	27.95	14.9	0.846	0.796	6.28	443.55	416.62	6.46
628.0	46.14	40.34	14.4	1.216	1.135	7.14	763.54	713.44	7.03

Table 3.1: Comparison between MATLAB–BEMT predictions and manufacturer reference data for the 15×13.5×3 propeller in hover.

The results show that the BEMT implementation slightly overestimates the propeller performance compared with the manufacturer's data, with thrust deviations of approximately 14–15% and smaller errors (below 7%) for torque and power. This consistent overprediction can be attributed to the simplified aerodynamic modeling, which neglects the loss of circulation near the tip and viscous dissipation effects.

Figure 3.1 shows the radial thrust distribution along the blade span, obtained by plotting the differential thrust dT as a function of the normalized radius r/R for the operating condition of 4000 RPM ($\omega = 419$ rad/s).

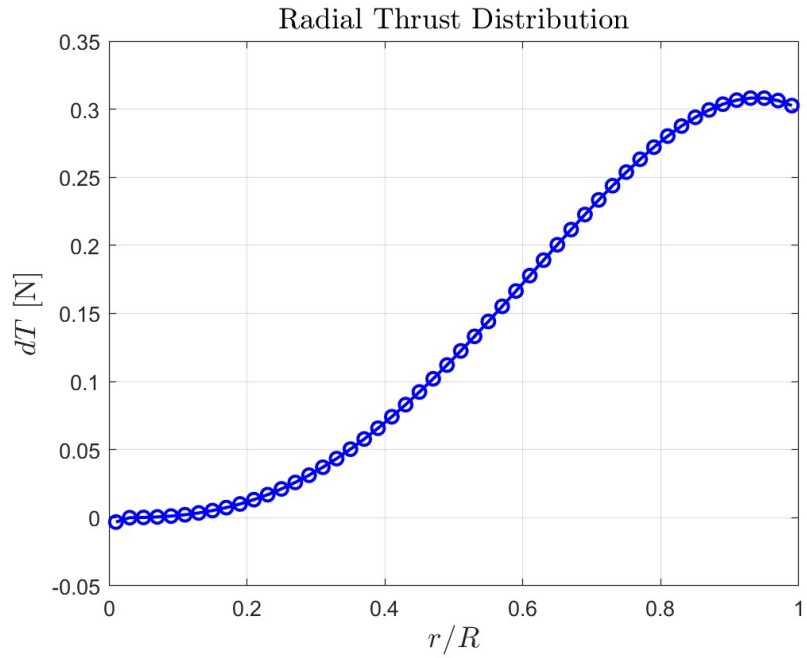

Figure 3.1: Radial thrust distribution obtained from the MATLAB BEMT model at 4000 RPM ($\omega = 419$ rad/s).

As expected, the aerodynamic load increases progressively toward the outer blade sections, where the tangential velocity and dynamic pressure are higher. The thrust contribution at the blade tip corresponds to approximately 0.303 N, confirming the predominant role of the tip region in the overall thrust generation.

The computed radial distribution is consistent with classical rotor theory, according to which the largest portion of thrust is produced in the outer third of the blade. This trend results from the quadratic increase in tangential velocity with radius, leading to higher local dynamic pressure and lift. The near–linear growth of $dT(r)$ with r/R observed in the results confirms the correct aerodynamic scaling of the implemented formulation.

Overall, the present model provides a robust *low–fidelity baseline* for the estimation of propeller performance in hover. However, it neglects essential effects such as the loss of circulation near the blade tips, viscous dissipation, and the actual twist and chord distributions of the tested propeller. For this reason, the following section introduces the **Prandtl correction**, which refines the BEMT formulation by accounting for finite blade effects and improving the prediction accuracy, particularly in the outer span region.

In the next stages, the BEMT framework will be progressively enhanced by including:

1. the **Prandtl tip–loss correction**, accounting for finite–blade effects;
2. the actual **chord and twist distributions** of the selected propeller.

3.1.2 Prandtl Tip–Loss Correction

The *Prandtl tip–loss correction* represents one of the most fundamental improvements to the classical momentum theory for finite bladed rotors. Originally developed by Ludwig Prandtl in the early 20^{th} century, the correction accounts for the reduction in circulation and aerodynamic loading near the blade tips due to the finite number of blades. Prandtl showed that, unlike an ideal rotor with an infinite number of blades where circulation remains constant along the span, real propellers experience a loss of lifting capability near the tip caused by the lateral leakage of vorticity and pressure equalization between the upper and lower surfaces of the blade. This results in a local decrease of induced velocity and aerodynamic efficiency in the outer radial region.

As detailed by Branlard [22] in *Wind Turbine Aerodynamics and Vorticity Based Methods*, the derivation of the tip–loss factor stems from vortex wake theory and aims to correct the overestimation of thrust and torque predicted by the ideal actuator disk model. A complementary and extensive review is provided by Ramdin [23], who examined the applicability and limitations of Prandtl's original formulation for modern rotors, demonstrating that the correction improves prediction accuracy under moderate loading conditions but may require adaptation for heavily loaded or distorted inflows.

In the framework of the *Blade Element Momentum Theory (BEMT)*, the inclusion of the tip–loss factor F mitigates the overestimation of thrust and torque resulting from the assumption of an axisymmetric and uniformly loaded rotor disk. Physically, F acts as a scaling factor (ranging from 0 to 1) that reduces both the induced velocity and aerodynamic forces near the tip, where the effective lifting area decreases.

The classical expression of Prandtl's tip–loss factor is given by:

$$F = \frac{2}{\pi} \arccos\left[\exp\left(-\frac{B}{2}\frac{R-r}{r\sin\phi}\right)\right] \tag{3.2}$$

where B is the number of blades, R is the rotor radius, r is the local radial coordinate, and ϕ is the inflow angle. When $r/R \to 1$, the exponential term reduces F, effectively attenuating the aerodynamic loading at the tip and improving the physical realism of the BEMT predictions.

By introducing F in the momentum balance, the local induced velocity equation becomes:

$$f(w_i) = \frac{8\pi r_i}{Bc_i}\frac{w_i}{F} - \sqrt{1 + \frac{(\Omega r_i)^2}{(V_\infty + w_i)^2}}[a_0(\theta_i - \phi_i)\,\Omega r_i - (C_{D0} + k_{CD}a_0^2(\theta_i - \phi_i)^2)(V_\infty + w_i)] = 0 \tag{3.3}$$

This equation represents the nonlinear coupling between the induced inflow computed from momentum theory and the aerodynamic forces predicted by the blade element formulation. By balancing these two descriptions of the flow, the model ensures a consistent estimation of the local induced velocity along the blade span. The inclusion of the Prandtl factor F in the denominator corrects the local induced velocity w_i to account for the finite number of blades, effectively reducing the aerodynamic loading toward the tip. This approach is consistent with modern BEMT implementations described by Branlard [22] and Ramdin [23].

The elemental thrust and torque contributions are corrected as:

$$\begin{aligned} dT_i &= F\,(L_i \cos\phi_i - D_i \sin\phi_i)\,, \\ dQ_i &= F\,r_i\,(L_i \sin\phi_i + D_i \cos\phi_i) \end{aligned} \tag{3.4}$$

The MATLAB implementation including the Prandtl correction is reported below. It extends the previous code by introducing F both in the iterative solution of w_i and in the computation of the elemental loads.

```
1
2  %% Classical BEMT method with Prandtl tip loss correction
3  clc; clear all; close all;
4
5  % --- Parameters and geometry identical to previous script ---
6
7  for i = 1:N
8      w0 = 1; tol = 1e-4; h = 0.01;
9      for k = 1:100
10         V_tang = Omega * r(i);
11         phi0 = atan((V_inf + w0) / V_tang);
12         sphi0 = max(sin(phi0), 1e-6);
13         F0 = (2/pi) * acos(exp(-(B/2)*((R - r(i)) / (r(i)*sphi0)))
       );
14         F0 = max(F0, 1e-3);
15
16         f = @(w) (8 * pi * r(i) / (B * c(i))) * (w / F0) ...
17                 - sqrt(1 + (V_tang.^2)./(V_inf + w).^2) .* ( ...
18                   (a0.*(theta - atan((V_inf + w)./ V_tang))).*
       V_tang ...
19                 - (CD0 + kCD .* (a0 .* (theta - atan((V_inf ...
20                 + w) ./ V_tang))).^2) .* (V_inf + w) );
21
22         fw = f(w0);
23         df = (f(w0 + h) - f(w0 - h)) / (2*h);
24         w1 = w0 - fw / df;
25         if abs(w1 - w0) < tol, break; end
26         w0 = w1;
27     end
28
29     % Recalculate F using final phi
30     phi = atan((V_inf + w1) / V_tang);
31     sphi = max(sin(phi), 1e-6);
32     F = (2/pi) * acos(exp(-(B/2)*((R - r(i)) / (r(i)*sphi))));
33     F = max(F, 1e-3);
34
35     % Apply F to aerodynamic loads
36     alpha = theta - phi;
```

```
37      CL_i = a0 * alpha;
38      CD_i = CD0 + kCD * CL_i.^2;
39      V_E = sqrt((V_inf + w1)^2 + V_tang^2);
40      L = 0.5 * rho * V_E^2 * c(i) * CL_i * dr * F;
41      D = 0.5 * rho * V_E^2 * c(i) * CD_i * dr * F;
42
43      dT_prandtl(i) = L * cos(phi) - D * sin(phi);
44      dQ_prandtl(i) = r(i) * (L * sin(phi) + D * cos(phi));
45  end
```

Listing 3.2: Modified MATLAB implementation of the BEMT method including the Prandtl tip–loss correction.

To assess the influence of the correction, the results obtained with and without the Prandtl factor were compared in terms of thrust, torque, and power. Table 3.2 reports the predicted values and their relative difference.

ω [rad/s]	**Thrust [N]**			**Torque [Nm]**			**Power [W]**		
	Without	With	Var. [%]	Without	With	Var. [%]	Without	With	Var. [%]
419.0	20.52	18.82	8.3	0.541	0.479	6.2	226.77	200.60	11.6
524.0	32.12	29.47	8.2	0.846	0.749	7.2	443.55	392.359	11.5
628.0	46.14	42.33	8.3	1.216	1.076	7.3	763.54	675.412	11.5

Table 3.2: Comparison of thrust, torque, and power with and without Prandtl tip–loss correction for the 15×13.5×3 propeller in hover at different rotational speeds.

The results show that the inclusion of the Prandtl factor leads to a moderate reduction in thrust and torque (approximately 6–7%), mainly due to the decreased effective loading near the blade tip. This correction improves the physical consistency of the BEMT model, bringing the predictions closer to experimental trends typically observed for small propellers.

The radial thrust distribution $dT(r)$ also exhibits a smoother decay near $r/R \to 1$, consistent with the expected tip–loss behaviour. Figure 3.2 compares the radial load distributions obtained *with* and *without* the Prandtl tip–loss correction for the operating condition of 4000 RPM ($\omega = 419$ rad/s). The effect of the correction is clearly visible in the outer span region, where the aerodynamic load is reduced due to finite–blade efficiency losses.

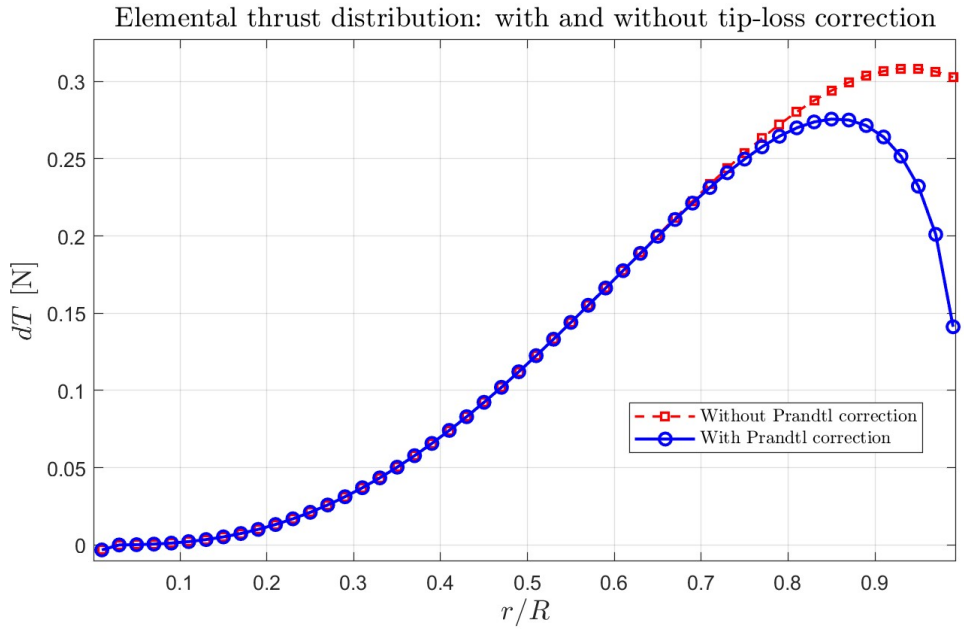

Figure 3.2: Comparison of radial thrust distribution with and without Prandtl correction for the operating condition of 4000 RPM ($\omega = 419$ rad/s).

A similar behaviour was reported by Oliveira *et al.* [24], who demonstrated that the inclusion of Prandtl's tip–loss factor significantly improves the prediction of thrust distribution near the blade tip, leading to a smoother decay and better agreement with experimental data for horizontal axis rotors. This consistency further supports the physical accuracy of the implemented correction.

To further assess the effect of the Prandtl correction on the model accuracy, the corrected BEMT predictions were compared with the manufacturer's experimental data. Table 3.3 summarizes this comparison for the three operating speeds considered. As shown, the inclusion of the Prandtl tip–loss factor reduces the overall prediction error, improving the agreement with reference measurements in terms of thrust, torque, and power.

By comparing the results in Tables 3.1 and 3.3, it is evident that the inclusion of the Prandtl tip–loss correction significantly improves the overall agreement with the manufacturer's reference data. The average deviation in thrust decreases from approximately 15% to about 5%, while torque and power errors are reduced to below 7%. This improvement confirms that accounting for finite–blade effects is essential to achieve realistic aerodynamic predictions, particularly near the tip region where the uncorrected BEMT model tends to overestimate the loading.

ω [rad/s]	**Thrust [N]**			**Torque [Nm]**			**Power [W]**		
	Prandtl	Ref	Err [%]	Prandtl	Ref	Err [%]	Prandtl	Ref	Err [%]
419.0	18.82	17.85	5.4	0.479	0.517	7.4	200.6	216.5	7.4
524.0	29.47	27.95	5.4	0.749	0.796	5.9	392.4	416.6	5.8
628.0	42.33	40.34	4.9	1.076	1.135	5.2	675.4	713.4	5.3

Table 3.3: Comparison between the BEMT predictions (including Prandtl correction) and manufacturer reference data for the 15×13.5×3 propeller in hover.

3.1.3 Prandtl Correction and Real Geometry

Starting from the previously validated BEMT implementation, the MATLAB model was extended to include the Prandtl tip–loss correction together with the real geometric characteristics of the APC 15×13.5×3 propeller. The geometric data, provided by the manufacturer (APC Propellers), specify the spanwise variations of chord length and twist angle derived from the actual blade design. This approach enables a more realistic representation of the propeller aerodynamics while maintaining the same theoretical framework and numerical procedure described in the previous section.

The computational method remains based on the iterative Newton–Raphson solution of the local momentum equilibrium. The Prandtl factor F is still computed according to Equation (3.2), while the blade geometry is discretized into ten spanwise sections consistent with the configuration later employed in the DUST simulations. This ensures a one–to–one correspondence between the MATLAB and DUST discretizations, allowing a meaningful comparison of the resulting load distributions. The spanwise geometric data used in the present analysis are summarized in Table 3.4. Each radial section is defined by its local radius, chord, and pitch angle (or twist). These values were directly obtained from the manufacturer's technical database and converted into SI units for numerical implementation.

The simplified aerodynamic representation, combined with the real chord and twist distributions of the APC 15×13.5×3 propeller, provides a sufficiently accurate yet computationally efficient basis for low–fidelity performance prediction. The performance of the corrected BEMT model ($\mathbf{BEMT_{corr}}$), which includes both the Prandtl tip–loss factor and the real propeller geometry, is quantitatively assessed against the manufacturer's experimental data.

Section	**Radius r_i [m]**	**Element Width dr_i [m]**	**Chord c_i [m]**	**Twist θ_i [deg]**
1	0.04848	0.00734	0.02537	42.32
2	0.05939	0.01448	0.02577	40.65
3	0.07592	0.01857	0.02653	37.33
4	0.09554	0.02067	0.02717	32.90
5	0.11638	0.02101	0.02694	27.96
6	0.13675	0.01973	0.02511	24.10
7	0.15511	0.01700	0.02136	21.29
8	0.17015	0.01307	0.01614	19.30
9	0.18359	0.01382	0.01066	17.46

Table 3.4: Spanwise geometric properties of the APC 15×13.5×3 propeller used in the BEMT implementation. The total propeller radius is $R = 0.1905$ m, and this same discretization is adopted in the DUST model for consistency.

The corresponding results are reported in Table 3.5. This comparison allows evaluating the overall accuracy of the low–fidelity formulation in reproducing the propeller's thrust, torque, and power in hover conditions.

ω [rad/s]	**Thrust [N]**			**Torque [Nm]**			**Power [W]**		
	$\mathbf{BEMT_{corr}}$	**Ref.**	**Err. [%]**	**$\mathbf{BEMT_{corr}}$**	**Ref.**	**Err. [%]**	**$\mathbf{BEMT_{corr}}$**	**Ref.**	**Err. [%]**
419.0	17.48	17.85	2.1	0.475	0.517	8.1	199.08	216.50	8.0
524.0	27.35	27.95	2.1	0.742	0.796	6.8	388.85	416.62	6.7
628.0	39.28	40.34	2.6	1.065	1.135	6.2	669.07	713.44	6.2

Table 3.5: Comparison between the corrected BEMT model ($\mathbf{BEMT_{corr}}$) and manufacturer reference data for the APC 15×13.5×3 propeller in hover.

The results presented in Table 3.5 confirm that the inclusion of both the Prandtl tip–loss correction and the real geometric distributions significantly improves the physical realism of the BEMT formulation. The corrected model ($\mathbf{BEMT_{corr}}$) reproduces the manufacturer's experimental data with errors below 3% in thrust and approximately 6–8% in torque and power across the considered operating range. Such levels of deviation are fully consistent with the expected accuracy of low–fidelity analytical models when applied to small scale propellers operating at low Reynolds numbers.

Figure 3.3 compares the non–dimensional elemental thrust coefficient dC_T obtained from the classical BEMT formulation and from the Prandtl–corrected model using the actual APC 15×13.5×3 propeller geometry. The results refer to the operating condition of 4000 RPM ($\omega = 419$ rad/s). The normalization of the elemental thrust according to:

$$dC_T = \frac{dT}{\frac{1}{2}\rho(\Omega R)^2(2\pi r\, dr)}$$

allows for a direct comparison of the spanwise loading distributions, independent of the absolute thrust magnitude.

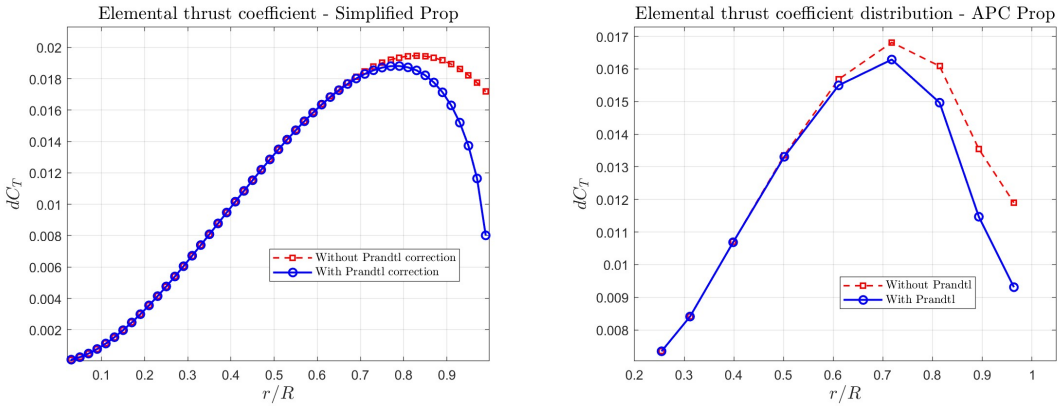

(a) Simplified geometry.

(b) Real APC geometry.

Figure 3.3: Spanwise distribution of the elemental thrust coefficient dC_T with and without Prandtl tip–loss correction at 4000 RPM ($\omega = 419$ rad/s).

In the simplified configuration (a), the spanwise loading exhibits a nearly parabolic shape, with a pronounced peak near $r/R \approx 0.8$ followed by a rapid drop toward the tip. When the real APC geometry is introduced (b), the distribution becomes smoother and slightly shifted toward mid–span, reflecting the influence of the actual chord and twist profiles.

The inclusion of the Prandtl tip–loss correction consistently mitigates the unrealistic load concentration near the blade tip, ensuring a physically consistent decay of dC_T as $r/R \to 1$. Overall, the corrected model captures the essential aerodynamic behavior of the propeller in hover, while the real geometry implementation enhances the fidelity of the radial load prediction.

3.2 Induced Velocity Field According to Lighthill

As previously discussed in Section 2.6.3, Lighthill [15] reformulated the classical actuator disk theory to include the presence of the ground, introducing the image-rotor concept to explain the aerodynamic interaction responsible for the ground effect. Beyond the prediction of the induced–power reduction (Figure 2.13), the same theoretical framework also yields an analytical description of the induced velocity distribution generated by a uniformly loaded disk in hover. This formulation represents the one–dimensional, axisymmetric flow solution of the model and serves as a reference for interpreting the axial evolution of the induced velocity in both low–fidelity (BEMT) and mid–fidelity (DUST) simulations.

After validating the Blade Element Momentum Theory (BEMT) model and its Prandtl–corrected formulation using the real APC propeller geometry, it is useful to compare these numerical predictions against the theoretical velocity field proposed by Lighthill. While BEMT provides the radial distribution of aerodynamic loads along the blades, it does not directly describe how the induced velocity evolves downstream of the propeller disk. To address this limitation, Lighthill's analytical model [15] is employed as a universal benchmark for the decay of the induced flow in the rotor wake.

In this model, the rotor is represented as an ideal *actuator disk* producing an axisymmetric, inviscid, and incompressible flow field. The analysis neglects blade geometry, airfoil characteristics, and tip losses, focusing exclusively on the fundamental physics of the induced–velocity field. The normalized axial coordinate z/R (with R the rotor radius) is linked to the auxiliary parameter $c > 1$ through the implicit relation derived by Lighthill:

$$\frac{z}{R} = \frac{1}{\pi}\left[\ln\left(\sqrt{c} + \sqrt{c-1}\right) + \frac{(c-1)^{3/2}}{c^{3/2} + 2c - 1}\left(\frac{\pi}{2} - \frac{\sqrt{c}}{\sqrt{c-1}}\right)\right] \tag{3.5}$$

from which the nondimensional induced velocity coefficient is obtained as

$$C_P = \frac{(c-1)^{3/2}}{c^{3/2} + 2c - 1} \tag{3.6}$$

This relation expresses the normalized induced velocity along the rotor axis, starting from its maximum immediately below the disk ($z/R \to 0$) and asymptotically approaching zero in the far wake ($z/R \to \infty$). It defines a universal curve that depends only on the normalized distance z/R, independent of any geometric or operational parameters.

Table 3.6 summarizes the variables used in the formulation.

Symbol	Description
z/R	Nondimensional distance along the rotor axis
c	Auxiliary variable in the implicit relation
C_P	Induced–velocity coefficient according to Lighthill
π	Mathematical constant (≈ 3.1416)

Table 3.6: Variables and notation used in the Lighthill formulation.

The implicit equation was solved numerically using MATLAB's `fsolve` routine, employing an iterative algorithm that enforces $c > 1$ and progressively updates the initial guess to ensure convergence across the entire range $z/R \in [0,3]$. For each value of z/R, the corresponding c was determined, and the induced–velocity coefficient C_P was computed accordingly. The complete MATLAB implementation is reported below.

```
%% Induced Velocity Distribution according to Lighthill (1952)
clc; clear; close all;

% ---- Range of nondimensional axial positions ----
z_R = linspace(0,3,60);   % z/R in [0,3]
C_p = zeros(size(z_R));   % induced velocity coefficient
opts = optimoptions('fsolve','Display','off');
c_guess = 2;              % initial guess (c > 1)

for i = 1:length(z_R)
    target = z_R(i);
    % Implicit Lighthill equation
    f = @(c) target - (1/pi)*( ...
        log(sqrt(c) + sqrt(c-1)) + ...
        ((c-1)^(3/2))/(c^(3/2) + 2*c - 1) * ...
        (pi/2 - sqrt(c)/(sqrt(c)-1)) ...
    );
    % Solve for c using fsolve
    [c_sol,~,exitflag] = fsolve(f, c_guess, opts);
    if exitflag > 0 && c_sol > 1
        C_p(i) = (c_sol-1)^(3/2) / (c_sol^(3/2) + 2*c_sol - 1);
        c_guess = c_sol; % update guess for next iteration
    else
        C_p(i) = NaN;
    end
```

```
end

% ---- Plot ----
figure;
plot(z_R, C_p, 'b-o','LineWidth',1.5, 'MarkerSize',4);
xlabel('$z/R$', 'Interpreter','latex', 'FontSize',14);
ylabel('$C_P$', 'Interpreter','latex', 'FontSize',14);
title("Lighthill induced velocity coefficient", 'Interpreter','
    latex',
'FontSize',14);
grid on;
```

The resulting distribution of the induced–velocity coefficient C_P along the rotor axis is shown in Figure 3.4. The curve shows a monotonic increase of C_P with the normalized axial coordinate z/R, representing the progressive recovery of the induced velocity within the rotor wake. Close to the actuator disk, the flow acceleration is most pronounced as the slipstream begins to contract, and as the distance from the rotor increases, the induced–velocity coefficient C_P progressively approaches its asymptotic value, corresponding to the fully developed slipstream in the far wake ($C_P \to 1$).

This monotonic growth of C_P with z/R reproduces the theoretical trend reported by Lighthill (1979, Fig. 4) and confirms the correctness of the numerical implementation. The analytical profile therefore provides a reliable reference for the axial evolution of the induced–velocity field predicted by both BEMT and DUST analyses.

Although this formulation neglects the geometric and aerodynamic properties of real propellers, it offers a rigorous analytical benchmark for interpreting the induced velocity field. When compared with the numerical predictions from the BEMT and mid–fidelity DUST simulations, the Lighthill curve provides a useful reference for validating the wake development rate and the induced velocity distribution along the rotor axis, bridging the ideal actuator disk theory with realistic propeller aerodynamics.

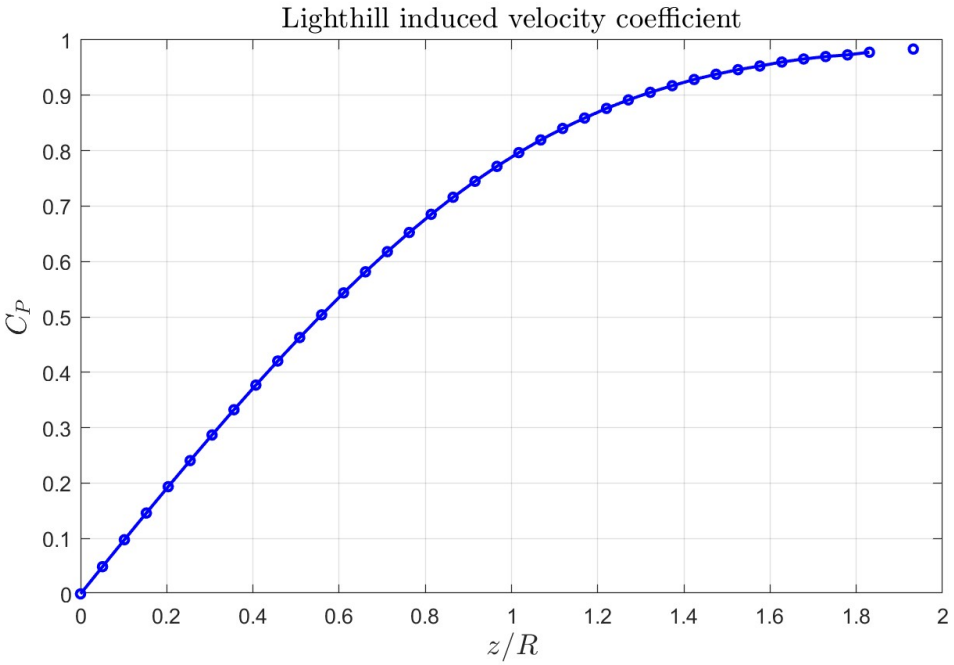

Figure 3.4: Axial distribution of the induced–velocity coefficient C_P according to Lighthill's analytical model (1979). The curve shows the monotonic increase of C_P with the nondimensional distance z/R, consistent with the analytical trend reported by Lighthill (1979, Fig. 4).

Chapter 4

Experimental Model Setup

Building on the numerical and theoretical findings discussed in Chapter 2, a controlled experimental campaign was carried out to validate the predicted ground effect on an open propeller. The objective was to quantify the variation of thrust and torque with the non-dimensional clearance h/R, and to assess whether the trends observed in the simulations were reproduced under laboratory conditions.

Since Hovera does not currently have a scaled prototype available, a smaller propeller was tested in the RMIT University laboratory to reproduce the ground-effect phenomenon under controlled conditions. The experiments were conducted in a closed-circuit wind tunnel, kept switched off during testing, providing a quiescent environment large enough to avoid wall interference and blockage effects. A movable wall was used to emulate the ground plane and systematically vary the rotor-to-wall distance, enabling controlled investigation of proximity effects on the aerodynamic loads.

The experimental results were compared with two complementary approaches: mid-fidelity numerical simulations using the DUST panel code, and the classical Cheeseman–Bennett formulation, which provides a semi-empirical correlation for the thrust ratio $T_{\mathrm{IGE}}/T_{\mathrm{OGE}}$. This chapter describes the experimental apparatus and testing procedure, including the CAD design and 3D printing of the Hovera-inspired duct.

4.1 Experimental setup

The experimental tests were conducted inside the closed-circuit wind tunnel of RMIT University, which was kept switched off during the measurements to ensure a

quiescent and unconfined flow environment. The setup allowed systematic variation of the rotor-to-wall distance and consisted of the following main components:

- **Propeller:** A three-blade, 15-inch propeller was employed to achieve representative Reynolds numbers without excessive power requirements. It was mounted 0.8 m above the floor, more than twice its diameter, to minimize interference with surrounding surfaces.
- **Motor:** A Hacker A50-16S V4 brushless motor was used to drive the propeller. The motor was powered by a DC supply and controlled through dedicated software that also managed data acquisition.
- **Load cell:** A six-axis load cell (Flight Stand 15 Pro, Tyto Robotics) was used to directly measure thrust and torque along the propeller axis, with a resolution of ± 150 N and ± 8 Nm, respectively. This ensured accurate characterization of the aerodynamic performance of the propeller.
- **Movable wall:** A 1.6 m $\times$ 1.6 m plywood plate mounted on an aluminum frame and placed beneath the rotor disk to simulate the ground plane. The wall was adjusted between tests to reproduce different non-dimensional clearances h/R and study the effect of ground proximity.
- **Duct:** A 3D-printed aerodynamic shroud, based on a NACA 0018 profile and manufactured in Polylactic Acid (PLA). It was supported by rigid mounts ensuring constant alignment with the rotor.

The overall setup allowed controlled variation of the propeller-to-wall distance, precise adjustment of the rotational speed, and rapid installation or removal of the duct when required. All measurements were recorded in real time through the Tyto Robotics interface, which managed both motor control and data acquisition for thrust and torque.

Before starting the experimental campaign, a preliminary calibration and verification phase was carried out under out of ground effect (OGE) conditions. This step aimed to confirm the reliability of the measurement system by comparing the thrust and torque recorded by the load cell with the reference performance data provided by the APC propeller manufacturer. The agreement was satisfactory, with deviations within 5–10%, thus validating the accuracy and consistency of the measurement setup. Following this verification, the first series of experiments was conducted with the open-propeller configuration, progressively reducing the distance between the rotor and the movable wall to analyze the effect of ground proximity.

Once all clearances had been tested, the duct was installed and the same sequence of measurements was repeated under identical operating conditions. For each configuration and clearance, four repetitions were performed under steady-state conditions to ensure data consistency and statistical reliability, while systematically varying the propeller–wall distance between 0.05 m and 0.70 m to cover the full range of ground proximities investigated.

The motor speed was electronically controlled through a predefined throttle sequence corresponding to three reference values, approximately 3000, 4000, and 5000 RPM, representative of hover-like operation. The sequence ensured smooth acceleration and deceleration phases, minimizing transient effects in the recorded data, as shown in Figure 4.1. The acquired thrust and torque measurements were then post-processed in MATLAB to enable direct comparison with the numerical predictions obtained from DUST.

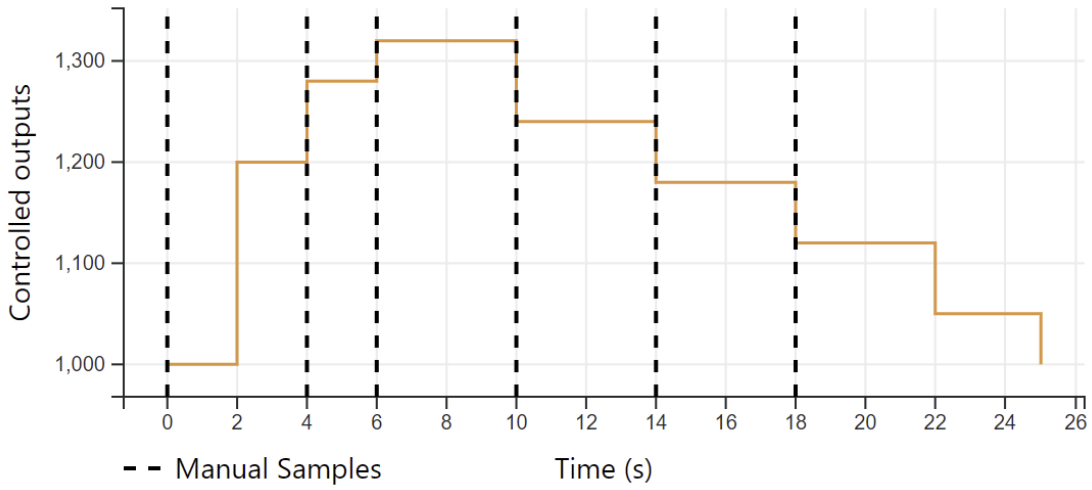

Figure 4.1: Automated throttle control sequence used during data acquisition.

Figure 4.2 presents the experimental setup used during the tests, showing the complete installation, the isolated propeller, and the ducted configuration.

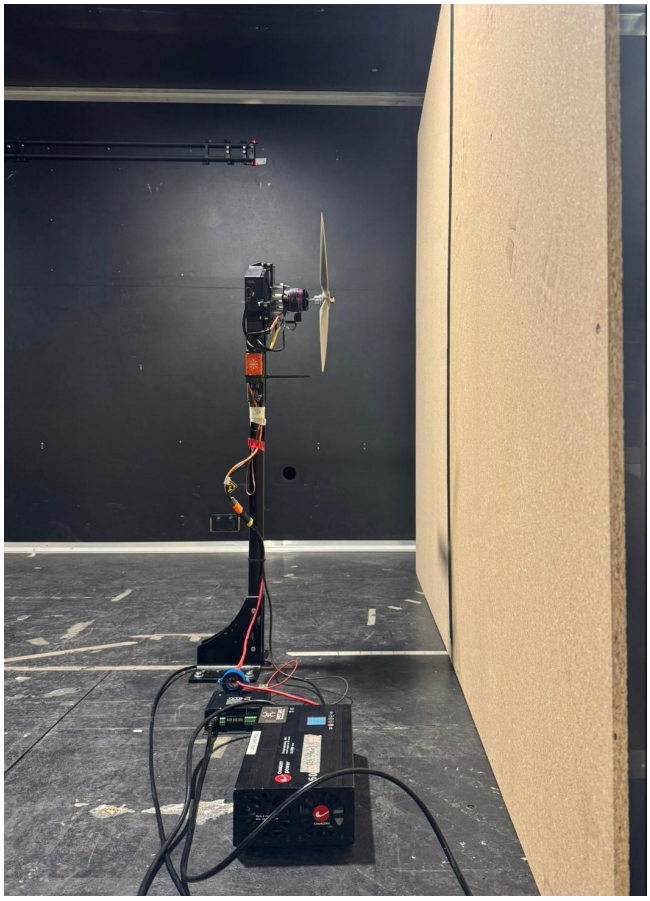

a. Overall setup with instrumentation

b. Propeller detail

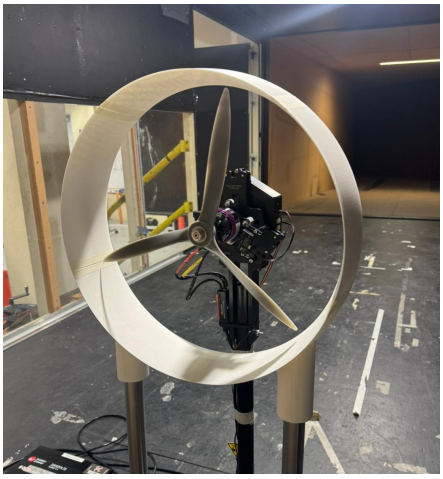

c. Ducted configuration

Figure 4.2: Photographs of the experimental setup: (a) overall view, (b) propeller detail and (c) ducted configuration.

4.1.1 Engine sizing

The selection and sizing of the motor are fundamental steps to ensure that the propulsion system operates within the required performance envelope during the ground-effect experiments. The sizing procedure was carried out by combining aerodynamic estimates based on the actuator disk model with the performance data provided by the propeller manufacturer.

For the tests, an APC three-blade propeller of size 15×13.5 was selected, as it enables achieving sufficiently high tip Reynolds numbers without demanding excessive power levels that would complicate the experimental setup. The corresponding

aerodynamic data supplied by the manufacturer (Figure 4.3) were used to define the initial constraints in terms of thrust, rotational speed, and Reynolds number.

PROP RPM = 4000

V (mph)	J (Adv_Ratio)	Pe -	Ct -	Cp -	PWR (Hp)	Torque (In-Lbf)	Thrust (Lbf)	PWR (W)	Torque (N-m)	Thrust (N)	THR/PWR (g/W)	Mach -	Reyn -	FOM -
0.00	0.0000	0.0000	0.1554	0.0742	0.290	4.575	4.012	216.513	0.517	17.846	8.405	0.24	92669.	0.6586
2.10	0.0369	0.0750	0.1548	0.0761	0.298	4.693	3.995	222.072	0.530	17.770	8.160	0.24	92776.	0.6380
4.19	0.0738	0.1454	0.1540	0.0782	0.306	4.816	3.975	227.936	0.544	17.680	7.909	0.24	92896.	0.6168
6.29	0.1107	0.2111	0.1530	0.0802	0.314	4.945	3.951	234.026	0.559	17.572	7.657	0.24	93031.	0.5953
8.39	0.1476	0.2722	0.1519	0.0824	0.322	5.076	3.922	240.243	0.574	17.443	7.404	0.24	93181.	0.5735
10.48	0.1845	0.3287	0.1506	0.0845	0.331	5.208	3.887	246.465	0.588	17.287	7.152	0.24	93346.	0.5516
12.58	0.2214	0.3808	0.1489	0.0866	0.339	5.336	3.844	252.541	0.603	17.099	6.904	0.24	93528.	0.5295
14.68	0.2583	0.4286	0.1470	0.0886	0.346	5.458	3.793	258.295	0.617	16.873	6.661	0.24	93728.	0.5075
16.77	0.2952	0.4724	0.1446	0.0904	0.353	5.568	3.732	263.523	0.629	16.602	6.424	0.24	93945.	0.4855
18.87	0.3321	0.5124	0.1418	0.0919	0.359	5.663	3.660	267.987	0.640	16.279	6.194	0.24	94181.	0.4636
20.97	0.3690	0.5490	0.1385	0.0931	0.364	5.735	3.574	271.415	0.648	15.897	5.973	0.24	94435.	0.4417
23.06	0.4059	0.5823	0.1345	0.0938	0.367	5.779	3.473	273.512	0.653	15.448	5.759	0.24	94709.	0.4199
25.16	0.4428	0.6127	0.1300	0.0940	0.367	5.790	3.356	274.012	0.654	14.928	5.555	0.24	95001.	0.3981
27.26	0.4797	0.6404	0.1249	0.0935	0.366	5.763	3.223	272.746	0.651	14.336	5.360	0.24	95311.	0.3764
29.35	0.5166	0.6656	0.1191	0.0925	0.362	5.698	3.075	269.659	0.644	13.679	5.173	0.24	95641.	0.3549
31.45	0.5535	0.6884	0.1129	0.0908	0.355	5.595	2.915	264.777	0.632	12.964	4.993	0.24	95989.	0.3334
33.55	0.5904	0.7086	0.1062	0.0885	0.346	5.455	2.743	258.158	0.616	12.199	4.819	0.24	96354.	0.3122
35.64	0.6273	0.7264	0.0992	0.0857	0.335	5.280	2.561	249.868	0.597	11.391	4.649	0.24	96738.	0.2910
37.74	0.6642	0.7415	0.0919	0.0823	0.322	5.071	2.371	239.968	0.573	10.547	4.482	0.24	97139.	0.2699
39.84	0.7011	0.7536	0.0842	0.0784	0.306	4.828	2.174	228.506	0.546	9.670	4.315	0.24	97557.	0.2489
41.93	0.7380	0.7625	0.0763	0.0739	0.289	4.554	1.971	215.520	0.515	8.766	4.148	0.24	97993.	0.2278
44.03	0.7749	0.7674	0.0683	0.0689	0.270	4.248	1.762	201.045	0.480	7.839	3.976	0.25	98445.	0.2065
46.12	0.8118	0.7676	0.0600	0.0635	0.248	3.912	1.549	185.112	0.442	6.891	3.796	0.25	98914.	0.1848
48.22	0.8487	0.7617	0.0516	0.0575	0.225	3.545	1.333	167.753	0.400	5.927	3.603	0.25	99400.	0.1627
50.32	0.8856	0.7472	0.0431	0.0511	0.200	3.149	1.113	149.009	0.356	4.950	3.387	0.25	99903.	0.1398
52.41	0.9225	0.7201	0.0345	0.0442	0.173	2.724	0.891	128.931	0.308	3.962	3.134	0.25	100422.	0.1157
54.51	0.9594	0.6725	0.0259	0.0369	0.144	2.273	0.668	107.592	0.257	2.969	2.814	0.25	100957.	0.0899
56.61	0.9963	0.5876	0.0172	0.0292	0.114	1.798	0.444	85.081	0.203	1.975	2.368	0.25	101508.	0.0617
58.70	1.0332	0.4206	0.0086	0.0211	0.082	1.300	0.222	61.513	0.147	0.986	1.634	0.25	102073.	0.0301
60.80	1.0701	0.0010	0.0000	0.0127	0.049	0.780	0.000	36.904	0.088	0.001	0.004	0.25	102639.	0.0000

Figure 4.3: Supplier data for the selected APC 15×13.5 three-blade propeller at 4000 rpm.

The aerodynamic profile of the selected propeller is based on the Clark Y airfoil, a conventional cambered section widely used in low Reynolds number applications. The operating range during the experiments was chosen between $\Omega = 419 \div 628$ rad/s (approximately $4000 \div 6000$ rpm), ensuring that the propeller operated within the motor capabilities while maintaining a realistic aerodynamic regime.

The main operating parameters adopted for the analysis are summarized below:

- Diameter: $D = 15'' = 0.381$ m $\quad \Rightarrow \quad R = 0.1905$ m,
- Rotational speed: $\Omega = 419 \div 628$ rad/s,
- Tip speed: $V_{tip} = \Omega R \approx 76 \div 114$ m/s,
- Chord: $c_{root} \approx 25$ mm, $c_{mid} \approx 27$ mm, $c_{tip} \approx 4.3$ mm,
- Twist: $\theta_{root} \approx 44°$, $\theta_{tip} \approx 14°$.

The corresponding rotor disk area is

$$A = \pi R^2 = \pi \cdot (0.1905)^2 \approx 0.114 \text{ m}^2.$$

The Reynolds number varies significantly along the blade span, depending on the local radius r and chord $c(r)$. Figure 4.4 shows the Clark Y section and the corresponding spanwise Reynolds number distribution in the selected operating range ($\Omega = 419 \div 628$ rad/s).

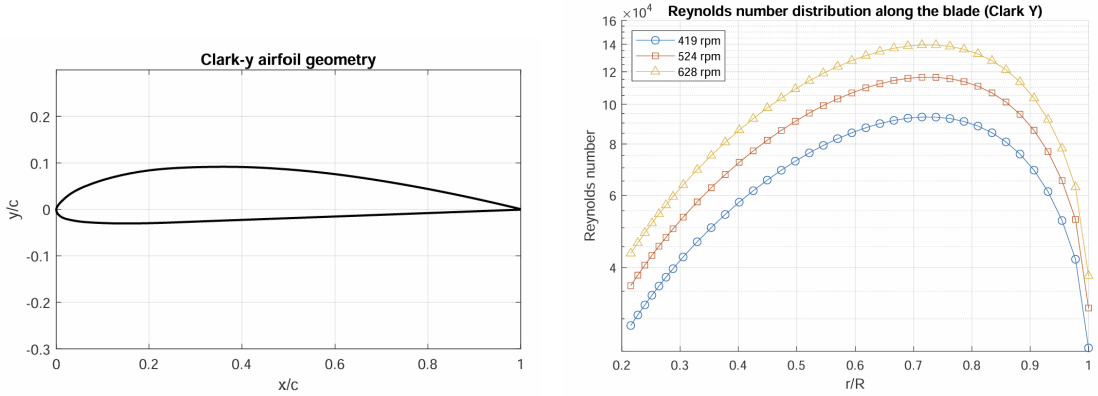

(a) Clark Y airfoil geometry.

(b) Reynolds distribution.

Figure 4.4: Clark Y profile (a) and Reynolds distribution along the span (b).

At the root ($r \approx 0.05$ m, $c \approx 25$ mm), the Reynolds number ranges from approximately 2.5×10^4 at $\Omega = 419$ rad/s to about 4.5×10^4 at $\Omega = 628$ rad/s. At mid-span ($r \approx 0.10$ m, $c \approx 27$ mm), it increases to $7 \times 10^4 \div 1.1 \times 10^5$, reaching a peak of $1.2 \times 10^5 \div 1.5 \times 10^5$ around $0.7R$, where the chord remains relatively large. Towards the tip ($r = 0.1905$ m, $c \approx 4.3$ mm), the Reynolds number decreases again to about $3 \times 10^4 \div 5 \times 10^4$. Overall, the blade operates in the range

$$Re \approx 2.5 \times 10^4 \div 1.5 \times 10^5,$$

with the most relevant aerodynamic sections lying between 7×10^4 and 1.5×10^5. All values were computed assuming sea-level conditions ($\rho = 1.225$ kg/m^3, $\nu = 1.5 \times 10^{-5}$ m^2/s).

To set a reference thrust level for the actuator disk analysis, the manufacturer's data at zero advance ratio ($V = 0$, i.e. hovering conditions) were considered. According to the tabulated curves, the thrust at $N = 4000$ rpm is 17.846 N, while at $N = 6000$ rpm it increases to 40.339 N. Therefore, the thrust range relevant to this study can be expressed as:

$$T = 17.846 \div 40.339 \text{ N}.$$

This interval was adopted as the reference range in the following calculations. Based on actuator disk theory, the induced velocity in hover is estimated as

$$v_i = \sqrt{\frac{T}{2\rho A}}, \tag{4.1}$$

which yields

$$v_i \approx 7.9 \div 12.0 \text{ m/s}.$$

The corresponding induced power is

$$P_i = T \cdot v_i, \tag{4.2}$$

Accounting for non-ideal effects with a correction factor of 1.25–1.5, the shaft power becomes

$$P_{shaft} \approx 178 \div 727 \text{ W}.$$

The torque at the motor shaft follows from

$$\tau = \frac{P_{shaft}}{\Omega}, \tag{4.3}$$

giving $\tau \approx 0.45 \div 0.53$ N m at $\Omega = 400$ rad/s and $\tau \approx 1.01 \div 1.21$ N m at $\Omega = 600$ rad/s. Assuming a motor efficiency of $\eta = 80\%$, the corresponding electrical power input is

$$P_{el} = \frac{P_{shaft}}{\eta}, \tag{4.4}$$

For a DC supply at constant voltage V, the current draw is then

$$I = \frac{P_{el}}{V}. \tag{4.5}$$

At $V = 24$ V, this results in $I = 9.3 \div 37.9$ A, while at $V = 48$ V it decreases to $4.6 \div 18.9$ A.

The actuator disk estimates are consistent with the manufacturer's performance data, which report a required shaft power of 216.5 W at $N = 4000$ rpm and 713.4 W at $N = 6000$ rpm. On this basis, the *Hacker A50-16 S* motor was selected, as it provides a sufficient power margin while remaining within safe operating limits.

(a) Hacker A50-16S motor.

A50-16 S V4 kv365					
Item no.: 15726839					
Propeller	Xoar 16x10	Xoar 16x12	RFM 17x10	RFM 17x13	RFM 18x11
LiPo	6S	6S	6S	6S	6S
Voltage [V]	23	23	22,2	22,2	22,2
Current [A]	60	69	60	71	70
Power [W]	1422	1590	1332	1576	1554
RPM	7559	7320	7150	6800	6850
Controller [A]	70-80	70-80	80-90	80-90	80-90
Timing [°]	20-25	20-25	20-25	20-25	20-25

(b) Supplier performance data.

Figure 4.5: Selected Hacker A50-16S motor and corresponding performance data.

Figure 4.5 shows the selected motor together with the corresponding manufacturer performance table. This configuration ensured adequate power availability for the complete test matrix, covering both out-of-ground and in-ground effect conditions.

4.1.2 Load cell

The thrust and torque generated by the propeller were measured using a *Flight Stand 15* load cell, a dedicated test bench for aerodynamic performance characterization of the propeller. A CAD model of the stand is shown in Fig. 4.6.

The main specifications of the load cell, summarized in Table 4.1, cover voltage, current, thrust, torque, and RPM ranges that fully encompass the operating conditions expected in the present work, thus ensuring safe and reliable measurements.

During the experiments, thrust, torque, and motor speed are recorded simultaneously. From these quantities, the input power and propeller efficiency can be derived, with the latter defined as

$$\eta_{\text{propeller}} = \frac{T \cdot v_{\text{air}}}{V \cdot I} \tag{4.6}$$

where T is the thrust, v_{air} the induced airflow velocity, and V, I the motor supply voltage and current.

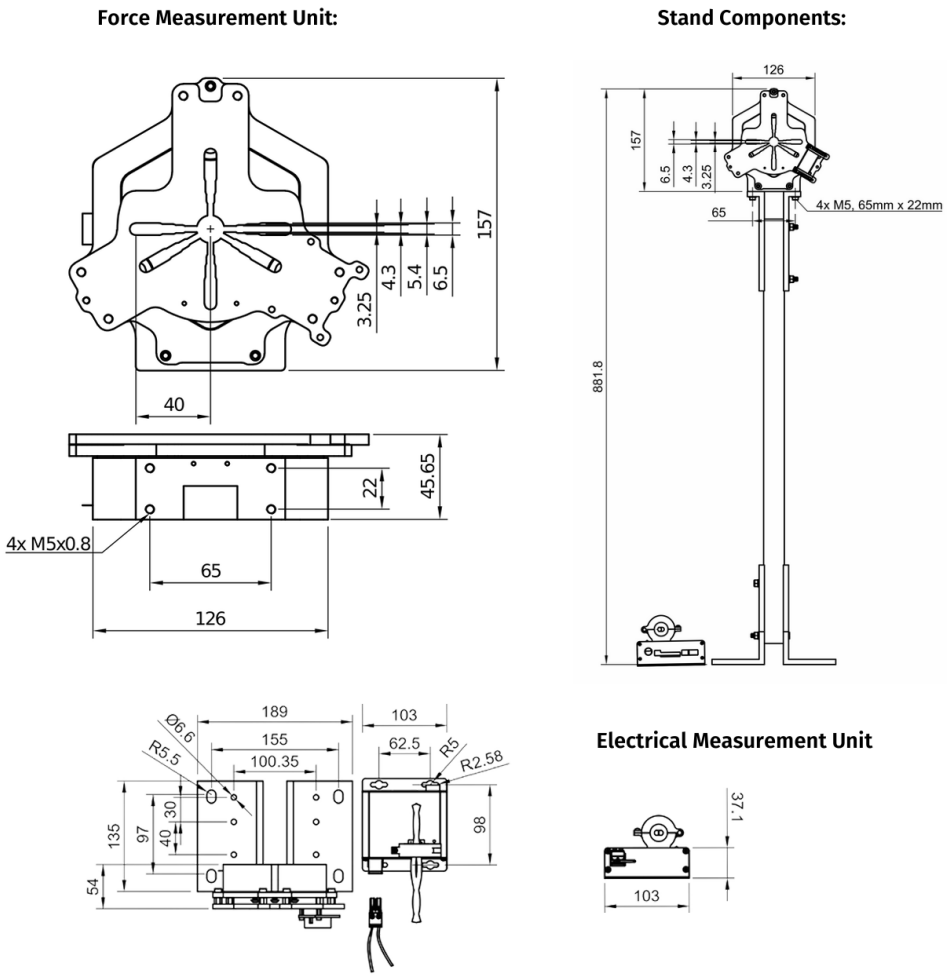

Figure 4.6: CAD model of the Flight Stand 15 load cell.

Parameter	Value
Voltage range	0 – 180 V (resolution 0.001 V)
Current range	0 – 150 A (resolution 0.001 A)
Thrust range	±150 N (resolution 0.05 N, accuracy ±1.5 N)
Torque range	±8 N m (resolution 0.005 N · m, accuracy ±0.1 N m)
RPM sensor range	400 – 30000 rpm (accuracy ±1 rpm)

Table 4.1: Main specifications of the Flight Stand 15 load cell (Standard version).

4.1.3 Power supply

For the experiments, a programmable DC power supply was adopted instead of a battery pack. This solution allows to deliver a stable voltage, to precisely control the current limit, and to continuously monitor the electrical parameters during operation. The supply voltage is selected according to the motor nominal range ($24 \div 48$ V). The current demand is not imposed directly, but results from the system load. From the estimates of Eq. (4.5), the expected current draw is:

$$I \approx 9.3 \div 37.9 \text{ A} \quad \text{at } 24 \text{ V},$$

$$I \approx 4.6 \div 18.9 \text{ A} \quad \text{at } 48 \text{ V}.$$

Accordingly, the current limit on the power supply was set slightly above these values (e.g. 40 A at 24 V), in order to provide sufficient margin while ensuring safe operation. Based on these considerations, a DC power supply rated up to 60 V and 40 A (2.4 kW) was selected, which comfortably covers the requirements of the propulsion system throughout the planned test campaign.

4.1.4 CAD and 3D printing

The CAD models developed for the experimental setup include all key components of the test rig: the propeller, the brushless motor, the load cell, the movable wall, the 3D-printed duct, the duct supports, the floor track, and the surrounding net enclosure. Each part was designed and assembled in *SolidWorks* to reproduce the real geometry of the laboratory configuration used during the tests. The complete assembly ensured proper alignment of the motor–propeller axis with the load cell, accurate positioning of the duct relative to the propeller, and sufficient clearances between all components.

Since the experiments were performed in the closed-circuit wind tunnel of RMIT University, which remained switched off during testing, the test chamber was represented in the CAD model as a permeable net enclosure. This design allowed the airflow to exit freely from the computational domain, avoiding artificial pressure build-up or wake recirculation while maintaining the correct geometric proportions of the experimental environment. The final CAD assembly, shown in Figure 4.7, includes the full test configuration as used in the laboratory, and was also adopted as the geometric reference for the subsequent numerical simulations.

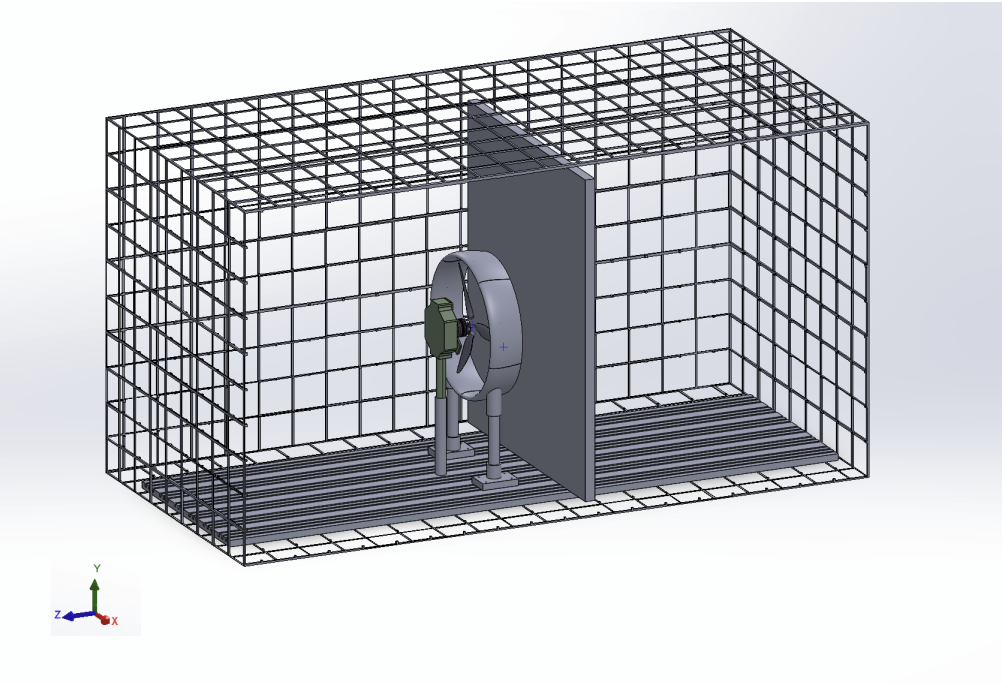

Figure 4.7: Complete CAD assembly of the experimental setup, including the propeller, motor, load cell, duct, supports, floor track, movable wall, and surrounding net enclosure.

Duct design

The duct geometry was designed following the work of Li et al. [17], where a NACA 0018 airfoil profile was identified as a suitable configuration for ducted rotors operating in hover. The airfoil section was scaled to match the three blade, 15 inch propeller adopted in the present study. The main geometric parameters of the duct are summarized below:

- Airfoil profile: NACA 0018
- Chord length: 100 mm
- Inner diameter: 408.9 mm
- Lip radius: 204.5 mm (measured from the duct center to the leading edge)
- Tip clearance: 2.6 % of the propeller radius (191 mm)

This configuration ensures geometric compatibility with the selected propeller while maintaining a compact aerodynamic profile. A small tip clearance was chosen to minimize leakage losses at the blade tips, which are known to significantly affect the overall efficiency of ducted propellers.

3D printing and assembly

The duct and its structural supports were manufactured using additive manufacturing techniques. All CAD components were exported in `.stl` format and processed in *Bambu Studio*, the slicing software used to generate the `.gcode` instructions for the printer. Due to the limited build volume, the duct was divided into multiple sections to allow fabrication and subsequent assembly. Before printing the complete model, the geometries were verified digitally to ensure dimensional compatibility between adjacent parts and correct alignment of the mounting interfaces.

Table 4.2 summarizes the components produced through 3D printing, including the duct sections, the supporting brackets, and the lower mounts used to attach the structure to the experimental rig.

Component	**Quantity**	**Description**
Duct section	2	Identical segments forming the main duct body
Support bracket	2	Elements with integrated attachment mounts
Lower mount	2	Brackets securing the duct to the floor track

Table 4.2: 3D-printed components included in the duct assembly.

Figure 4.8 shows the individual parts visualized in *Bambu Studio* during the slicing and preparation phase, including the duct, the support brackets, and the lower mounts. These digital checks ensured printability and proper dimensional matching before fabrication.

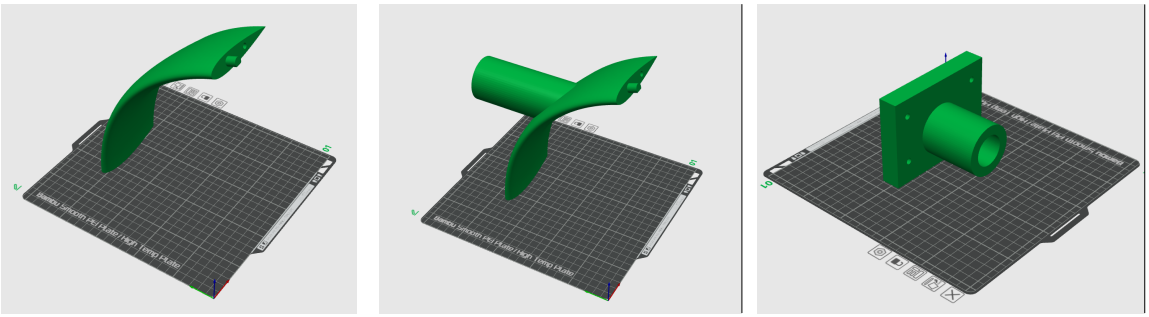

(a) Duct section. (b) Lower mounts. (c) Support bracket.

Figure 4.8: CAD components visualized in *Bambu Studio* before 3D printing.

Before assembling the final model, a small test piece was printed to verify the accuracy of the tolerances and ensure that the interfaces between adjacent parts matched correctly. Once the verification was successful, the full-scale duct sections were printed in Polylactic Acid (PLA), cleaned, and assembled using bolts and screws through the dedicated mounting supports. The complete 3D-printed duct was then mounted on the propeller and secured to the test rig, completing the preparation of the experimental apparatus.

(a) Duct profile NACA 0018.

(b) 3D-printed duct sections.

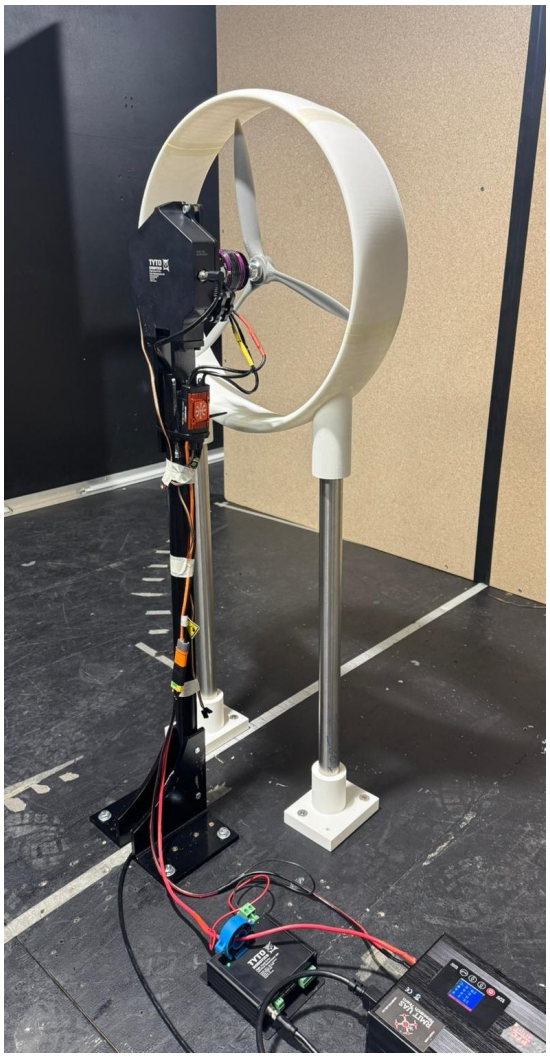

(c) Final 3D-printed duct.

Figure 4.9: Fabrication and assembly process of the 3D-printed duct. The smaller images (a) and (b) show intermediate printing and fit-verification steps, while (c) illustrates the completed duct installed on the propeller.

Chapter 5

Numerical Model and DUST Simulations

In parallel with the laboratory measurements, a numerical campaign was carried out using the aerodynamic solver *DUST*, with the aim of reproducing the behavior of the propeller both in and out of ground effect. The simulations were designed to replicate as closely as possible the experimental configuration, so that thrust and torque predictions could be directly compared with the measured data and with simplified analytical models.

5.1 Overview of the code

DUST (Downwash Unsteady Solver) is a mid-fidelity aerodynamic code developed at Politecnico di Milano [25]. The solver computes the unsteady potential flow around lifting and non-lifting bodies by coupling a vortex-particle wake formulation with a lifting-line blade representation. This approach enables an accurate prediction of wake roll-up, induced velocities, and boundary interactions, while maintaining a computational cost significantly lower than that of full Computational Fluid Dynamics (CFD) simulations [26], [27].

The underlying mathematical formulation is based on the Helmholtz decomposition of the velocity field, which separates the potential and vortical components of the flow. The potential part is solved through a boundary-value problem, while the free vorticity is represented by a mixed panel–vortex-particle model, providing a stable Lagrangian description of the wake suitable for configurations characterized by strong aerodynamic interactions, such as rotor–wall interference or multi-rotor coupling [25].

DUST therefore provides an effective compromise between simplified models such as Blade Element Momentum Theory (BEMT) and high-fidelity CFD approaches, achieving a favorable balance between computational efficiency and physical accuracy. The solver's modular architecture includes three main stages:

1. a pre-processor defining the geometry and discretization of the lifting surfaces,
2. a solver computing unsteady aerodynamic loads and induced velocities,
3. a post-processor for data extraction and visualization.

All simulation inputs, such as geometry, reference frames, aerodynamic polars, and solver parameters, are specified through structured text files, allowing flexible definition of different test configurations [26], [27].

5.1.1 Geometry generation in DUST

Within the pre-processing stage, the rotor geometry is defined through a structured parametric description. In *DUST*, the blade is divided into *sections* and *regions*, as illustrated in Figure 5.1 [28]. Each section is characterized by its chord, twist angle, and associated airfoil polar, while regions connect consecutive sections and prescribe their spanwise extent. This hierarchical structure enables complex geometries to be represented in a compact and easily editable format, facilitating rapid setup of different rotor configurations.

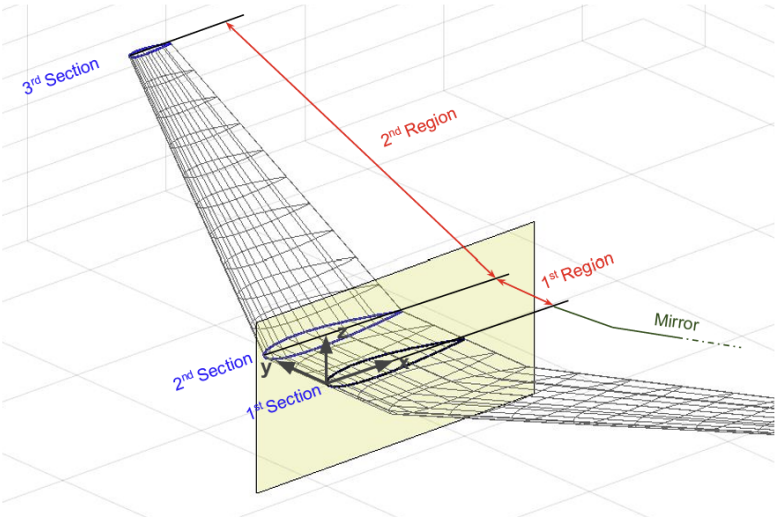

Figure 5.1: Sections and regions in parametric wing generation (from [28]).

Figure 5.2 provides a visual example of how these parametric elements are combined into the full three-dimensional blade geometry. The effect of local parameters such as twist and sweep can be clearly recognized, offering an intuitive interpretation of how sectional data translate into the actual blade surface.

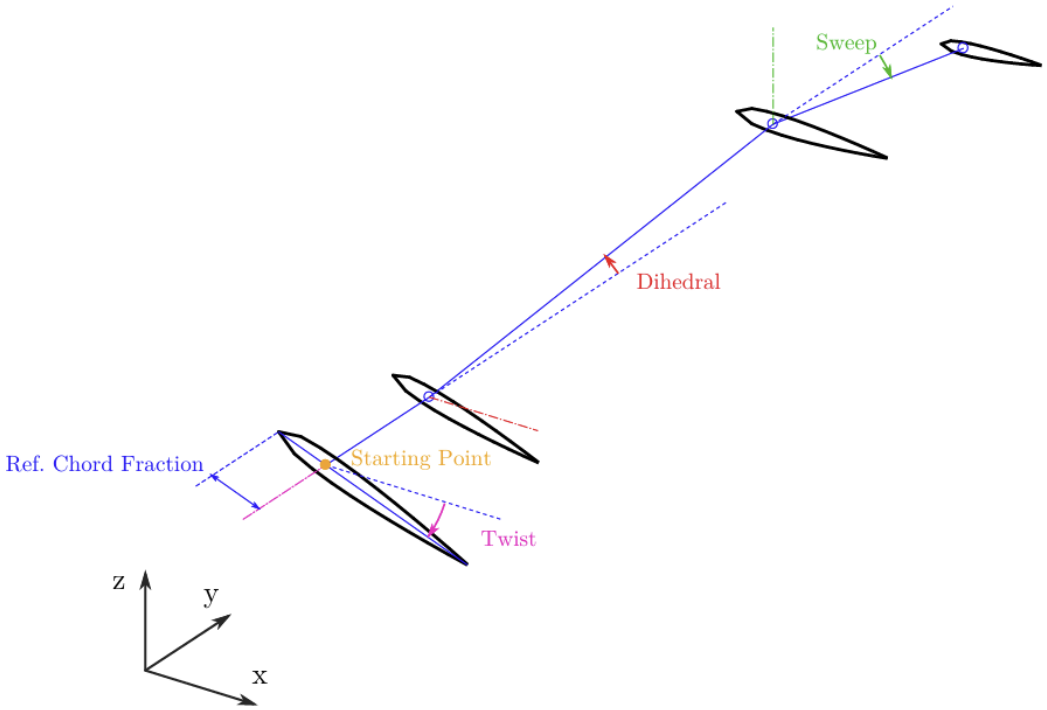

Figure 5.2: Generation logic of the geometry of parametric elements (from [28]).

To reproduce the geometry of the analyzed propeller, the blade parameters were derived from the manufacturer's data available on the *APC Propellers* website. The provided geometric information included the radial distributions of chord, twist, and sweep, which were used as the basis for the numerical model.

A preliminary analysis was conducted in `MATLAB` to examine the twist evolution along the blade span and to determine an appropriate segmentation of the lifting surface into discrete sections. Figure 5.3 illustrates the resulting twist distribution together with the selected section locations.

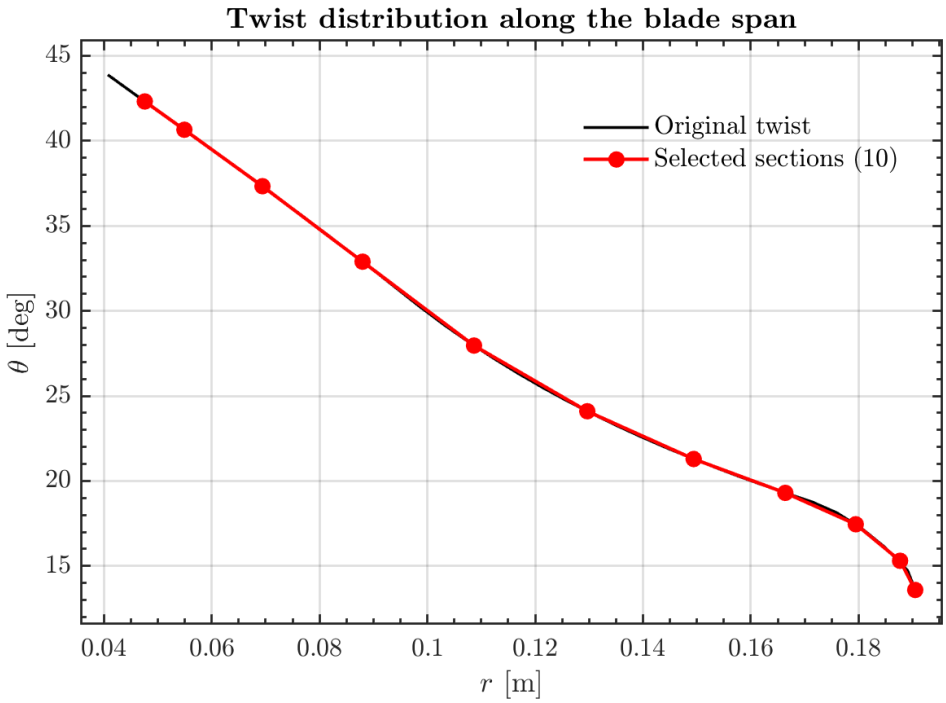

Figure 5.3: Twist distribution along the blade span derived from APC Propellers data. Red markers indicate the selected section locations used in *DUST*.

The radial discretization started at $y = 0.0448$ m from the hub, in order to avoid near-hub instabilities and ensure a smooth aerodynamic transition between adjacent regions. Each section was defined by its local chord and twist, while the connecting spanwise regions were characterized by their length, sweep angle, dihedral angle, and number of spanwise elements.

Along the chord, a uniform panel distribution with five elements was adopted (`nelem_chord = 5`, `type_chord = uniform`, reference point at `0.5` of the chord), providing a simple and numerically robust configuration. For completeness, other chordwise clustering options available in *DUST* are illustrated in Fig. 5.4 (from the DUST manual [28]), although they were not employed in this work.

The resulting blade geometry definition used in *DUST* is summarized in Table 5.1. All sections employ the CLARK Y airfoil (CLARKY.DAT with CLARKY.C81 aerodynamic tables), which were appropriately generated to cover the range of Mach and Reynolds numbers representative of the present propeller's operating conditions, while spanwise regions are uniformly divided into two elements each.

Section	**Chord [m]**	**Twist [°]**	**Span [m]**	**Sweep [°]**	**Dihedral [°]**	$n_{\textbf{span}}$
1	0.02537	42.317	0.00734	2.65	0.0	2
2	0.02577	40.653	0.01448	2.24	0.0	2
3	0.02653	37.334	0.01857	1.13	0.0	2
4	0.02717	32.895	0.02067	0.88	0.0	2
5	0.02694	27.963	0.02101	3.87	0.0	2
6	0.02511	24.101	0.01973	7.61	0.0	2
7	0.02136	21.294	0.01700	11.61	0.0	2
8	0.01614	19.303	0.01307	15.29	0.0	2
9	0.01066	17.456	0.01382	19.79	0.0	2
10	0.00625	15.310	–	–	–	–

Table 5.1: Blade geometry definition used in *DUST*. Sections are numbered from root to tip, each followed by its corresponding spanwise region.

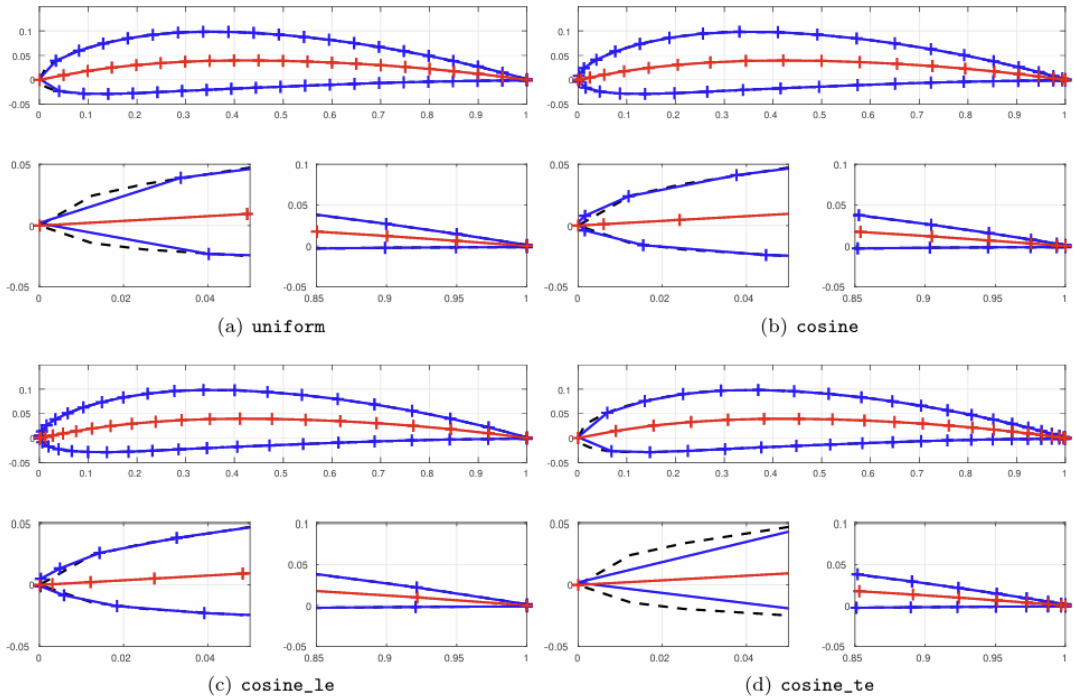

Figure 5.4: Chordwise discretization options for a NACA 4412 profile with 20 elements [28].

5.2 Airfoil polar generation (C81 files)

The aerodynamic polars required by DUST were generated using XFLR5, based on the same airfoil employed in the experimental propeller, namely the CLARK Y profile. Two dimensional analyses were performed with the XFOIL solver integrated in XFLR5, covering the ranges of Reynolds and Mach numbers representative of the propeller operating conditions.

Computations were carried out for Reynolds numbers between $Re = 9.0 \times 10^4$ and 1.5×10^5, corresponding to the chord–based values expected along the blade span for rotational speeds between 4000 and 6000 rpm. The Mach number was set to $M = 0.3$, while the amplification factor for transition was fixed to $N_{\text{crit}} = 9$, which corresponds to a low turbulence conditions typical of small scale propeller testing environments.

For each (Re, M) combination, the lift, drag, and moment coefficients (C_L, C_D, C_m) were computed over an angle of attack range from $-12°$ to $20°$. The results were post processed to smooth numerical oscillations and interpolated to produce a continuous data set in the .c81 format required by DUST.

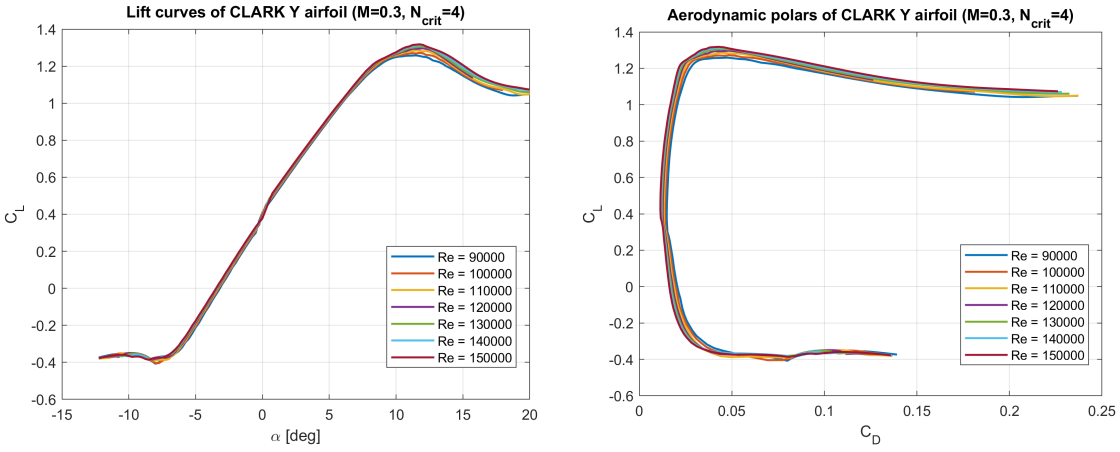

(a) Lift coefficient curves $C_L(\alpha)$ at different Reynolds numbers.

(b) Aerodynamic polars $C_L(C_D)$.

Figure 5.5: Aerodynamic polars of the CLARK Y airfoil obtained in *XFLR5*.

As shown in Figure 5.5, the lift curve remains approximately linear up to $\alpha \approx 10°$, beyond which the onset of flow separation causes a sharp drop in C_L. The maximum lift coefficient ranges between 1.25 and 1.3, with slightly higher values

at increasing Reynolds numbers.

The $C_L(C_D)$ polars show limited dispersion within the investigated Reynolds number range, confirming that the aerodynamic behaviour of the CLARK Y airfoil remains largely consistent in this regime. Nevertheless, a systematic trend can be observed upon closer inspection of the low-drag region: increasing Re results in a slight leftward translation of the curves, associated with a reduction in profile drag and a marginal improvement in the maximum aerodynamic efficiency $(C_L/C_D)_{\max}$.

5.3 Simulation parameters for the present study

This section details the numerical setup employed in DUST to reproduce the experimental conditions, with emphasis on the temporal resolution, blade discretization, and implementation of the image method. The main parameters are summarized below.

1. The time step Δt was chosen such that each rotor revolution was discretized into approximately 100 steps, ensuring adequate resolution of the unsteady wake dynamics. Each case was advanced for about five revolutions, corresponding to a total of $500 \div 510$ iterations depending on the angular velocity.

2. The propeller geometry was provided via the `blade.in` file and discretized according to Table 5.1.

3. To reproduce the ground effect, the image method available in DUST was adopted. The mirroring was implemented directly in the `blade_mirror.in` file by activating the option `mesh_mirror = T` and specifying the plane `mirror_normal = (/0.0, 0.0, 1.0/)`. In this way, the lower rotor acted as a specular copy of the upper one: it did not contribute thrust directly, but reproduced the aerodynamic influence of the reflecting ground plane through wake interaction.

4. The angular velocity ω was varied between 419, 524 and 628 rad/s to explore the effect of RPM on aerodynamic loads. For each value of ω, the rotor was simulated at different ground clearances $h/R = 0.26$, 0.39, 0.52, 0.65, 0.78, 1.05, 1.31, and 1.57, where $R = 0.191$ m is the rotor radius.

5. The aerodynamic polars used in DUST were generated by post-processing the airfoil data obtained from XFLR5. Lift, drag and moment coefficients were exported for the range of Reynolds and Mach numbers relevant to the present operating conditions, and subsequently converted into the .c81 format required by DUST.

Parameter	Value
Propeller radius R	0.191 m
Number of blades	3
Rotational speeds ω	419, 524, 628 rad/s
Ground clearance ratios h/R	0.26, 0.39, 0.52, 0.65, 0.78, 1.05, 1.31, 1.57
Number of revolutions	≈ 5
Time step Δt	$\approx 1.20 \times 10^{-4}$ s (for $\omega = 524$ rad/s, 100 steps/rev)
Steps per revolution	≈ 100
Chordwise elements n_{chord}	5
Airfoil polars	CLARKY.c81 (from XFLR5 generated polars)
Post-processing tools	ParaView, MATLAB (BEM comparison)

Table 5.2: Summary of DUST simulation parameters for the ground-effect study.

5.4 Post-processing of Simulation Data

The numerical results obtained from DUST were analyzed using two complementary tools: ParaView and MATLAB. ParaView was employed to visualize the wake topology and to qualitatively verify the consistency of the simulated flow field, while MATLAB was used for quantitative post processing of the solver output. This combined approach allowed both a physical validation of the setup and a reliable numerical evaluation of aerodynamic performance.

5.4.1 Flow visualization in ParaView

ParaView was employed to visualize the vorticity and induced velocity fields, providing a qualitative verification of the numerical setup and the overall wake development. The post-processing allowed to confirm:

- the correct sense of rotation of both the real and mirrored propellers,
- the expected direction of the thrust vector and wake inclination,
- the formation of a coherent and symmetric wake pattern in the mirrored configuration, representative of the ground effect.

In the simulation, the two rotors rotate in the same direction, as imposed by the mirror boundary condition, so that the mirrored rotor reproduces the reflection of

the flow field rather than a counter-rotating configuration. The wake structures generated by the real and mirrored rotors interact near the symmetry plane, forming a circular and stable induced velocity distribution when observed from above. This behavior confirms the physical consistency of the mirror-plane approach adopted to model the ground surface.

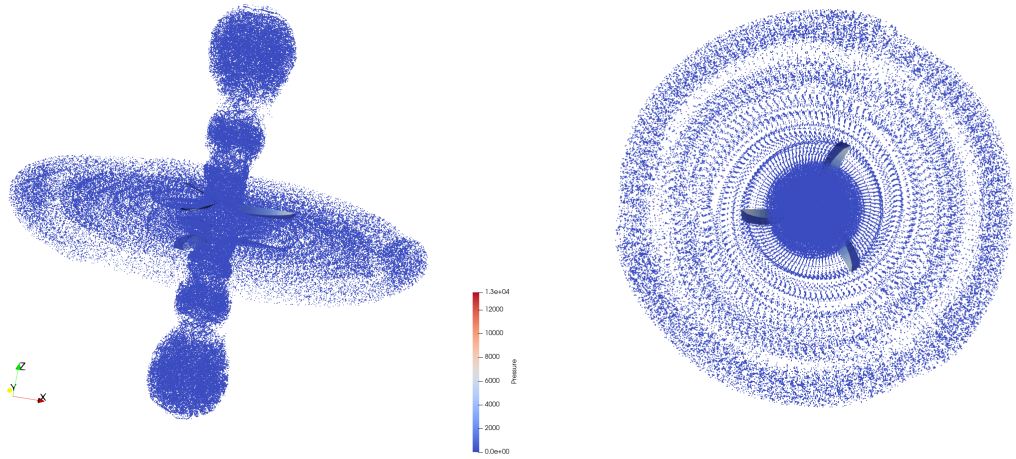

Figure 5.6: Flow visualization in *ParaView* for the case $\omega = 524$ rad/s and $h/R = 0.26$. (a) Side view showing the mirrored rotor configuration and the wake interaction near the symmetry plane. (b) Top view illustrating the circular and symmetric wake pattern, confirming the correct reproduction of the ground effect.

5.4.2 Quantitative post processing in MATLAB

MATLAB scripts were developed to process the solver output, extracting the time histories of thrust T, torque Q, and power P. Since the wake requires a transient period to stabilize, only the final value of each time history, after reaching steady conditions, was considered for the analysis.

The scripts automated:

– loading and parsing of DUST output files,

– plotting of temporal convergence curves,

– extraction of the steady–state value for each quantity.

This ensured a consistent and reliable evaluation of aerodynamic performance in all simulated cases. As an example, Figure 5.7 illustrates the temporal evolution of thrust and torque for the case at $\omega = 524$ rad/s and $h/R = 0.26$, showing that the solution reaches steady conditions after approximately two and a half revolutions of the rotor (about 0.03 s of the simulated time). Once the transient wake development was completed, the final value of each signal was extracted and used for the quantitative comparison between different operating conditions.

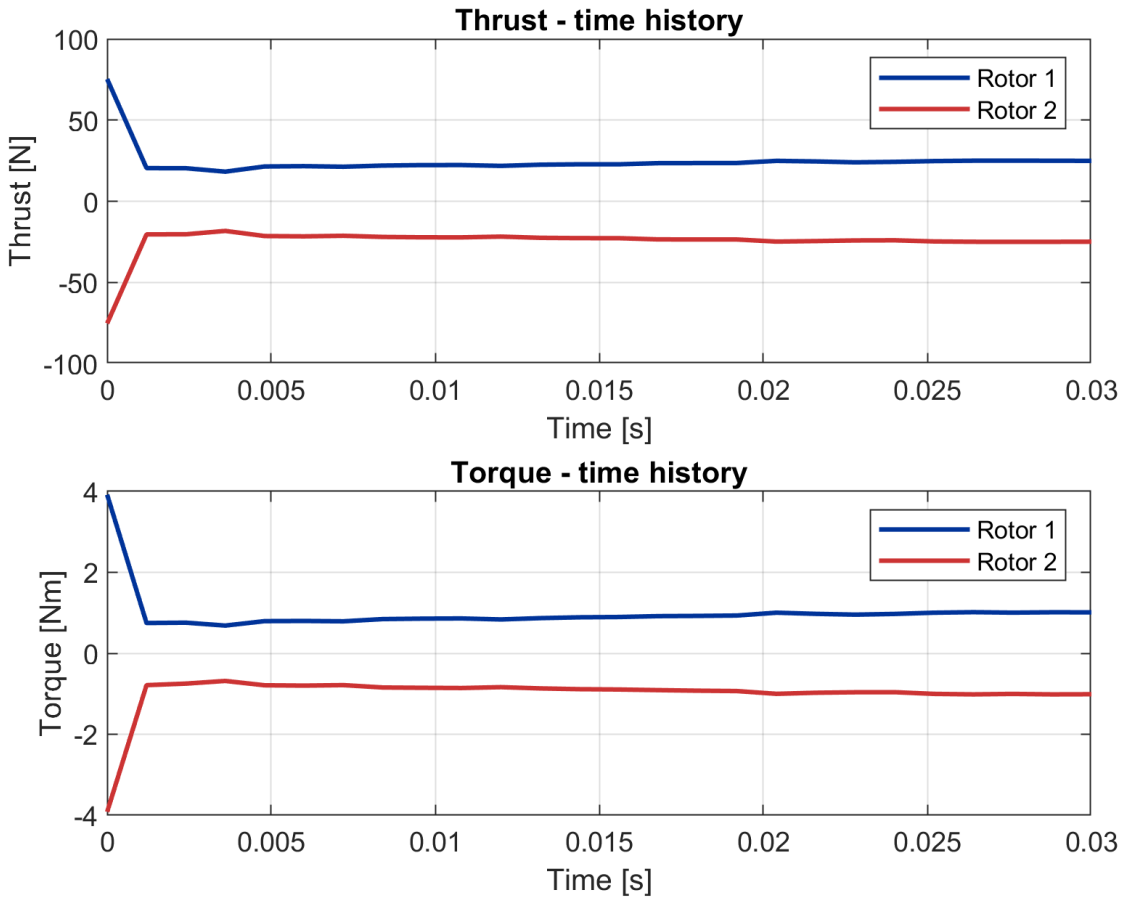

Figure 5.7: Temporal convergence of thrust and torque for $\omega = 524$ rad/s and $h/R = 0.26$. In the legend, Rotor 1 corresponds to the actual propeller, while Rotor 2 is the mirrored rotor used in DUST to model the ground effect.

Once the solver convergence was verified, the out of ground effect (OGE) configuration was first analyzed to validate the numerical setup. This preliminary step aimed to assess the ability of the *DUST* solver to predict propeller performance under hover conditions, prior to introducing ground proximity effects.

Table 5.3 presents the comparison between the numerical predictions and the reference data provided by the manufacturer, in terms of thrust, torque and power at different angular velocities. The agreement is satisfactory across the considered operating range: discrepancies in thrust decrease with increasing rotational speed, falling from about 17.5% at low ω to below 11.36% at higher values. Torque and power predictions remain within 9.63% of the reference data throughout the range. This validation confirms the reliability of the aerodynamic model implemented in *DUST* and provides a solid foundation for the subsequent analysis of ground effects.

ω [rad/s]	Thrust [N]			Torque [Nm]			Power [W]		
	DUST	Ref	Err [%]	DUST	Ref	Err [%]	DUST	Ref	Err [%]
419.0	14.73	17.85	17.45	0.558	0.517	7.88	233.70	216.50	7.94
524.0	23.81	27.95	14.82	0.873	0.796	9.63	456.39	416.62	9.55
628.0	35.76	40.34	11.36	1.215	1.135	7.07	763.19	713.44	6.97

Table 5.3: Comparison between DUST results and manufacturer reference data.

After validating the out of ground effect performance, the simulations in ground effect (IGE) were analyzed. Table 5.4 summarizes the steady state thrust values at different h/R ratios and angular velocities, allowing a direct quantification of the influence of ground proximity on the rotor performance.

ω [rad/s]	T_{IGE} [N] at different h/R							
	h/R 0.26	h/R 0.39	h/R 0.52	h/R 0.66	h/R 0.79	h/R 1.05	h/R 1.31	h/R 1.57
419.0	13.24	15.26	15.70	16.13	15.93	15.50	14.87	14.79
524.0	21.34	24.15	25.91	25.59	25.26	25.39	24.08	24.49
628.0	31.98	35.19	37.59	37.46	38.29	36.73	36.23	36.03

Table 5.4: T_{IGE} at different angular velocities and ground clearances.

Finally, Figure 5.8 reports the ratio $T_{\mathrm{IGE}}/T_{\mathrm{OGE}}$ as a function of the normalized clearance h/R. The trend obtained with DUST is compared with the analytical model by Cheeseman and Bennett, previously introduced in Section 2.6.

As recalled in Equation (2.27), the model predicts the thrust increment in ground effect as

$$\frac{T_{IGE}}{T_{OGE}} = \frac{1}{1 - \left(\frac{R}{4h}\right)^2},$$

and is considered valid for $h/R > 0.25$.

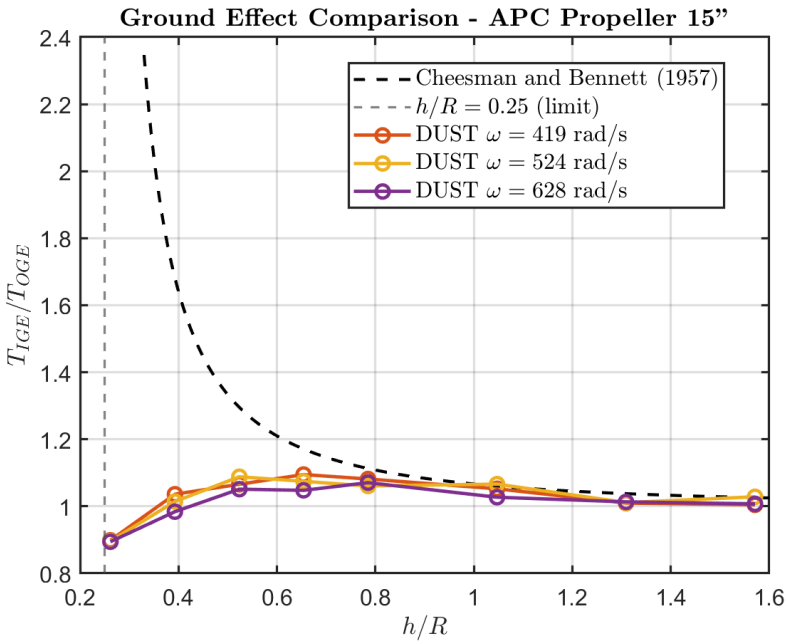

Figure 5.8: Comparison between DUST predictions and Cheeseman-Bennett model. The ratio $T_{\mathrm{IGE}}/T_{\mathrm{OGE}}$ is plotted as a function of h/R. The vertical dashed line indicates the validity limit of the analytical model ($h/R = 0.25$).

The *DUST* results confirm that the solver accurately reproduces the overall trend of thrust reduction as the propeller moves away from the ground, with the thrust ratio approaching unity at large clearances, independently of the rotational speed. For smaller separations ($h/R < 0.8$), however, the numerical predictions underestimate the thrust enhancement compared with the analytical correlation of Cheeseman and Bennett, whose curve diverges more rapidly as the rotor approaches the wall. This discrepancy highlights the inherent limitations of mid-fidelity potential-flow solvers, in which viscous dissipation, tip vortices, and strong wake–ground interactions are only partially represented.

The correlation proposed by Cheeseman and Bennett (1957) [2] was originally derived to describe the ground effect behavior of large scale helicopter rotors operating in hover. Being based on actuator disk theory, it assumes an ideal, uniformly loaded rotor. Although this formulation provides an accurate reference for conventional rotors, it is not fully representative of small-scale propellers such as the APC 15"×13.5"x3 analyzed in the present work, whose higher rotational speeds and moderate geometric twist produce a more complex, non uniform inflow distribution. Consequently, the analytical model tends to overpredict the thrust augmentation in ground effect, particularly at low clearances.

5.5 Sensitivity to Blade Twist and Pitch Influence on the Ground Effect

To better understand whether the observed non-monotonic behavior of the thrust ratio could be influenced by the propeller twist distribution, a dedicated sensitivity analysis was performed. The objective was to determine whether the variations in thrust observed near the ground were affected by the local blade geometry rather than by the numerical inaccuracies of the solver.

A review of the literature confirmed that the pitch to diameter ratio γ/D plays a crucial role in determining the aerodynamic response in ground effect. In particular, Cai [29] conducted a systematic experimental study on the influence of propeller pitch using several APC propellers of 17 inches diameter and different pitches (17"×7", 17"×10" and 17"×12"). His results demonstrated that as γ/D increases, the classical ground effect, typically characterized by enhanced thrust and reduced power consumption near the ground, progressively weakens and may even invert. Low pitch propellers ($\gamma/D \approx 0.41$) exhibited the strongest thrust augmentation, whereas high pitch configurations ($\gamma/D \approx 0.71$) displayed minimal or even negative variations in thrust when operating close to the ground. This trend is consistent with the present experimental and numerical results for the APC 15"×13.5"×3, which features an exceptionally high ratio $\gamma/D = 13.5/15 \approx 0.9$.

To further investigate this effect numerically, a series of DUST simulations were carried out, systematically reducing the pitch and the corresponding twist distribution of the baseline geometry. The methodology adopted to scale the twist follows the helical pitch relationship, ensuring geometric consistency across all sections of the blade.

1. Geometric Relationship Between Pitch and Twist

For a propeller of radius R, the *local geometric pitch* $P(r)$ at a radial distance r represents the axial advance per revolution of the helical surface traced by the airfoil section. From the helical geometry, the local blade angle $\beta(r)$ (twist angle) measured between the chord line and the plane of rotation, is defined as:

$$\tan\beta(r) = \frac{P(r)}{2\pi r}$$

Inverting this relation gives:

$$\beta(r) = \arctan\left(\frac{P(r)}{2\pi r}\right)$$

If the pitch is uniformly scaled by a constant factor k, such that $P^*(r) = k\,P_0(r)$, the new local twist angle becomes:

$$\tan\beta_{\text{new}}(r) = k\,\tan\beta_{\text{old}}(r)$$

and consequently:

$$\boxed{\beta_{\text{new}}(r) = \arctan\Big(k\,\tan\beta_{\text{old}}(r)\Big)}$$

This expression preserves the shape of the original twist distribution while uniformly reducing the effective helical pitch along the blade span. It therefore provides a physically consistent way to analyze the influence of pitch and twist without altering other geometric parameters such as chord or sweep. The scaling factor k is defined as the ratio between the desired pitch P^* and the original pitch P_0:

$$k = \frac{P^*}{P_0}$$

For the baseline APC 15"×13.5"×3 propeller, $P_0 = 13.5''$. Four configurations were defined to systematically explore the sensitivity of the ground effect:

- **Case 1:** $P^* = 0\,\text{in} \quad \Rightarrow \quad k = 0.00$
- **Case 2:** $P^* = 6.5\,\text{in} \quad \Rightarrow \quad k = 0.48$
- **Case 3:** $P^* = 9.5\,\text{in} \quad \Rightarrow \quad k = 0.71$
- **Case 4:** $P^* = 13.5\,\text{in}$ (baseline) $\Rightarrow \quad k = 1.00$

In each case, the twist angle at every radial station was recalculated according to the above expression, ensuring a consistent variation of the local blade incidence with respect to the reference geometry. This approach enables an isolated analysis of the aerodynamic influence of pitch, maintaining the same planform, airfoil sections, and chord distribution.

The new twist distributions were implemented in the *DUST* input files by applying the computed k values to the baseline geometry provided by APC. The scaling process was fully parametric: each section retained its original chord and airfoil, while the twist angles were modified through the function

$$\beta_{\text{new}}(r_i) = \arctan(k \tan(\beta_{\text{old}}(r_i))).$$

This modification allowed the simulation of propellers with progressively lower geometric pitch, while preserving the radial variation of aerodynamic loading.

2. Paraview visualization

The four propeller geometries were imported into ParaView to visually verify the applied twist scaling. By superimposing the models in a common reference frame, the progressive reduction of the helical angle with decreasing pitch was clearly observed. The visualization confirmed that the scaling procedure was correctly implemented before running the DUST simulations.

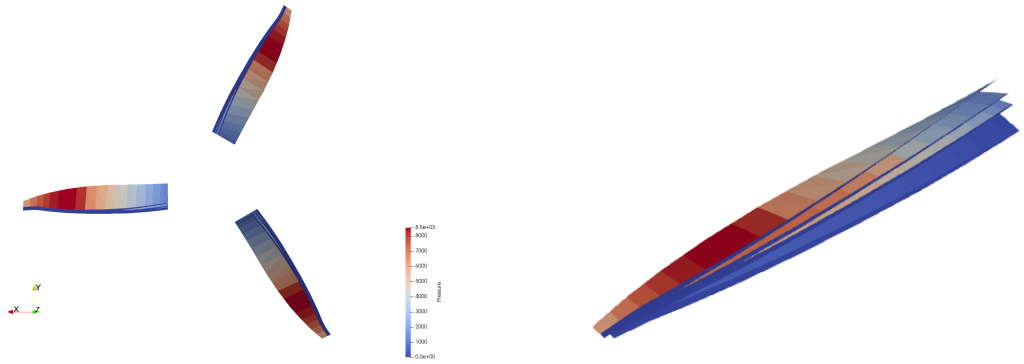

Figure 5.9: Visualization in ParaView of the four propeller configurations. The close-up image on the right highlights the variation in twist angle along the span.

3. Numerical Results

Figure 5.10 shows the comparison between the DUST predictions for the four analyzed configurations and the analytical correlation of Cheeseman and Bennett (1957).

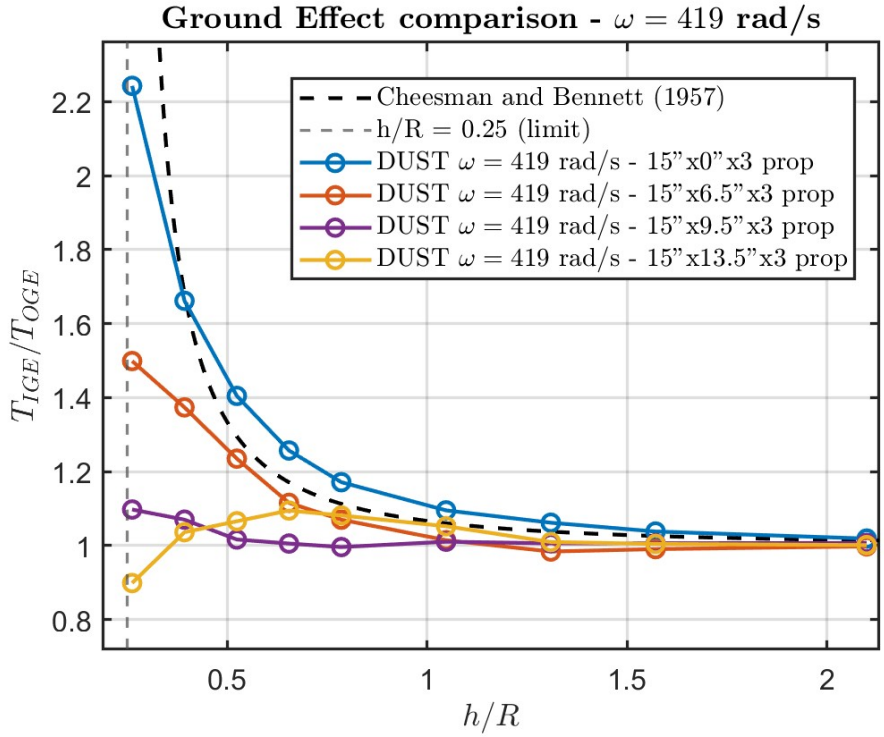

Figure 5.10: Effect of geometric pitch and blade twist on the thrust ratio $T_{\mathrm{IGE}}/T_{\mathrm{OGE}}$ as a function of h/R. The DUST results for the four pitch values are compared with the analytical correlation of Cheeseman and Bennett (1957). Lower pitch configurations show stronger ground effect enhancement, while the high-pitch baseline (13.5 in) exhibits a weaker or slightly negative variation near the ground.

The results indicate a clear dependency of the ground effect on the geometric pitch: as the pitch (and thus the twist) decreases, the thrust ratio $T_{\mathrm{IGE}}/T_{\mathrm{OGE}}$ increases, converging toward the analytical prediction. In particular, the trends reveal that lower-pitch configurations exhibit stronger ground effect enhancement, closely following the analytical model.

Conversely, the baseline high-pitch propeller (13.5") shows a weaker and slightly negative variation of the thrust ratio near the ground, consistent with the observations reported by Cai (2020) [29]. This behavior is attributed to the

increased tangential component of the induced velocity, which diminishes the vertical inflow and consequently the pressure recovery on the lower side of the disk.

Overall, the numerical results confirm that the ground effect is strongly influenced by the propeller's helical pitch and twist distribution. As the pitch decreases, the spanwise loading becomes more uniform and the propeller approaches the ideal actuator-disk behavior assumed by Cheeseman and Bennett. In contrast, the high-pitch configuration produces a more non-uniform inflow and stronger tangential velocity components, both of which suppress the thrust augmentation typically induced by proximity to the ground.

5.5.1 Collective Pitch Normalization for Thrust-Matched Comparison

While the previous simulations directly compared geometries with different geometric pitch, the resulting thrust levels in out-of-ground-effect (OGE) conditions were not identical. To perform a fair assessment of the ground effect sensitivity, all configurations were therefore normalized to deliver the same thrust in OGE at a constant rotational speed ($\omega = 419\ \mathrm{rad\,s^{-1}}$).

The baseline configuration is the 15"×13.5" propeller, producing a reference thrust of $T^\star = 14.73\,\mathrm{N}$. For each other geometry (15"×9.5", 15"×6.5", 15"×0"), a uniform collective pitch offset, $\Delta\theta_{\mathrm{coll}}$, was applied such that

$$T(\Delta\theta_{\mathrm{coll}}; \omega, \mathrm{OGE}) = T^\star, \tag{5.1}$$

while maintaining identical chord, airfoil, and mesh parameters. The new twist distribution for each blade section was obtained as:

$$\beta_{\mathrm{new}}(r) = \beta_{\mathrm{geom}}(r) + \Delta\theta_{\mathrm{coll}}, \tag{5.2}$$

ensuring a pure collective trim without changing the differential twist.

The collective offsets required to match the baseline thrust were found to be:

$$\Delta\theta_{\mathrm{coll}} = \begin{cases} +6.01^\circ & (15"\times 9.5") \\ +10.15^\circ & (15"\times 6.5") \\ +20.30^\circ & (15"\times 0") \end{cases}$$

and the resulting section-by-section twists are summarized in Tables 5.5.1.

15"×9.5" ($\Delta\theta_{\text{coll}} \approx +6.01°$)

Section	1	2	3	4	5	6	7	8	9	10
β_{geom} [deg]	29.79	28.62	26.28	23.16	19.69	16.97	14.99	13.59	12.29	10.78
β_{new} [deg]	35.80	34.63	32.29	29.17	25.69	22.98	21.00	19.59	18.29	16.79

15"×6.5" ($\Delta\theta_{\text{coll}} \approx +10.15°$)

Section	1	2	3	4	5	6	7	8	9	10
β_{geom} [deg]	21.16	20.33	18.67	16.45	13.98	12.05	10.65	9.65	8.73	7.65
β_{new} [deg]	31.31	30.48	28.82	26.59	24.13	22.20	20.79	19.80	18.88	17.81

15"×0" ($\Delta\theta_{\text{coll}} \approx +20.30°$)

Section	1	2	3	4	5	6	7	8	9	10
β_{geom} [deg]	0.00	0.00	0.00	0.00	0.00	0.00	0.00	0.00	0.00	0.00
β_{new} [deg]	20.30	20.30	20.30	20.30	20.30	20.30	20.30	20.30	20.30	20.30

Figures 5.11 and 5.12 show the distributions of thrust and torque per unit radius (dT/dr and dQ/dr) for the four propellers at 4000 rpm. These quantities represent the local aerodynamic loading along the blade span and are directly proportional to the sectional lift and moment generated by each blade element.

The comparison confirms that, following the collective pitch trimming procedure, all configurations deliver equivalent overall thrust while maintaining consistent aerodynamic behavior along the span.

The physical interpretation of these distributions can be understood from the local momentum balance. For an infinitesimal blade element located at a distance r from the hub, the incremental thrust and torque can be expressed as:

$$\frac{dT}{dr} = \tfrac{1}{2}\,\rho\,(\Omega r)^2\,c(r)\,C_L(r)\,F_{\text{tip}}(r), \qquad \frac{dQ}{dr} = \tfrac{1}{2}\,\rho\,(\Omega r)^2\,c(r)\,C_D(r)\,r\,F_{\text{tip}}(r),$$

where ρ is the air density, Ω the angular velocity, $c(r)$ the local chord, $C_L(r)$ and $C_D(r)$ the sectional lift and drag coefficients, and $F_{\text{tip}}(r)$ the Prandtl tip–loss correction factor. The term $(\Omega r)^2$ causes the aerodynamic loading to increase rapidly with radius, while the reduction in chord, blade twist, and tip efficiency progressively limits this growth.

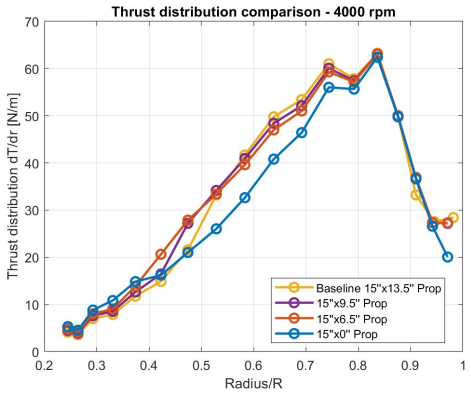

Figure 5.11: Thrust distribution per unit radius at 4000 rpm for the four propellers. The peak load occurs around $r/R \simeq 0.85$, followed by a tipwise decay due to twist reduction and tip–vortex losses.

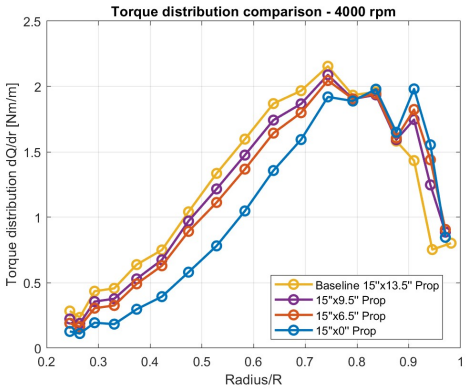

Figure 5.12: Torque distribution per unit radius at 4000 rpm. The pattern mirrors the thrust trend, confirming consistent aerodynamic behavior and uniform trimming across all configurations.

The maximum of $\frac{dT}{dr}$ is located in the outer region of the blade, approximately between $r/R = 0.7$ and 0.85. In this zone, the increase in tangential velocity with radius, proportional to $(\Omega r)^2$, is balanced by the gradual decrease of the local chord $c(r)$, lift coefficient $C_L(r)$, and the tip–loss factor $F_{\text{tip}}(r)$. This equilibrium produces the characteristic "bell–shaped" load distribution, with a peak where aerodynamic loading and rotational speed achieve an optimal balance. Beyond this region, the combined effect of decreasing incidence, smaller chord, and stronger tip–vortex losses leads to a rapid decay in both thrust and torque per unit radius [8].

All configurations in Figures 5.11 and 5.12 exhibit the typical bell–shaped behavior, with a maximum around $r/R \simeq 0.8{-}0.85$, corresponding to the region of highest aerodynamic efficiency. However, the amplitude and slope of the distributions vary systematically with the blade pitch.

The high–pitch propeller (15"×13.5"×3), shown by the yellow line, exhibits lower thrust loading in the inner portion of the blade ($r/R < 0.45$) and a stronger concentration toward the outer span. The distribution rises sharply between $r/R = 0.6$ and 0.8, then decays rapidly near the tip, indicating that the aerodynamic forces are dominated by the outer sections, where the local inflow angle is smaller and the induced velocity is mainly tangential. As a result, the vertical component of the induced flow is weaker, and the propeller's sensitivity to ground proximity is reduced, in agreement with the lower $T_{\text{IGE}}/T_{\text{OGE}}$ ratios

observed.

Conversely, the low–pitch configuration (15”×0”×3, blue line) shows higher thrust near the hub ($r/R < 0.4$), followed by a gradual decrease up to $r/R \simeq 0.85$ and a steep drop toward the tip. This broader but less intense loading pattern reflects a greater axial component of the induced velocity and a more actuator–disk–like behavior, leading to stronger flow recirculation and higher $T_{\mathrm{IGE}}/T_{\mathrm{OGE}}$ values.

Intermediate pitches, such as the 15”×9.5”×3 and 15”×6.5”×3 propellers, display smoother and flatter profiles that bridge these two behaviors. Their dT/dr and dQ/dr distributions remain close to the baseline but with slightly lower peaks, confirming that decreasing pitch promotes a more uniform aerodynamic loading and a stronger influence of the ground on the propeller inflow.

The resulting twist distributions after applying the collective pitch offsets were compared, as shown in Figure 5.13.

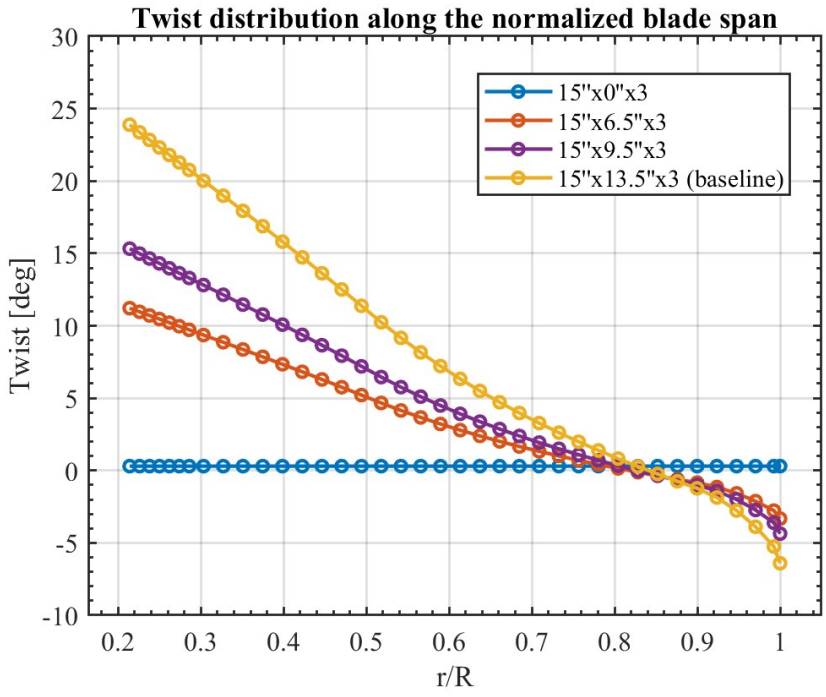

Figure 5.13: Comparison of the twist distributions after applying the collective pitch offsets. All curves intersect around $r/R \approx 0.8$, indicating that the collective normalization aligns the aerodynamic incidence near the most effective blade region.

As expected, increasing the nominal pitch shifts the entire twist curve upward, while preserving a nearly linear radial trend. The baseline configuration (15”×13.5”×3) exhibits the highest twist at the root, reaching values above 25°, which gradually decrease toward a slightly negative incidence near the tip. This strong geometric twist ensures an approximately uniform angle of attack along the span when operating at high pitch settings.

For intermediate pitches (15”×9.5”×3 and 15”×6.5”×3), the overall incidence level is reduced, but a moderate twist gradient is still preserved, ensuring proper aerodynamic loading along the span. In contrast, the lowest–pitch configuration (15”×0”×3) displays a constant twist of zero degrees across the entire radius. This case represents an idealized, actuator–disk–like geometry, characterized by a uniform pitch angle and a purely collective aerodynamic response, where the loading is determined solely by the induced velocity distribution rather than by geometric twist.

The consistent linearity between curves confirm that the collective pitch offsets were applied uniformly across all geometries, in accordance with:

$$\beta_{\text{new}}(r) = \beta_{\text{geom}}(r) + \Delta\theta_{\text{coll}}.$$

This ensures that the trimming procedure modified the blades through a pure collective rotation, without altering the radial twist gradient. Consequently, the aerodynamic differences observed in the thrust and torque distributions directly arise from the variation in collective incidence, rather than from geometric inconsistencies along the span.

Ground Effect Analysis

With the trimmed twist distributions and constant speed, a new ground-effect analysis was performed for

$$h/R \in \{0.2617,\ 0.3927,\ 0.5236,\ 0.654,\ 0.785,\ 1.047,\ 1.309,\ 1.571,\ 2.099\}.$$

The thrust was extracted and normalized with respect to the out-of-ground-effect (OGE) value as $\dfrac{T_{\text{IGE}}}{T_{\text{OGE}}}$.

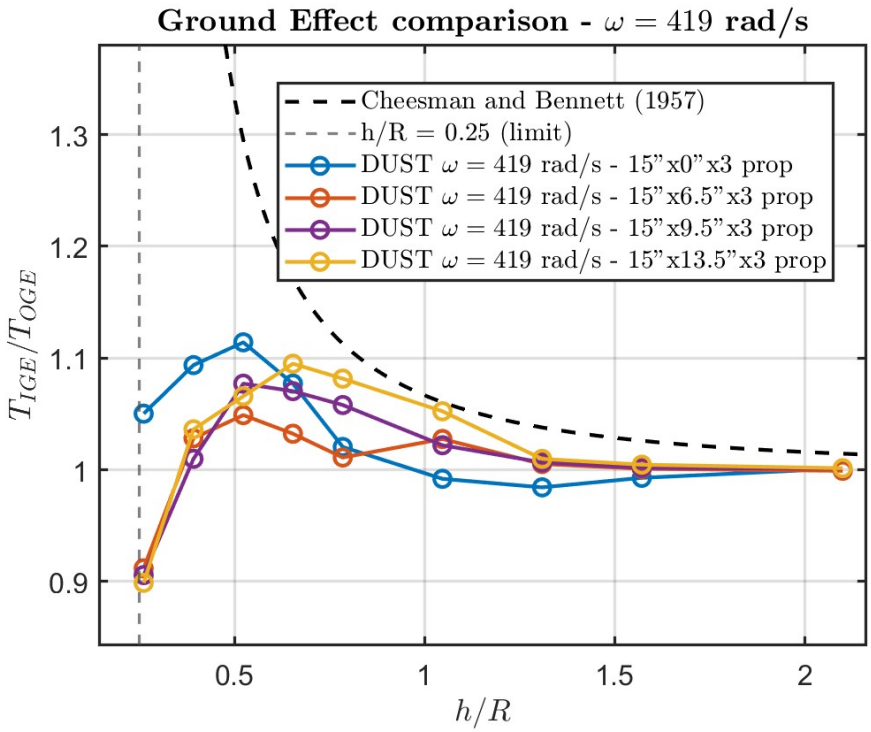

Figure 5.14: Ground effect comparison: normalized thrust versus h/R for all four propellers at 4000 rpm.

The updated results confirm that, once the propellers are thrust-matched, the low-pitch configurations exhibit a stronger sensitivity to the ground effect, whereas the high-pitch propeller shows only minor thrust amplification near the surface. As shown in Figure 5.14, the 15"×0" configuration (blue line) approaches more closely the analytical trend of Cheeseman and Bennett (1957), indicating a stronger dependence of the induced flow on ground proximity. Conversely, the intermediate and high-pitch propellers (6.5", 9.5", and 13.5") display a progressively weaker variation of $T_{\mathrm{IGE}}/T_{\mathrm{OGE}}$ with h/R, consistent with a reduced mirror-plane interaction.

It should be noted that the Cheeseman and Bennett correlation was originally developed for large-scale helicopter rotors in hover, assuming an ideal and uniformly loaded actuator disk. In the present case of small, high-speed propellers, the flow is dominated by tip vortices, compressibility, and nonuniform inflow, effects not captured by the classical model. Nevertheless, the general trend holds: low-pitch propellers, with a more vertically oriented induced flow, experience stronger ground-effect thrust augmentation, whereas high-pitch configurations produce a more axial, diffused wake and a weaker response.

5.6 Flow Field Visualization in ParaView

To better understand the aerodynamic mechanisms responsible for the thrust variation observed in Figure 5.14, the induced velocity field of the baseline propeller (15"×13.5"×3) was analyzed and visualized using ParaView.

Starting from the numerical results previously obtained with the DUST solver, a dedicated post-processing stage was performed to extract the flow field data around the rotor. This analysis focuses on three representative cases:

1. **h = 0.05 m** – corresponding to $h/R \simeq 0.26$, representing the *in-ground-effect* condition, where the rotor operates in close proximity to the ground plane;
2. **h = 0.1524 m** – corresponding to $h/R \simeq 0.8$, representing an *intermediate height*, where partial ground interference still affects the induced flow;
3. **h = 0.4 m** – corresponding to $h/R \simeq 2.1$, representing the *out-of-ground-effect (OGE)* condition.

In DUST, the procedure was implemented through the following analysis block in the `dust_post.in` file:

```
analysis = {
  type      = flow_field
  name      = volume_test

  start_res = 1
  end_res   = 51
  step_res  = 1
  format    = vtk
  average   = F
  variable  = Velocity

  n_xyz     = (/ 50, 50, 50 /)
  min_xyz   = (/-0.3, -0.3, 0.0 /)
  max_xyz   = (/ 0.3,  0.3, 0.5 /)
}
```

This setup defines a cubic domain extending from -0.3 m to $+0.3$ m in both the x and y directions, and from $z = 0$ (ground plane) up to $z = 0.5$ m. The field is discretized over a uniform grid of $50 \times 50 \times 50$ points, providing sufficient spatial resolution to capture the main induced–flow features around the rotor. The selected variable is the instantaneous velocity vector, exported at each iteration between time steps 1 and 51, with outputs saved in `.vtk` format for subsequent visualization in ParaView. The resulting dataset was saved in `.vtu` format and subsequently imported into ParaView for visualization.

Within ParaView, a vertical plane was selected through the rotor axis using the `Slice` filter, in order to inspect the local velocity vectors along the central section of the flow. The `Glyph` filter was then applied to represent the velocity vectors' direction and magnitude, while the background color map corresponds to the velocity magnitude distribution. An example of the computational grid and the selected visualization plane is shown in Figure 5.15.

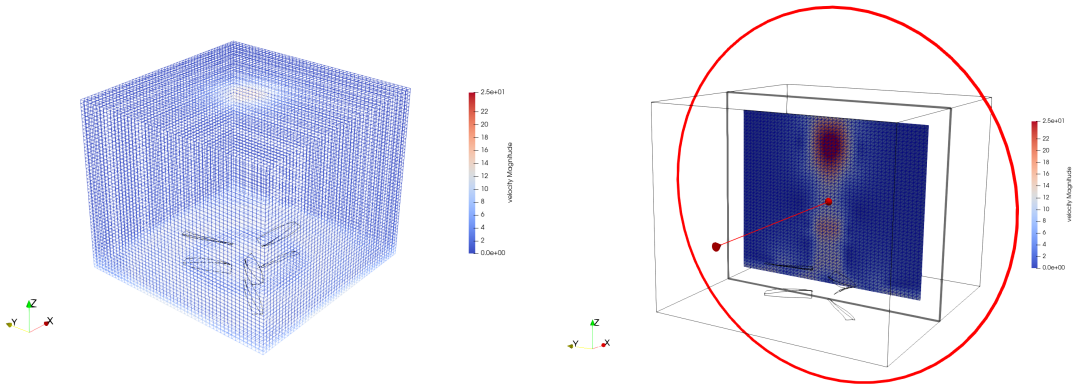

(a) Sampling grid used in DUST for the case $h = 0.05$ m.

(b) Slice plane visualization.

Figure 5.15: Example of post-processing setup for velocity field extraction and visualization.

To better understand the relationship between the induced flow and the thrust generation mechanism, the post–processing was extended to all ground–clearance configurations by plotting the *vertical velocity component* v_z instead of the total velocity magnitude. This quantity provides a more physically meaningful description, since only the vertical component of the induced velocity contributes directly to

the propeller thrust. According to the momentum–theory formulation, the thrust can be expressed as:

$$T = \rho A_{\text{eff}} \overline{v_z}^2,$$

where ρ is the air density, A_{eff} is the effective flow area, and $\overline{v_z}$ is the mean vertical induced velocity through the rotor disk. Analyzing the v_z field thus enables a direct connection between the local flow characteristics and the corresponding thrust ratio $T_{\text{IGE}}/T_{\text{OGE}}$.

The following section presents and discusses the results for the three selected ground–clearance cases, emphasizing the evolution of the vertical velocity field and its correlation with the experimentally observed $T_{\text{IGE}}/T_{\text{OGE}}$ variations.

1. h = 0.05 m ($h/R \simeq 0.26$) – Strong Ground Effect:

At this very low clearance, the rotor operates in strong ground–effect conditions, where the induced flow is significantly altered by the proximity of the surface. The following figures provide an overview of the velocity field obtained in ParaView, highlighting the structure of the wake and its interaction with the ground plane.

Velocity levels (v_z). The analysis of the vertical velocity component v_z was performed using a fixed scale of [−15,0] m/s, where negative values indicate downward flow (toward the ground). At this very low clearance, the downward motion is strongly weakened: most of the region beneath the rotor shows $|v_z|$ between 2 and 6 m/s, while only localized areas along the axis reach peaks of about 10 m/s. Large zones near the surface exhibit almost stagnant or even slightly upward flow ($|v_z| \approx 0$ m/s), indicating strong recirculation and energy dissipation due to wall–bounded interaction. This condition explains the reduction in thrust ($T_{\text{IGE}}/T_{\text{OGE}} < 1$), as a significant portion of the induced momentum is diverted radially instead of contributing to vertical lift.

Wake topology and near–ground interaction. The downward jet strikes the ground and expands radially, forming a wide low–velocity region beneath the rotor. This deflection increases the effective flow area and lowers the mean induced velocity, reducing the axial momentum available for thrust. Localized recirculation near the blade tips and weak upward reversal along the axis indicate partial dissipation of the induced flow energy.

Implication on $T_{\text{IGE}}/T_{\text{OGE}}$. The reduction of axial momentum and the strong

redistribution of the flow result in a lower thrust coefficient, consistent with the smaller $T_{\mathrm{IGE}}/T_{\mathrm{OGE}}$ ratios observed in Figure 5.14.

A detailed view of the near–ground interface (Figure 5.17) reveals strong upward motion and localized vortices beneath the blade tips, produced by the interaction between the impinging jet and the solid surface.

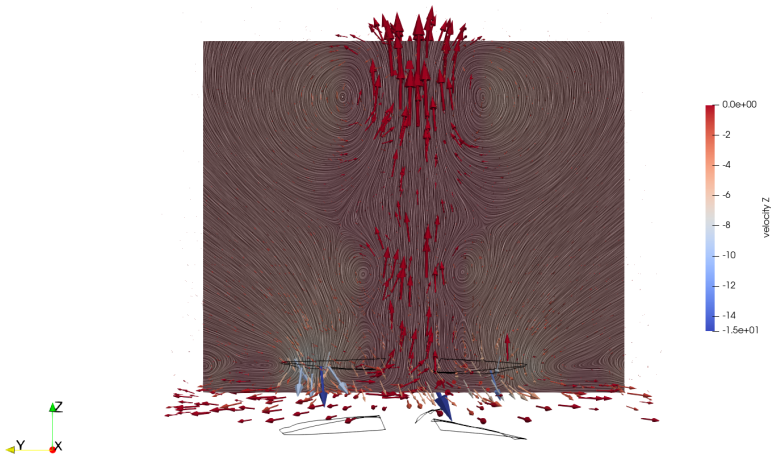

Figure 5.16: Overview of the velocity field for the baseline propeller at $h = 0.05$ m ($h/R \simeq 0.26$). Streamlines and color map show the lateral expansion of the induced jet and the broad low–velocity region formed near the ground.

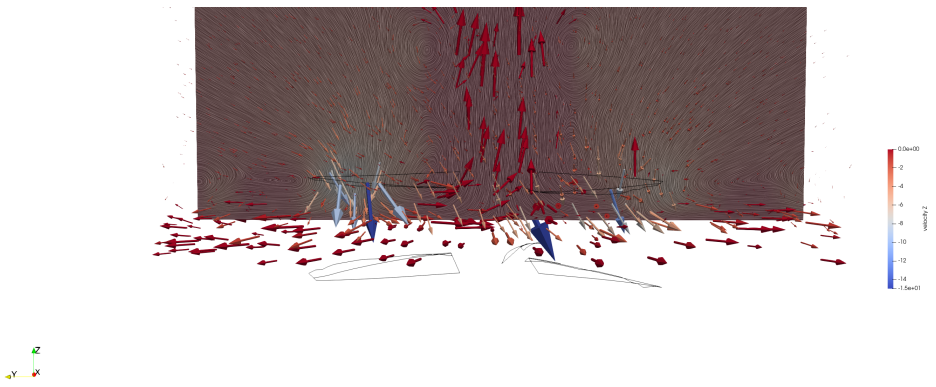

Figure 5.17: Detailed view of the interface region below the propeller at $h = 0.05$ m.

2. $h = 0.1524$ m $(h/R \simeq 0.8)$ – Intermediate Height

At this intermediate clearance, the propeller transitions between the near–ground and free–flight regimes. The following visualization illustrates how the wake structure progressively recovers its vertical alignment while still experiencing partial interaction with the ground reflection.

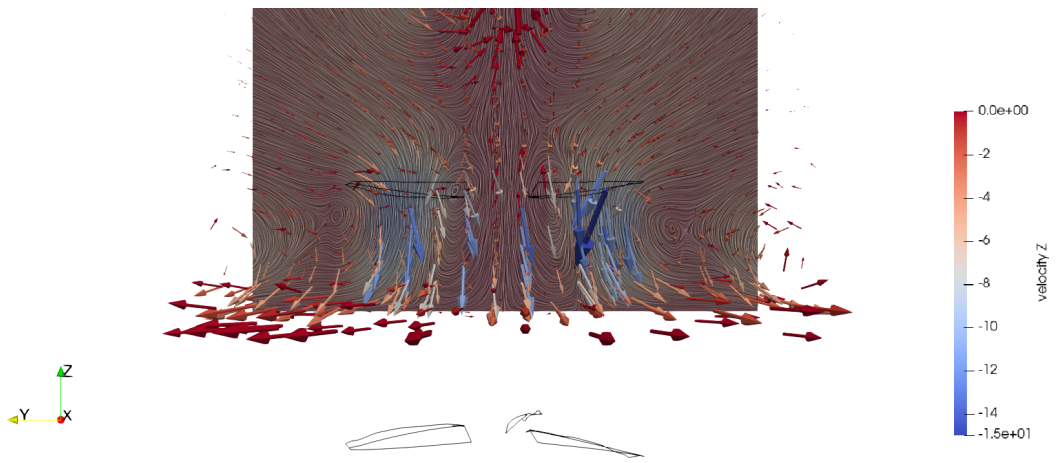

Figure 5.18: Velocity field at intermediate height ($h = 0.1524$ m), showing partial interaction between the wake and the ground.

Velocity levels (v_z). The axial core exhibits $|v_z|$ values between 10 and 13 m/s, surrounded by an annular region with moderate downward flow (5 to 9 m/s). Near the surface, the reflected motion produces localized upward components ($|v_z| \approx 0$ m/s) and weak recirculation. This distribution confirms the partial loss of axial momentum and explains the moderate thrust increase ($T_{\mathrm{IGE}}/T_{\mathrm{OGE}} > 1$) typical of this transitional regime.

Wake topology and near–ground interaction. The wake progressively recovers a vertical orientation, with limited radial expansion compared to the near–ground case. The reduced wall influence allows partial detachment of the induced flow, leading to a more coherent downward jet. Residual interaction with the mirror vortex system remains visible near the axis but is considerably weaker.

Implication on $T_{\mathrm{IGE}}/T_{\mathrm{OGE}}$. This intermediate condition corresponds to a moderate enhancement of thrust, with $T_{\mathrm{IGE}}/T_{\mathrm{OGE}}$ slightly above unity. The improvement arises from a partial recovery of axial induced velocity while retaining some ground–induced confinement of the flow.

3. $h = 0.4$ m $(h/R \simeq 2.1)$ – Out of Ground Effect

Finally, at a clearance large enough to suppress any wall interference, the propeller operates under fully out–of–ground–effect conditions. The flow evolves freely and reproduces the nominal induced–velocity pattern predicted by momentum theory.

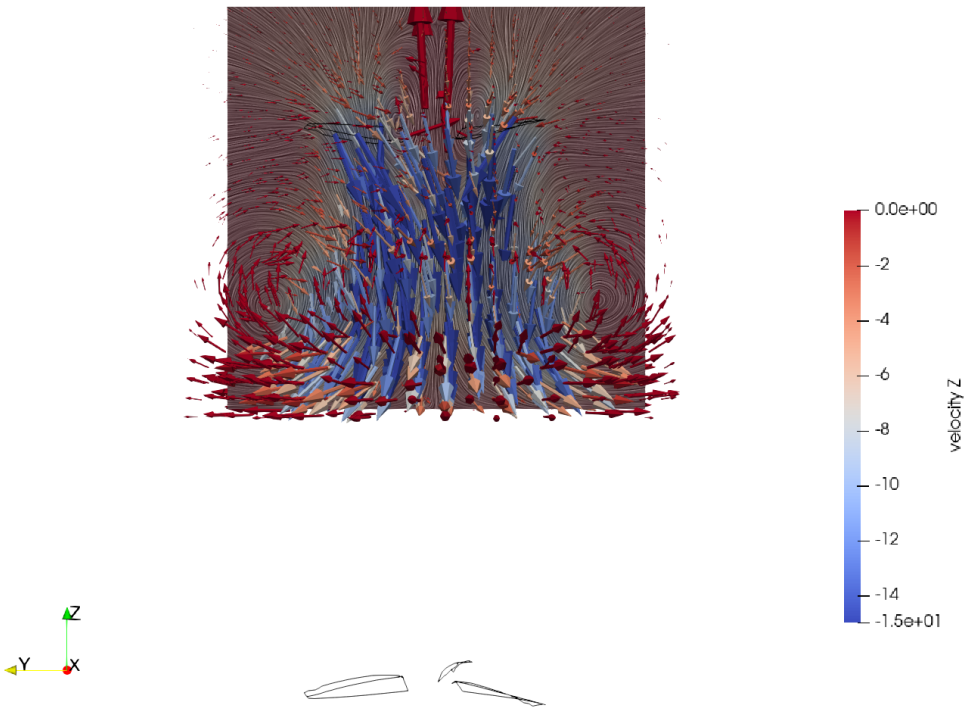

Figure 5.19: Velocity field in out–of–ground–effect condition ($h = 0.4$ m), showing a free, axisymmetric wake.

Velocity levels (v_z). The out–of–ground–effect jet shows: core values $|v_z| \simeq 12$ to 15 m/s along the axis and an annular region with $|v_z| \simeq 6$ to 10 m/s.. These higher $|v_z|$ levels are consistent with the OGE reference where $T_{\mathrm{IGE}}/T_{\mathrm{OGE}} \approx 1$.

Wake topology and near–ground interaction. At this distance, the wake evolves as a free, axisymmetric jet, with negligible wall interference. The flow fully recovers the nominal out–of–ground–effect condition.

Implication on $T_{\mathrm{IGE}}/T_{\mathrm{OGE}}$. The thrust coefficient matches the nominal out–of–ground–effect value T_{OGE}, representing the baseline condition for comparison with the lower–height cases.

5.6.1 Correlation between velocity field and thrust ratio

Although the observed trends in velocity magnitude and thrust ratio may appear counterintuitive at first glance, they are fully consistent with the classical theory of ground effect. In fact, the apparent discrepancy between the local velocity levels visualized in ParaView and the corresponding $T_{\mathrm{IGE}}/T_{\mathrm{OGE}}$ values can be explained by considering the integral nature of the thrust generation process.

While the flow visualization highlights local variations of the induced velocity, the thrust depends on the overall momentum flux through the rotor disk, which can be expressed as:

$$T = \rho A_{\mathrm{eff}} \overline{v_z}^2,$$

where A_{eff} is the effective flow area and $\overline{v_z}$ is the mean vertical velocity component. Depending on the height above ground, the balance between induced velocity and flow area changes significantly, leading to the three characteristic regimes summarized below:

- **Out of Ground Effect (OGE)** – $h = 0.4$ m**,** $T_{\mathrm{IGE}}/T_{\mathrm{OGE}} \approx 1.0$
  - The rotor operates in free air, unaffected by wall interference.
  - The induced jet is narrow, well–collimated, and aligned with the rotor axis.
  - The vertical velocity component reaches its maximum values ($|v_z| \simeq 14$ m/s), concentrated in a small core region.
  - Although the local velocities are high, the effective flow area is limited and the total momentum flux (and thus the thrust) equals the nominal out–of–ground condition.

- **Intermediate Height** – $h = 0.1524$ m**,** $T_{\text{IGE}}/T_{\text{OGE}} > 1.0$
  - The downward jet begins to interact with the ground, but without complete blockage.
  - The flow decelerates slightly ($|v_z| \approx 8 \div 10$ m/s) while expanding laterally.
  - The partial confinement of the flow increases the static pressure beneath the rotor, effectively reducing the induced power requirement.
  - The combined effect of a larger effective area A_{eff} and moderate induced velocity leads to an overall thrust augmentation.

- **Strong Ground Effect** – $h = 0.05$ m**,** $T_{\text{IGE}}/T_{\text{OGE}} < 1.0$
  - At very low clearance, the induced jet impinges directly on the surface and is deflected radially outward.
  - The vertical velocity component nearly vanishes below the disk ($v_z \approx 0$), and recirculating regions of reversed flow appear near the blade tips.
  - A large portion of the induced energy is redirected horizontally rather than contributing to vertical momentum.
  - As a result, the useful axial momentum flux decreases, leading to a reduction in thrust despite the visually complex and energetic flow field.

In summary, plotting the vertical velocity field v_z proved essential to interpret the ground–effect behavior in physical terms, since v_z directly represents the portion of the induced flow that contributes to thrust generation. By visualizing its spatial distribution, it becomes possible to clearly relate local flow mechanisms, such as jet confinement, ground reflection, and recirculation, to the measured variations of $T_{\text{IGE}}/T_{\text{OGE}}$.

This approach thus provides a more intuitive and quantitative understanding of how proximity to the ground alters the balance between induced momentum and thrust production.

5.7 Sensitivity to Rotational Speed

Following the analysis of pitch and twist effects, a complementary investigation was conducted to assess the influence of the rotational speed on the ground effect. The objective was to isolate the impact of the angular velocity ω on the thrust generation mechanisms of the baseline propeller (15"x13.5"x3), keeping the geometric parameters unchanged.

Figure 5.20 presents the variation of the thrust and the thrust ratio $T_{\mathrm{IGE}}/T_{\mathrm{OGE}}$ with angular velocity ω for different ground clearances.

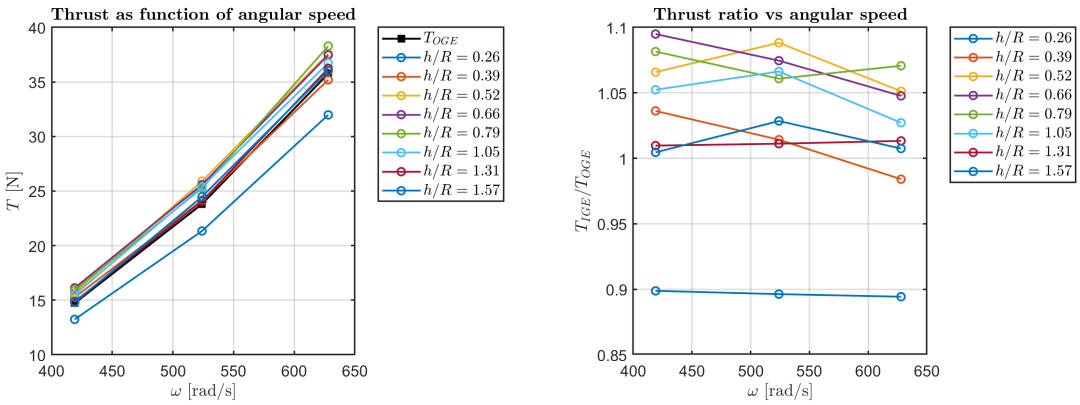

(a) Thrust as a function of ω for different clearances.

(b) Ratio $T_{\mathrm{IGE}}/T_{\mathrm{OGE}}$ versus ω.

Figure 5.20: Numerical results obtained with *DUST* for the APC propeller.

Consistent with momentum theory, the thrust increases approximately with the square of the rotational speed. However, at the smallest clearances, the DUST results underestimate the expected thrust enhancement, yielding values lower than those obtained at larger h/R. For $h/R \geq 0.8$, the results become consistent across all angular velocities and progressively converge toward the OGE condition as the clearance increases.

The ratio $T_{\mathrm{IGE}}/T_{\mathrm{OGE}}$ confirms that the ground effect primarily depends on the geometric clearance parameter h/R, exhibiting only a weak sensitivity to the rotational speed, an observation in agreement with the analytical correlation of Cheeseman and Bennett.

The overall trends observed from the DUST simulations are consistent with those reported by Zhu *et al.* (2023) [20], who investigated the ground effect behavior of single and staggered rotors. Their results confirmed that thrust generally increases as the rotor approaches the ground, although the magnitude of this enhancement strongly depends on the rotor configuration and the resulting wake–ground interactions. In particular, Zhu *et al.* highlighted that factors such as rotor spacing, geometry, and local flow turbulence can significantly alter the aerodynamic behavior near the ground, leading to deviations from the idealized analytical trends at low clearances ($h/R < 0.5$).

These observations are in line with the present findings, which similarly indicate a complex dependence of the induced flow structure on the clearance ratio h/R.

5.8 Comparison Between BEMT and DUST

To evaluate the consistency between the low–fidelity analytical model and the mid–fidelity numerical solver, a direct comparison is performed between the corrected BEMT implementation (described in Section 3) and the DUST simulations. Both analyses refer to hover conditions for the APC 15”×13.5”×3 propeller at $\omega = 419$ rad/s (4000 RPM). The DUST setup reproduces the same radial discretization and geometric parameters used in the BEMT model, ensuring a coherent basis for comparison.

The comparison is carried out in terms of the non-dimensional elemental thrust coefficient, defined as:

$$dC_T = \frac{dT}{\frac{1}{2}\rho(\Omega R)^2 \pi R^2}.$$

This formulation follows the same convention adopted in Section 3, allowing a consistent and scale–independent evaluation of the radial load distribution predicted by both models.

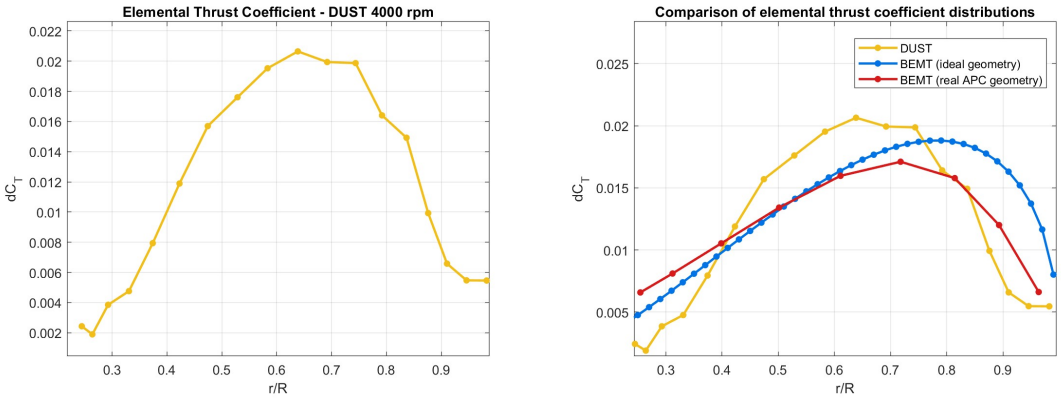

(a)Elemental thrust coefficient distribution predicted by DUST.

(b) Comparison among DUST, BEMT (ideal geometry), and BEMT (real APC geometry).

Figure 5.21: Spanwise distribution of the non–dimensional elemental thrust coefficient $dC_T(r/R)$ at $\omega = 419$ rad/s. The left plot shows the isolated DUST prediction, while the right plot compares it against both BEMT formulations, highlighting the effects of the Prandtl correction and the real blade geometry.

Figure 5.21 shows the spanwise evolution of the non–dimensional thrust coefficient predicted by the two methods. The corrected BEMT model (including Prandtl's tip–loss and real APC geometry) exhibits a maximum value of approximately $dC_T = 0.016$ at $r/R = 0.71$, while the DUST simulation predicts a slightly higher peak of $dC_T = 0.026$ located at $r/R = 0.65$. Both curves display the expected decay of aerodynamic loading toward the blade tip, consistent with finite–blade effects. The DUST profile is slightly smoother in the outer span, reflecting the influence of wake–induced velocity and viscous dissipation.

To provide a quantitative comparison, the global performance coefficients predicted by the two solvers are summarized in Table 5.5. The differences in total thrust and torque remain below 3% across all operating conditions, confirming the consistency between the low– and mid–fidelity approaches.

Overall, the good correlation between the two datasets confirms that the corrected BEMT implementation captures the main aerodynamic features of the propeller. The DUST solver refines these results by resolving the wake dynamics and the viscous tip–loss effects, offering a physically richer yet consistent prediction framework.

ω [rad/s]	**Thrust [N]**			**Torque [Nm]**			**Power [W]**		
	BEMT$_{\mathbf{corr}}$	**DUST**	**Diff. [%]**	**BEMT$_{\mathbf{corr}}$**	**DUST**	**Diff. [%]**	**BEMT$_{\mathbf{corr}}$**	**DUST**	**Diff. [%]**
419.0	17.48	17.10	−2.2	0.475	0.489	+3.0	199.08	204.93	+2.9
524.0	27.35	27.05	−1.1	0.742	0.761	+2.6	388.85	398.42	+2.5
628.0	39.28	39.54	+0.7	1.065	1.092	+2.5	669.07	686.42	+2.6

Table 5.5: Comparison between the corrected BEMT model (**BEMT$_{\mathbf{corr}}$**) and DUST simulations for the APC 15×13.5×3 propeller in hover.

5.9 Comparison with Multirotor Studies

To further interpret the non-monotonic behavior observed in the thrust ratio $T_{\mathrm{IGE}}/T_{\mathrm{OGE}}$ at small clearances, a comparative analysis was conducted between the present DUST results and experimental data from studies on multirotor configurations. Although the present work focuses on a single high-pitch propeller, the aerodynamic interaction mechanisms governing ground proximity are analogous to those observed in multirotor systems, particularly in hover conditions. Two key reference works were considered: Kan *et al.* (2019) [30] and Li *et al.* (2015) [4].

In the study by Kan *et al.* (2019), the authors experimentally analyzed the ground-effect behavior of a quadrotor UAV in both hover and forward flight conditions. Their investigation compared several analytical formulations, including the classical model by Cheeseman and Bennett (1957) and the empirical correlation by Hayden (1976) [30], expressed as:

$$\frac{T_{\mathrm{IGE}}}{T_{\mathrm{OGE}}} = \left(0.9926 + \frac{0.15176}{(h/R)^2}\right)^{2/3} \tag{5.3}$$

The comparison revealed that, contrary to the monotonically increasing trend predicted by Cheeseman and Bennett, the experimental thrust ratio decreases as the rotor approaches the ground, before gradually tending to unity for $h/R > 1$. This behavior, shown in Figure 5.22, is qualitatively similar to that obtained with DUST.

Analogous conclusions were reported by Li *et al.* (2015) [4], who developed an empirical model for autonomous landing applications of quadrotors. In their formulation, the thrust ratio is defined as:

$$\frac{T_{\mathrm{in}}}{T_{\mathrm{out}}} = b_i - k_i \left(\frac{R}{4h}\right)^2 \tag{5.4}$$

where $b_i = 0.985$ and $k_i = 1.680$ are coefficients identified experimentally in hovering conditions. Also in this case, the trend observed experimentally shows a reduction of $T_{\mathrm{IGE}}/T_{\mathrm{OGE}}$ near the ground, supporting the behavior predicted by the DUST simulations with the single high-pitch propeller.

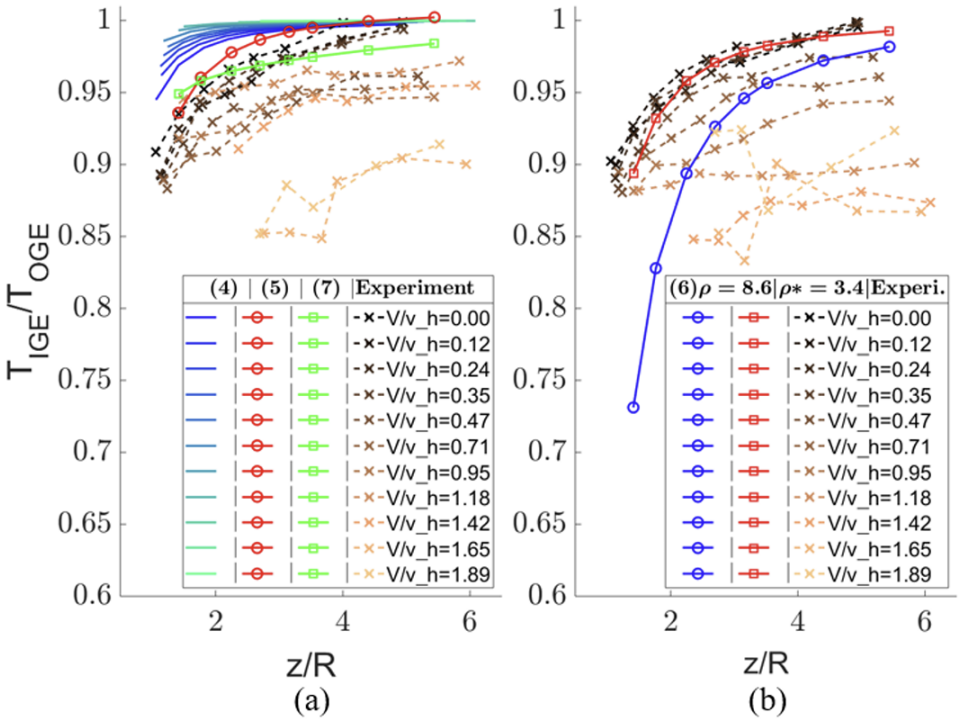

Figure 5.22: (a) Evaluation of Cheeseman & Bennett (4), Hayden (5), and Sánchez-Cuevas *et al.* (7) models; (b) Evaluation of Li *et al.* (2015) [4] model. The comparison highlights that both experimental datasets show a decreasing trend of $T_{\mathrm{IGE}}/T_{\mathrm{OGE}}$ as the clearance h/R decreases.

Building on these considerations, Kan *et al.* (2019) [30] proposed a simplified analytical formulation for the estimation of the thrust ratio in hover conditions, expressed as:

$$\frac{T_{\mathrm{IGE}}}{T_{\mathrm{OGE}}} = 1 - \frac{3R}{25h} \tag{5.5}$$

This expression was superimposed on the DUST predictions and compared with both the classical Cheeseman–Bennett model and the empirical relation by Li

et al. (2015) reported in Equation (5.4). As illustrated in Figure 5.23, the DUST results reproduce the same qualitative behavior observed in experiments, with a slight reduction in thrust at small clearances and a progressive convergence to unity as h/R increases.

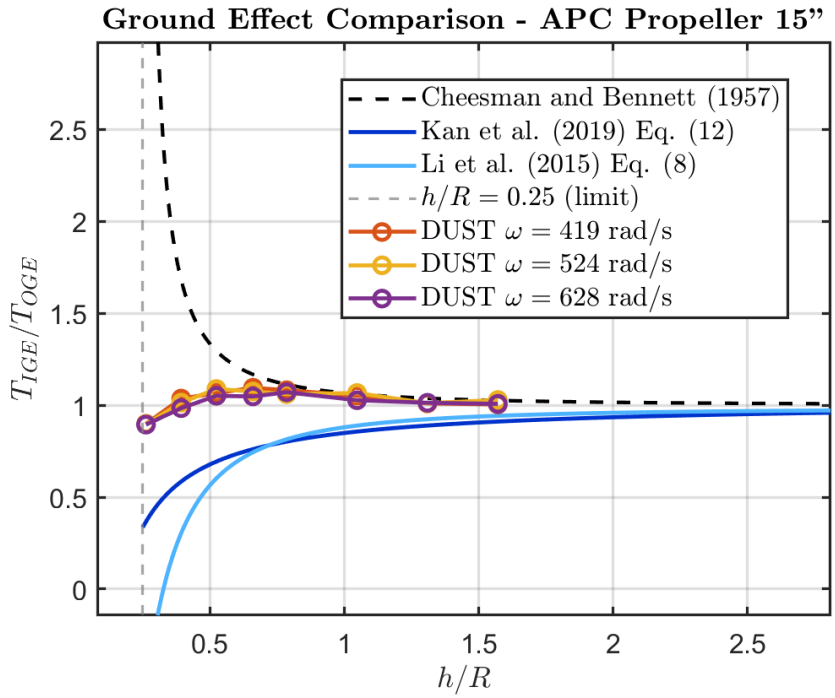

Figure 5.23: Comparison between DUST simulations and empirical models from the literature.

Overall, the results obtained with DUST show a non-monotonic evolution of the thrust ratio at small clearances, a behavior consistent with the experimental evidence reported for multirotor platforms in the literature. In particular, Kan *et al.* (2019) [30] and Li *et al.* (2015) [4] both observed that, contrary to the classical prediction of Cheeseman and Bennett, the ground effect may locally reduce the generated thrust as the rotor approaches the ground.

This thrust reduction is primarily attributed to complex flow mechanisms such as induced-flow recirculation, vortex–surface interactions, and wake distortion near the mirror plane. These effects intensify at small clearances, where the induced velocity field becomes highly nonlinear and sensitive to viscous and ground-interaction phenomena that are only partially captured by potential-flow solvers.

Nevertheless, despite the geometric and physical differences between a single propeller and multirotor configurations, the numerical results obtained here exhibit strikingly similar trends to those observed experimentally for quadrotors operating at comparable high pitch conditions. This agreement reinforces the reliability of DUST in capturing the dominant aerodynamic features of the ground effect, while highlighting the sensitivity of the phenomenon to both geometric and viscous factors at low h/R values.

5.10 Torque and Power Analysis

Following the thrust analysis, the torque and power predictions obtained from *DUST* were examined to further assess the solver's capability in reproducing the aerodynamic behavior of the propeller. Torque and power are directly related through the rotational speed ω, and both quantities provide additional insight into the overall aerodynamic performance and efficiency of the rotor system. The numerical results were first compared with the manufacturer's reference data for the out of ground effect (OGE) configuration, and subsequently analyzed as a function of the ground clearance h/R.

ω [rad/s]	Q_{IGE} [Nm] at different h/R							
	0.26	0.39	0.52	0.66	0.79	1.05	1.31	1.57
419.0	0.498	0.572	0.641	0.644	0.625	0.596	0.575	0.558
524.0	0.777	0.870	0.996	0.992	0.963	0.922	0.887	0.867
628.0	1.053	1.221	1.387	1.409	1.394	1.330	1.267	1.229

Table 5.6: Steady-state torque (Q_{IGE}) at different ω and h/R.

ω [rad/s]	P_{IGE} [W] at different h/R							
	0.26	0.39	0.52	0.66	0.79	1.05	1.31	1.57
419.0	208.66	239.69	268.69	269.69	261.74	251.46	240.90	234.36
524.0	406.26	455.16	521.09	518.91	503.89	482.11	463.40	453.27
628.0	661.47	766.82	870.83	884.85	875.31	835.01	795.57	774.53

Table 5.7: Steady-state power (P_{IGE}) at different ω and h/R.

The trends of torque and power with angular velocity ω are illustrated in Figures 5.24. At lower clearances ($h/R < 0.7$), both quantities are slightly higher than in OGE, while at larger clearances the differences progressively vanish. Since power is defined as $P = Q\omega$, the non dimensional ratios $P_{\text{IGE}}/P_{\text{OGE}}$ and $Q_{\text{IGE}}/Q_{\text{OGE}}$ are expected to coincide for a given ω, as also observed in the present results.

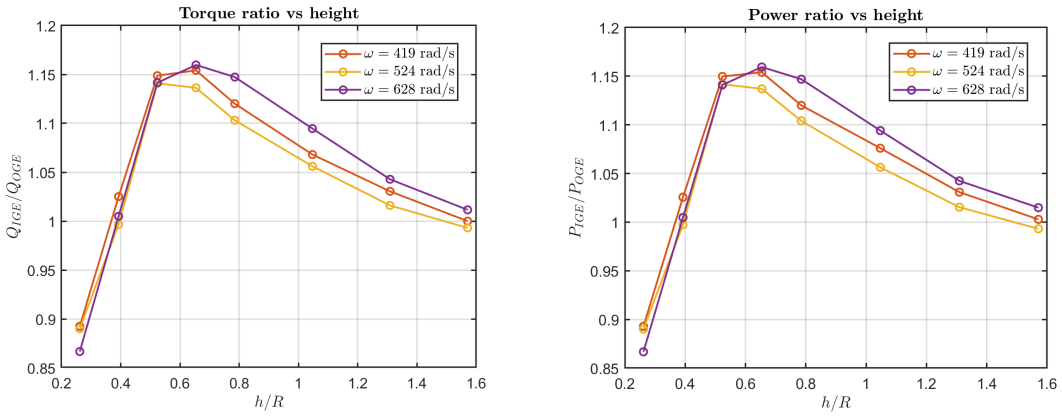

(a) Torque ratio as a function of ω.

(b) Power ratio as a function of ω.

Figure 5.24: Variation of torque (left) and power (right) with ω for different h/R.

The overall behavior of both torque and power is consistent with findings reported in the literature. In particular, Gilad *et al.* (2019) [31] investigated the aerodynamic performance of a flexible rotor operating in extreme ground effect, showing that the power ratio $P_{\text{IGE}}/P_{\text{OGE}}$ approaches unity as the normalized height h/R increases, indicating the progressive disappearance of the ground influence beyond $h/R \simeq 1.5$. A similar trend is observed in the present DUST simulations: as h/R increases, both $Q_{\text{IGE}}/Q_{\text{OGE}}$ and $P_{\text{IGE}}/P_{\text{OGE}}$ tend toward unity, suggesting that the propeller progressively approaches the hover condition as the ground clearance increases.

For small clearances ($h/R < 0.7$), however, a local overprediction of the power ratio is observed, with a distinct peak at the lowest h/R values. This deviation from the expected monotonic behavior likely arises from numerical limitations of the potential–flow formulation near the mirror plane, where the induced velocity field becomes highly nonlinear and sensitive to discretization. Similar effects have been reported in other mid-fidelity simulations of near-wall propeller aerodynamics, highlighting the need for viscous corrections when modeling ground–effect phenomena at very small clearances.

Chapter 6

Experimental results

This chapter presents the experimental results obtained from the test campaign described in Chapter 4, where the setup, propeller model, measurement apparatus, and throttle sequence were detailed. The experiments were conducted in two distinct phases: first with the open propeller configuration (without duct), and subsequently with the ducted propeller configuration. The latter phase aimed to investigate the aerodynamic influence of the duct on propeller performance; however, this topic is not discussed here, as it represents the focus of a complementary study within the same research project. Accordingly, the present analysis focuses on the open propeller case.

The experimental campaign provided thrust and torque measurements for both in ground effect (IGE) and out of ground effect (OGE) conditions over different propeller-ground distances. For each rotational speed setting, the propeller–wall spacing was varied from 0.05 m to 0.70 m, and multiple repetitions were performed to assess measurement repeatability, resulting in a total of 48 tests. Data post processing was carried out in MATLAB. Since the resulting datasets corresponded to slightly different rotational speeds, a linear interpolation was applied to estimate thrust and torque values at selected reference RPMs for both IGE and OGE conditions. This procedure ensured consistent comparisons across all operating points and enabled the computation of nondimensional quantities such as the thrust ratio $T_{\mathrm{IGE}}/T_{\mathrm{OGE}}$ and torque ratio $Q_{\mathrm{IGE}}/Q_{\mathrm{OGE}}$.

6.1 Validation in OGE Conditions

Before analyzing the effect of ground proximity, the experimental results obtained in out-of-ground (OGE) conditions were compared against the manufacturer's

nominal data to verify the accuracy of the measurement setup.

Table 6.1 reports the measured thrust and torque values obtained in OGE conditions for all test repetitions. Each dataset corresponds to a distinct throttle sequence, and the RPM values refer to the steady-state averages for each throttle setting. The results show good repeatability among the four runs, confirming the consistency of the measurement system.

Test	**RPM**	**Thrust [N]**	**Torque [Nm]**	**Voltage [V]**	**Current [A]**
OGE–1	2396	5.77	0.543	24.82	10.31
	3156	10.21	0.397	24.96	9.58
	3991	16.10	0.591	24.84	18.74
	4313	19.08	0.788	24.55	28.58
	4864	25.59	0.917	24.48	41.46
OGE–2	2329	5.69	0.567	24.95	10.77
	3173	10.09	0.391	24.97	9.39
	3961	16.16	0.598	24.84	19.17
	4307	19.10	0.791	24.68	28.71
	4925	24.64	0.895	24.50	39.63
OGE–3	2276	4.65	0.191	25.24	3.88
	3208	10.04	0.40	25.17	7.77
	3213	10.00	0.382	25.16	9.35
	4049	16.37	0.395	25.02	18.90
	4571	22.27	0.782	24.81	29.88
	4992	25.45	0.894	24.71	38.77
OGE–4	2290	4.76	0.194	25.24	3.83
	3204	10.04	0.396	25.18	7.74
	3215	10.05	0.383	25.16	9.40
	4035	15.87	0.59	25.02	18.94
	4547	21.49	0.794	24.79	31.30
	4936	24.58	0.883	24.71	39.65

Table 6.1: Experimental OGE results for the open propeller configuration.

From the manufacturer's static performance chart for the APC 15"×13.5"×3 propeller, the expected hover performance at zero forward velocity is reported as follows:

- $T = 10.01$ N and $Q = 0.298$ Nm at 3000 rpm;
- $T = 17.85$ N and $Q = 0.517$ Nm at 4000 rpm;
- $T = 27.95$ N and $Q = 0.796$ Nm at 5000 rpm.

The experimental OGE measurements exhibit an excellent agreement with these reference values, both in magnitude and trend, confirming the proper calibration of the test rig and the reliability of the acquisition procedure.

The rotational speed range investigated (approximately 2300–5000 rpm) was selected to ensure stable operation of the propulsion unit. Preliminary observations indicated that, at higher speeds ($\sim$ 6000 rpm), the HACKER A50-16S motor, directly coupled to the load cell, tended to overheat. This thermal buildup could have introduced measurement inaccuracies and potentially damaged the setup; for this reason, such operating conditions were deliberately avoided during the test campaign.

6.2 Performance in IGE Conditions

Following the validation of the *out-of-ground-effect* (OGE) results, the analysis was extended to investigate the influence of ground proximity on the propeller aerodynamic performance. The objective was to quantify how thrust and torque vary as the propeller approaches a solid wall, and to express this variation in nondimensional form through the ratios $T_{\mathrm{IGE}}/T_{\mathrm{OGE}}$ and $Q_{\mathrm{IGE}}/Q_{\mathrm{OGE}}$.

Since the experimental runs were performed independently for each ground clearance, the measured rotational speeds did not perfectly coincide among repetitions. To ensure a consistent comparison across different distances, the data were post–processed in MATLAB through a dedicated interpolation and averaging procedure. Linear interpolation was applied to all thrust and torque datasets, allowing the values to be evaluated at fixed reference speeds (3200, 4000, 4500, and 4900 rpm) for each height. This step minimized the influence of measurement scatter and enabled direct computation of the nondimensional ratios:

$$\frac{T_{\mathrm{IGE}}}{T_{\mathrm{OGE}}}, \qquad \frac{Q_{\mathrm{IGE}}}{Q_{\mathrm{OGE}}}.$$

The interpolation and ratio evaluation followed three main steps:

1. All OGE datasets were merged to define reference interpolation functions $T_{\mathrm{OGE}}(\mathrm{rpm})$ and $Q_{\mathrm{OGE}}(\mathrm{rpm})$.

2. For each clearance h, the corresponding IGE data were combined and interpolated independently, yielding $T_{\mathrm{IGE}}(\mathrm{rpm}, h)$ and $Q_{\mathrm{IGE}}(\mathrm{rpm}, h)$.

3. The ratios $T_{\mathrm{IGE}}/T_{\mathrm{OGE}}$ and $Q_{\mathrm{IGE}}/Q_{\mathrm{OGE}}$ were then evaluated at the four reference speeds.

A simplified version of the MATLAB implementation is reported below:

```
rpm_target = [3200, 4000, 4500, 4900];  % Reference speeds
T_OGE_fun = @(rpmq) interp1(all_rpm, all_T, rpmq, 'linear',
    'extrap');

for hh = 1:length(unique_h)
    idx = find([IGE.h] == unique_h(hh));
    T_IGE_fun{hh} = @(rpmq) interp1(all_rpm_h, all_T_h, rpmq
    , 'linear', 'extrap');
end

for i = 1:length(unique_h)
    for j = 1:length(rpm_target)
        Tige = feval(T_IGE_fun{i}, rpm_target(j));
        Toge = feval(T_OGE_fun, rpm_target(j));
        ratios(i,j) = Tige / Toge;
    end
end
```

An analogous routine was used for the torque data. Finally, the computed ratios were plotted as functions of the nondimensional clearance h/R, together with the analytical prediction of Cheeseman and Bennett (1957):

$$\frac{T_{\mathrm{IGE}}}{T_{\mathrm{OGE}}} = \frac{1}{1 - \left(\frac{1}{4h/R}\right)^2},$$

which represents the ideal ground–effect amplification for a uniformly loaded actuator disk. This theoretical curve was superimposed on the experimental data for direct comparison. The interpolation yielded mean thrust and torque values for each clearance, which were subsequently averaged across repetitions. Table 6.2 summarizes the interpolated IGE results for the four selected reference speeds. These averaged values served as the basis for the computation of the nondimensional ratios and for the comparison with the OGE baseline.

THRUST RATIO $(T_{\mathrm{IGE}}/T_{\mathrm{OGE}})$				
h/R	**3200 rpm**	**4000 rpm**	**4500 rpm**	**4900 rpm**
0.26	1.0366	1.0690	1.0571	1.0546
0.39	0.9994	1.0737	1.0708	1.0673
0.52	0.9952	1.0618	1.0391	1.0857
0.67	0.9970	1.0674	1.0819	1.1016
0.79	0.9846	1.0709	1.0131	1.0769
1.05	0.9815	1.0314	1.0321	1.0533
1.31	0.9914	1.0670	1.0734	1.0909
1.57	0.9884	1.0806	1.0358	1.0582
2.89	0.9934	1.0559	1.0809	1.0583
3.67	0.9917	1.0245	1.0703	1.0442

TORQUE RATIO $(Q_{\mathrm{IGE}}/Q_{\mathrm{OGE}})$				
h/R	**3200 rpm**	**4000 rpm**	**4500 rpm**	**4900 rpm**
0.26	1.3158	0.9978	0.9291	0.9399
0.39	1.0737	1.0088	0.9267	0.9353
0.52	1.0845	1.0211	0.9367	0.9384
0.67	1.0450	0.9942	0.8997	0.9383
0.79	1.0251	1.2791	0.9546	0.9207
1.05	1.0077	1.0187	0.9431	0.9529
1.31	0.9983	0.9999	0.9434	0.9324
1.57	1.0067	1.0048	0.9614	0.9557
2.89	1.0037	1.0413	0.8932	0.9891
3.67	0.9949	1.0163	0.9020	0.9880

Table 6.2: Interpolated nondimensional thrust and torque ratios in IGE conditions for the four reference rotational speeds (3200, 4000, 4500, and 4900 rpm).

The resulting trends are illustrated in Figure 6.1, which shows the evolution of the thrust ratio $T_{\mathrm{IGE}}/T_{\mathrm{OGE}}$ as a function of the nondimensional clearance h/R. A noticeable thrust increase is observed primarily at low rotational speed (3200 rpm), while at higher speeds the ratio slightly decreases as the propeller approaches the wall. This non–monotonic behavior suggests that, at small clearances, recirculation and stand–induced interference partially counteract the classical ground–effect amplification predicted by the analytical model of Cheeseman and Bennett (1957). Such behavior has been similarly observed in experimental investigations of small-scale rotors operating near solid boundaries [30], [4].

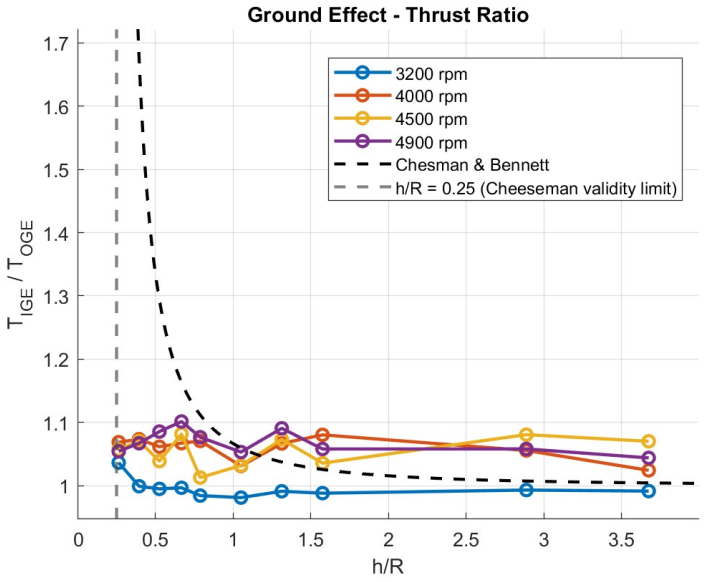

Figure 6.1: Experimental results for the open propeller configuration: variation of the thrust ratio $T_{\mathrm{IGE}}/T_{\mathrm{OGE}}$ with h/R at different rotational speeds.

Similarly, Figure 6.2 illustrates the evolution of the torque ratio $Q_{\mathrm{IGE}}/Q_{\mathrm{OGE}}$ as a function of the nondimensional clearance h/R.

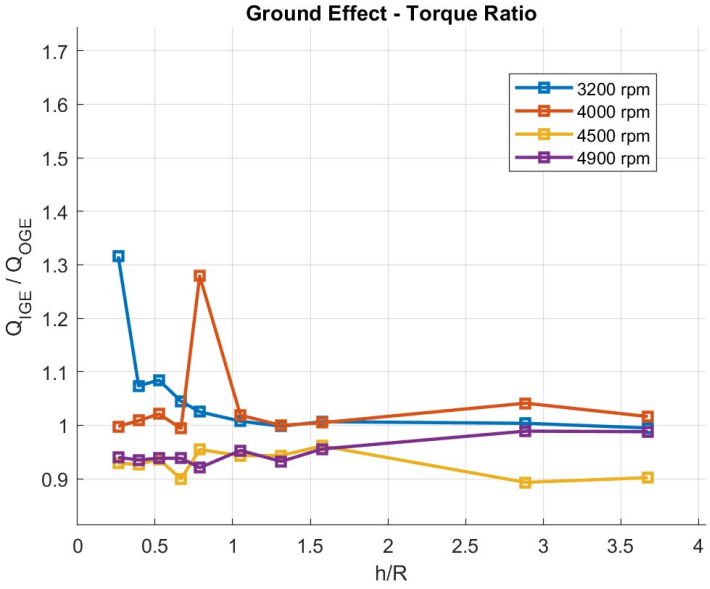

Figure 6.2: Experimental results for the open propeller configuration: variation of the torque ratio $Q_{\mathrm{IGE}}/Q_{\mathrm{OGE}}$ with h/R at different rotational speeds.

Unlike the thrust ratio, the torque exhibits higher variability across the tested conditions, particularly at low clearance levels, where localized recirculation and unsteady inflow may increase measurement uncertainty. At low rotational speed (3200 rpm), the torque ratio occasionally exceeds unity, whereas at higher speeds it generally remains close to or slightly below one. This behavior indicates that, as the propeller approaches the wall, viscous and installation effects contribute to a moderate reduction in propulsive efficiency, a trend consistent with prior rotor–ground interaction studies [30], [4].

6.3 Comparison with Numerical Predictions

To further assess the predictive capability of the DUST solver, Figures 6.3 and 6.4 compare the experimental measurements with the corresponding numerical results for both thrust and torque ratios. The comparison focuses on three representative rotational speeds (**3200**, **4500** and **4900 rpm**), for which a detailed post-processing of the numerical output was performed, including the evaluation of the standard deviation of thrust and torque after removal of the initial transient.

The numerical model reproduces well the overall trend of the thrust ratio, capturing the non-monotonic behaviour characterized by a local increase around $h/R \approx 0.66$, followed by a progressive decay toward unity as the rotor moves away from the ground. The amplitude of the variation predicted by DUST is slightly lower than that observed experimentally.

For the torque ratio, the correlation between experiments and numerical predictions is less consistent. While DUST generally predicts a smooth rise in $Q_{\mathrm{IGE}}/Q_{\mathrm{OGE}}$ at small clearances followed by a gradual decay toward unity as h/R increases, the experimental measurements exhibit a noticeably larger variability. This discrepancy is most pronounced at low clearance ratios, where the experiments show a pronounced peak around $h/R \approx 0.7$ before decreasing and asymptotically approaching the out-of-ground-effect value. This behaviour suggests a stronger sensitivity of the torque response to near-wall flow interactions and possible viscous or support-induced losses not captured by the potential-flow formulation used in DUST.

It is also worth noting that the numerical predictions show only minor differences across the three rotational speeds considered (3200, 4500 and 4900 rpm). All cases follow nearly identical trends for both thrust and torque ratios.

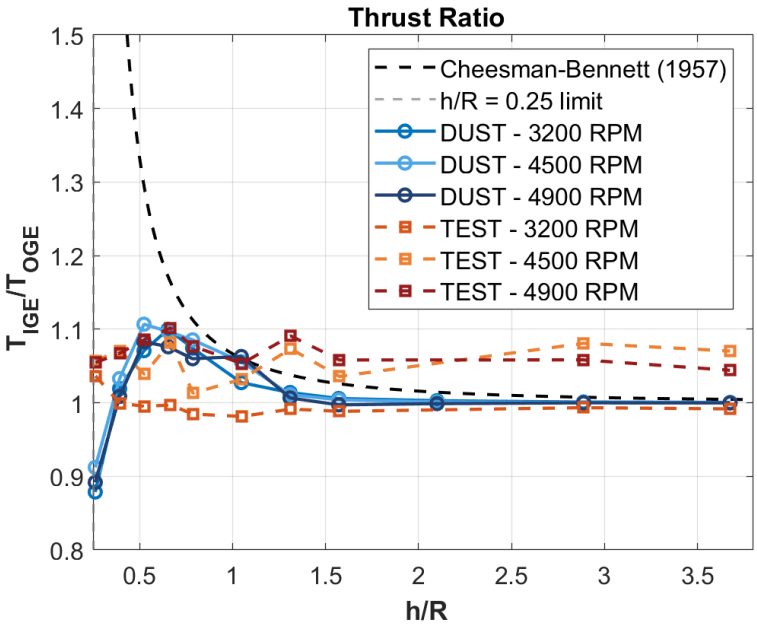

Figure 6.3: Comparison between experimental data (TEST) and numerical predictions (*DUST*) for the variation of the thrust ratio $T_{\mathrm{IGE}}/T_{\mathrm{OGE}}$ with h/R.

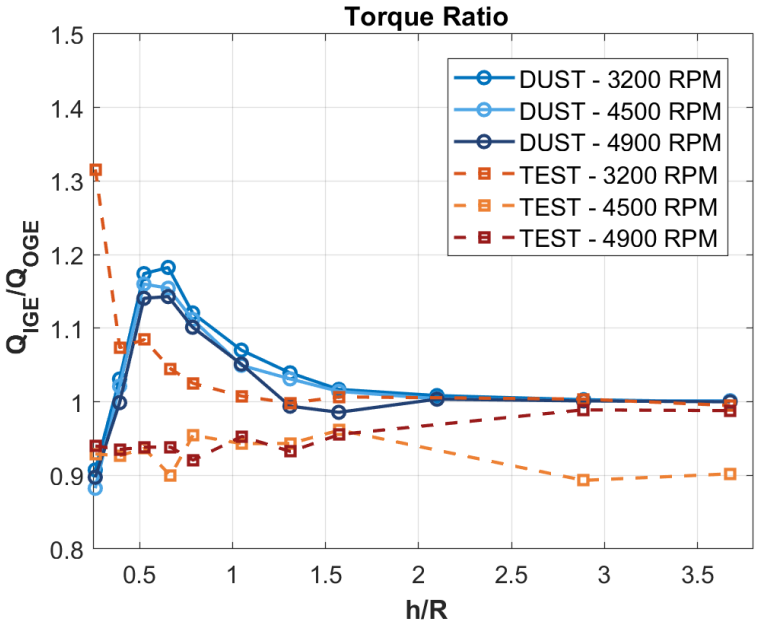

Figure 6.4: Comparison between experimental data (TEST) and numerical predictions (*DUST*) for the variation of the torque ratio $Q_{\mathrm{IGE}}/Q_{\mathrm{OGE}}$ with h/R.

Overall, the comparison demonstrates that DUST is capable of reproducing the main aerodynamic trends observed experimentally. The solver provides reliable mid–fidelity predictions for $h/R > 0.8$, where wall induced disturbances are less pronounced, whereas deviations at smaller clearances highlight the increasing influence of viscous and installation effects beyond the scope of the present model.

6.3.1 Standard Deviation Analysis

In order to quantify the unsteady behaviour of the DUST simulations and to assess the convergence towards a statistically steady state, a standard deviation analysis was performed for three representative rotational speeds: **3200 rpm**, **4500 rpm** and **4900 rpm**.

Each of the three analysed rotational speeds corresponds to a different angular velocity and therefore to a different physical time step used within the DUST simulation. For every case, DUST produces a sequence of output files, each containing the instantaneous values of thrust (F_z) and torque (M_z) evaluated at successive time steps of the unsteady solution.

Since the initial portion of each simulation includes the transient associated with wake roll-up and the establishment of a periodic regime, the first 1.5 rotor revolutions were systematically removed from the analysis. The cutoff time $t_{\min}$ was therefore computed as:

$$t_{\min} = 1.5\,T \qquad \text{with} \quad T = \frac{2\pi}{\Omega}.$$

The resulting values for each rotational speed are:

– **3200 rpm:**

$$\Omega = 335.10 \text{ rad/s}, \qquad T = \frac{2\pi}{335.10} = 0.01874 \text{ s},$$

$$t_{\min} = 1.5T = 1.5 \times 0.0187 = \mathbf{0.0281\ s}.$$

– **4500 rpm:**

$$\Omega = 471.24 \text{ rad/s}, \qquad T = \frac{2\pi}{471.24} = 0.0133 \text{ s},$$

$$t_{\min} = 1.5T = 1.5 \times 0.0133 = \mathbf{0.0199\ s}.$$

– **4900 rpm:**

$$\Omega = 512.13 \text{ rad/s}, \qquad T = \frac{2\pi}{512.13} = 0.0122 \text{ s},$$

$$t_{\min} = 1.5T = 1.5 \times 0.0122 = \mathbf{0.0184\ s}.$$

After removing all samples with $t < t_{\min}$, the remaining values were used to compute the **mean thrust and torque**:

$$\bar{T} = \frac{1}{N}\sum_{i=1}^{N} T_i, \qquad \bar{Q} = \frac{1}{N}\sum_{i=1}^{N} Q_i,$$

and their corresponding **standard deviations**:

$$\sigma_T = \sqrt{\frac{1}{N-1}\sum_{i=1}^{N}(T_i - \bar{T})^2}, \qquad \sigma_Q = \sqrt{\frac{1}{N-1}\sum_{i=1}^{N}(Q_i - \bar{Q})^2}.$$

Tables 6.3, 6.4 adn 6.5 summarize the mean values and standard deviations of T and Q for all the ground clearance ratios h/R and rotational speeds (3200, 4500 and 4900 rpm). The ratio $T_{\text{IGE}}/T_{\text{OGE}}$ and the percentage increment with respect to out-of-ground-effect (OGE) thrust are also included.

STEADY LOADS AND STANDARD DEVIATION – 3200 rpm						
h/R	$T_{\textbf{mean}}$ **[N]**	$T_{\textbf{std}}$ **[N]**	$Q_{\textbf{mean}}$ **[Nm]**	$Q_{\textbf{std}}$ **[Nm]**	$T_{\text{IGE}}/T_{\text{OGE}}$	ΔT **[%]**
0.26	8.289	0.181	0.3324	0.0063	0.904	-9.62%
0.39	9.469	0.187	0.3713	0.0041	1.032	+3.25%
0.52	9.643	0.129	0.3949	0.0150	1.051	+5.15%
0.67	9.730	0.283	0.3921	0.0159	1.061	+6.10%
0.79	9.473	0.217	0.3849	0.0088	1.033	+3.29%
1.05	9.307	0.135	0.3752	0.0061	1.015	+1.48%
1.31	9.268	0.071	0.3696	0.0046	1.011	+1.06%
1.57	9.235	0.078	0.3663	0.0053	1.007	+0.70%
2.09	9.223	0.079	0.3640	0.0054	1.006	+0.57%
2.89	9.205	0.078	0.3630	0.0060	1.004	+0.37%
3.67	9.202	0.077	0.3627	0.0060	1.003	+0.34%

Table 6.3: Mean thrust and torque, standard deviation and thrust ratio in IGE for 3200 rpm.

STEADY LOADS AND STANDARD DEVIATION – 4500 rpm						
h/R	$T_{\mathbf{mean}}$ **[N]**	$T_{\mathbf{std}}$ **[N]**	$Q_{\mathbf{mean}}$ **[Nm]**	$Q_{\mathbf{std}}$ **[Nm]**	$T_{\mathrm{IGE}}/T_{\mathrm{OGE}}$	ΔT [%]
0.26	17.687	0.350	0.6380	0.0129	0.939	-6.14%
0.39	20.135	1.278	0.7566	0.0610	1.068	+6.85%
0.52	20.302	0.527	0.7807	0.0307	1.077	+7.73%
0.67	20.247	0.253	0.7765	0.0250	1.074	+7.44%
0.79	19.998	0.238	0.7575	0.0186	1.061	+6.12%
1.05	19.606	0.169	0.7274	0.0104	1.040	+4.04%
1.31	19.258	0.388	0.7360	0.0134	1.022	+2.19%
1.57	19.181	0.403	0.7297	0.0153	1.018	+1.78%
2.09	19.138	0.403	0.7258	0.0158	1.016	+1.55%
2.89	19.116	0.398	0.7240	0.0158	1.014	+1.44%
3.67	19.110	0.399	0.7233	0.0160	1.014	+1.41%

Table 6.4: Mean thrust and torque, standard deviation, and thrust ratio in IGE for 4500 rpm.

STEADY LOADS AND STANDARD DEVIATION – 4900 rpm						
h/R	$T_{\mathbf{mean}}$ **[N]**	$T_{\mathbf{std}}$ **[N]**	$Q_{\mathbf{mean}}$ **[Nm]**	$Q_{\mathbf{std}}$ **[Nm]**	$T_{\mathrm{IGE}}/T_{\mathrm{OGE}}$	ΔT [%]
0.26	20.728	0.248	0.7579	0.0108	0.906	-9.45%
0.39	23.607	0.475	0.8600	0.0140	1.031	+3.13%
0.52	24.631	0.864	0.9379	0.0507	1.076	+7.61%
0.67	24.081	0.307	0.9110	0.0287	1.052	+5.20%
0.79	23.861	0.355	0.8881	0.0230	1.042	+4.24%
1.05	23.664	0.532	0.8603	0.0166	1.034	+3.38%
1.31	23.449	0.443	0.8452	0.0175	1.024	+2.44%
1.57	23.183	0.619	0.8402	0.0177	1.013	+1.28%
2.09	22.910	0.231	0.8577	0.0178	1.001	+0.09%
2.89	22.804	0.345	0.8546	0.0174	0.996	-0.38%
3.67	22.801	0.342	0.8541	0.0174	0.996	-0.39%

Table 6.5: Mean thrust and torque, standard deviation, and thrust ratio in IGE for 4900 rpm.

To better illustrate the behaviour captured by DUST, the standard deviation analysis is first presented for the lowest rotational speed (3200 rpm) to clearly illustrate the behaviour of the unsteady loads at a single operating condition. Subsequently, the curves for all three rotational speeds (3200, 4500 and 4900 rpm)

are shown together, allowing for a direct comparison of how the sensitivity to ground proximity evolves with rotor speed.

Figures 6.7a and 6.7b report the thrust and torque mean values together with their associated standard deviation ($\pm\sigma$). The variability is significantly larger at small ground clearance ratios, where the wake impinges on the wall and generates a strong unsteady recirculation. As h/R increases, both thrust and torque rapidly stabilize, and the standard deviation decreases accordingly.

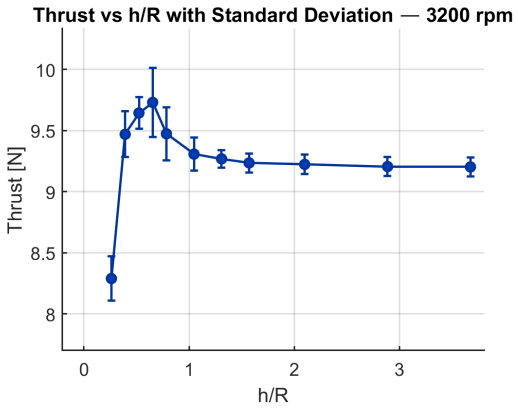

Figure 6.5: Thrust and standard deviation at 3200 rpm.

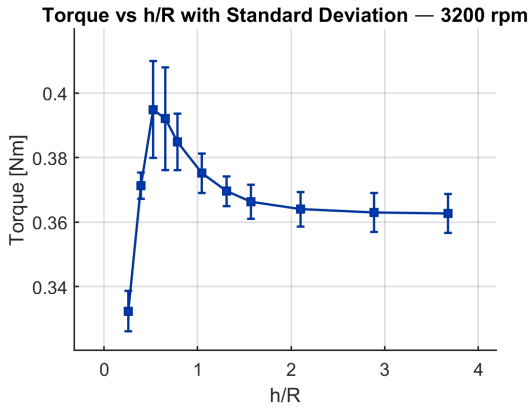

Figure 6.6: Torque and standard deviation at 3200 rpm.

Figure 6.7: Standard deviation analysis for the 3200 rpm case.

Once the behaviour of the fluctuations is clearly established for the 3200 rpm case, the comparison across all rotational speeds is presented in Figures 6.8a and 6.8b. Here the three curves (3200, 4500 and 4900 rpm) are superimposed to highlight how the magnitude of the aerodynamic fluctuations changes with increasing rotational speed.

To better quantify how the unsteady fluctuations vary with the rotor speed, the *relative standard deviation* was computed for both thrust and torque at each ground clearance ratio. It is defined as:

$$\sigma_T^{\%} = 100\,\frac{\sigma_T}{T_{\text{mean}}}, \qquad \sigma_Q^{\%} = 100\,\frac{\sigma_Q}{Q_{\text{mean}}}. \tag{6.1}$$

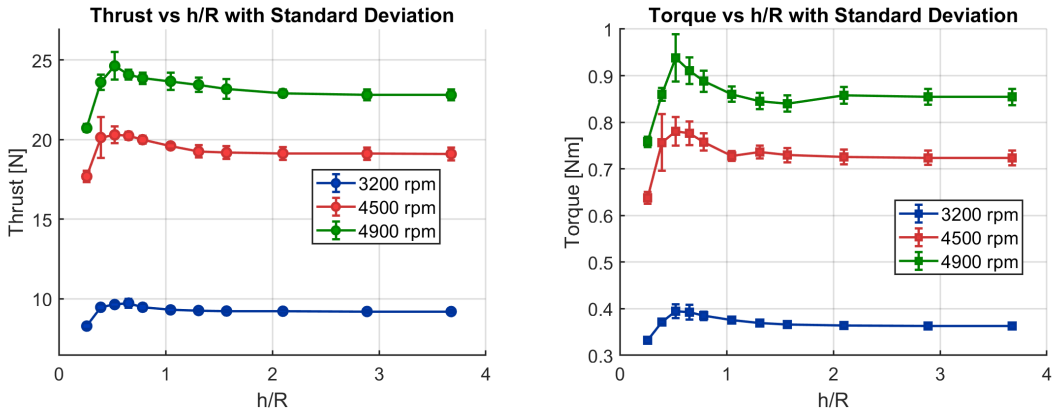

(a) Thrust. (b) Torque.

Figure 6.8: Comparison of thrust and torque variability.

Tables 6.6 illustrate the relative standard deviations for thrust and torque at all ground clearance ratios and for the three examined rotational speeds. This compact representation allows a direct comparison of the fluctuation levels across operating conditions, complementing the visual trends shown in Figures 6.8(a) and 6.8(b).

h/R	RPM					
	3200		**4500**		**4900**	
	σ_T [%]	σ_Q [%]	σ_T [%]	σ_Q [%]	σ_T [%]	σ_Q [%]
0.26	2.18	1.89	1.98	2.02	1.19	1.43
0.39	1.98	1.10	6.35	8.06	2.01	1.63
0.52	1.34	3.79	2.59	3.93	3.51	5.41
0.65	2.91	4.06	1.25	3.22	1.28	3.15
0.79	2.29	2.29	1.19	2.46	1.49	2.59
1.05	1.45	1.63	0.86	1.43	2.25	1.93
1.31	0.77	1.25	2.02	1.82	1.89	2.07
1.57	0.85	1.45	2.11	2.09	2.67	2.11
2.10	0.86	1.49	2.11	2.18	1.01	2.08
2.89	0.85	1.65	2.08	2.18	1.51	2.04
3.67	0.84	1.65	2.09	2.21	1.50	2.04

Table 6.6: Relative standard deviation of thrust and torque.

The relative standard deviations reported in Table 6.6 reveal several consistent trends regarding the intensity of the unsteady aerodynamic fluctuations. First, at all ground clearance ratios, the fluctuations tend to decrease as the rotational speed increases: the values at 3200 rpm are generally higher than those at 4500 and 4900 rpm. This behaviour reflects the stabilising effect of higher angular momentum, which makes the flow field more energetic and less susceptible to perturbations.

Across all rotational speeds, the largest relative deviations occur at the smallest clearance ratios, particularly in the range $h/R \approx 0.4$-0.7. In this region, both thrust and torque exhibit noticeable peaks (most prominently at 4500 rpm, where σ_T and σ_Q reach 6.35% and 8.06%, respectively). These elevated values confirm that strong non–stationary interactions develop when the induced flow becomes confined between the rotor and the ground.

As the rotor moves away from the ground, the relative fluctuations rapidly decrease. For $h/R > 1$, the values of $\sigma_T^{\%}$ and $\sigma_Q^{\%}$ fall within narrow numerical intervals:

- **Thrust:** typically between **0.7% and 2.2%**;
- **Torque:** typically between **1.2% and 2.2%**.

These fluctuations also show only a weak dependence on the rotational speed. For $h/R > 2$, the variability becomes nearly constant, consistent with the approach to out-of-ground-effect conditions.

At small clearances, torque displays a stronger sensitivity than thrust to near-wall flow perturbations. In general:

- $\sigma_T^{\%}$ remains below **3–4%**, with the exception of a single peak of about **6%** at 4500 rpm and $h/R = 0.39$;
- $\sigma_Q^{\%}$ can reach values as high as **5–8%** at small ground clearances.

This confirms that torque is more affected by local variations in the induced velocity field and by the vortical structures generated in the confined shear layer.

Overall, the data confirm that unsteady aerodynamic activity is most intense at intermediate ground proximities and diminishes both with increasing distance from the ground and with increasing rotational speed.

Chapter 7

Conclusions and Future Work

This thesis presented an integrated numerical and experimental investigation of the *ground effect* acting on a small propeller in hover, representative of the propulsion systems employed in multirotor drones and eVTOL platforms. Following a critical review of the classical models (Momentum Theory, BET/BEMT, and vortex-based methods) and the traditional correlations developed for helicopter rotors, a dedicated test bench was designed and built to measure thrust, torque, and power at different heights above the ground. In parallel, a numerical analysis was performed using the **DUST** solver, a mid-fidelity free-vortex code capable of capturing the induced flow field and wake behavior. The combination of experimental and numerical results allowed the assessment of the limitations of classical correlations at small scales and provided quantitative insights into how geometric and kinematic parameters affect the *ground effect* on small fixed-pitch propellers, highlighting trends and dependencies that differ from those observed in large-scale rotor systems.

The results clearly show that the proximity to the ground significantly alters the aerodynamic behavior of the propeller, influencing thrust, torque, and power in ways that diverge from traditional theoretical predictions. In particular:

- **Dependence on normalized height h/R.** The increase in thrust observed in ground effect follows the general trend predicted by theory, but its magnitude differs notably from classical formulations derived for large rotors, especially at low h/R ratios.
- **Limitations of existing analytical models.** The Cheesman–Bennett correlation, which remains the only widely adopted analytical formulation for ground–effect prediction, proves inadequate at small scales and systematically

overestimates the thrust at very low clearances. This limitation is not unexpected, since the model was originally derived for helicopter rotors characterized by low pitch, collective control, and the presence of a central hub, operating in a flow environment fundamentally different from that of small fixed–pitch multirotor propellers.

– **Role of geometry and rotational speed.** The intensity of the ground effect is sensitive to the propeller pitch, twist distribution, and rotational speed. Low-pitch configurations exhibit more pronounced effects, confirming that helicopter-based correlations cannot be directly scaled to small drone propellers.

– **Numerical–experimental consistency.** DUST simulations exhibited good agreement with the laboratory measurements, successfully capturing both the thrust variation in ground effect and the associated induced–flow behavior. This confirms that, despite its mid-fidelity nature, the solver provides a reliable representation of the ground–interaction mechanisms relevant to small propellers.

7.1 Comparison with Literature Models

The comparison with classical ground effect correlations (in particular the Cheeseman–Bennett model) highlights that existing analytical formulations are not directly applicable to small-scale, fixed-pitch propellers. Systematic discrepancies emerge at low h/R, where classical models overpredict the thrust increase and fail to capture the strong radial deflection and momentum dissipation observed experimentally. These limitations are expected, since the available correlations were originally developed for helicopter rotors with collective pitch control and fundamentally different wake structures. For small multirotor propellers, no analytical model currently provides a reliable prediction of ground effect performance, especially in the very near-ground regime.

While BEMT can still serve as a low-fidelity baseline, it requires significant corrections for inflow, Reynolds number, and wake contraction. Conversely, vortex-based mid-fidelity solvers such as DUST reproduce the induced-flow physics more accurately and offer a practical compromise between model fidelity and computational cost. Overall, the present results confirm that ground effect modeling for small propellers remains an open research topic, with a clear need for new physics and based correlations specifically tailored to UAV-scale rotors.

7.2 Limitations and Future Works

The present study investigated the ground effect aerodynamics of a single isolated propeller in hover, operating above a rigid and idealized ground plane. The analysis did not include multirotor interactions, lateral confinement, or the effects of non-uniform or porous surfaces. These assumptions define the controlled framework of the work and allow a clear interpretation of the physical mechanisms, but inherently limit the direct applicability of the results to more complex UAV configurations.

Building on these considerations, several developments emerge as natural extensions of the work:

1. **Extension to coaxial and multirotor systems.** Future investigations should include mutual interference effects such as fountain flow, and partial ground effect, which are highly relevant for multirotor drones.

2. **Ground effect aerodynamics in realistic environments.** Additional experiments and simulations considering non-ideal surfaces (rough, porous, sloped) and partially confined conditions would enable a more complete characterization of the operating scenarios typically encountered by UAVs.

3. **High-fidelity validation of the wake structure.** Selected RANS/LES simulations could be used to validate and refine the mid-fidelity DUST model, particularly in the very near-ground regime where strong radial deflection and recirculation occur.

4. **Reconstruction and experimental testing of the Hovera eVTOL.** Although this thesis was motivated by the ground effect behaviour observed on the **Hovera** platform developed by the RMIT student team, a direct replication could not be performed due to the lack of detailed propeller geometry and the time required for accurate CAD reconstruction. Completing this reconstruction and conducting dedicated experiments on the Hovera system would allow a direct validation of the numerical results presented in this work.

Bibliography

[1] RMIT GoFly Team. *Hovera: Progress Report for the GoFly Prize*. Tech. rep. https://rmitgofly.wordpress.com/wp-content/uploads/2021/07/progress-report-gofly-2021.pdf. Melbourne, Australia: RMIT University, 2021 (cit. on p. 3).

[2] S. A. Conyers, M. J. Rutherford, and K. P. Valavanis. «An Empirical Evaluation of Ground Effect for Small-Scale Rotorcraft». In: *IEEE International Conference on Robotics and Automation (ICRA)* (2018). https://doi.org/10.1109/ICRA.2018.8461035 (cit. on pp. 5, 7, 18–20, 76).

[3] J. Xu, J. Yu, X. Lu, Z. Long, Y. Xu, and H. Sun. «Aerodynamic Performance and Numerical Analysis of the Coaxial Contra-Rotating Propeller Lift System in eVTOL Vehicles». In: *Mathematics* (2024). Vol. 12, No. 7, Pag. 1056, https://doi.org/10.3390/math12071056 (cit. on pp. 5, 6, 18, 25–28).

[4] D. Li, Y. Zhou, Z. Shi, and G. Lu. «Autonomous Landing of Quadrotor Based on Ground Effect Modelling». In: *Proceedings of the 34th Chinese Control Conference (CCC)* (2015). Pag. 5647–5652, https://doi.org/10.1109/ChiCC.2015.7260509 (cit. on pp. 5, 97–99, 106, 108).

[5] A. Delgado-Gutiérrez, P. Marzocca, D. Cárdenas-Fuentes, O. Probst, and A. Montesinos Castellanos. «An Efficient Implementation of the GPU-Accelerated Single-Step and Simplified Lattice Boltzmann Method for Irregular Fluid Domains». In: *Physics of Fluids* (2022). Vol. 34, No. 12, Pag. 125123, https://doi.org/10.1063/5.0127270 (cit. on p. 6).

[6] J. D. Anderson. «Fundamentals of Aerodynamics». In: (2017). Chap. 9: Momentum Theory, https://link.springer.com/content/pdf/10.1007/978-3-319-55164-7_9.pdf (cit. on p. 8).

[7] W. Johnson. «Blade Element Theory (BET)». In: *Introduction to Helicopter and Tiltrotor Flight Simulation*. Chap. 7, Pag. 245–280, https://link.springer.com/content/pdf/10.1007/978-3-319-55164-7_7.pdf. Springer, 2015 (cit. on pp. 9, 10).

[8] J. G. Leishman. *Principles of Helicopter Aerodynamics*. 2nd. https://assets.cambridge.org/052166/0602/sample/0521660602WS.pdf. Cambridge University Press, 2006 (cit. on pp. 12, 33, 82).

[9] W. Johnson. *Helicopter Theory*. https://books.google.com.au/books?id=SgZheyNeXJIC&pg=PA1. Dover Publications, 1980 (cit. on pp. 12, 33).

[10] G. Georgiev. «Blade Element–Momentum Aerodynamic Model of a Helicopter Rotor Operating at Low-Reynolds Numbers in Ground Effect». In: *Aviation* (2025). Vol. 29, No. 2, https://doi.org/10.3846/aviation.2025.23587 (cit. on pp. 12, 13, 18, 20, 21).

[11] D. Tyagi and S. Schmitz. «Glauert's Optimum Rotor Disk Revisited – A Calculus of Variations Solution and Exact Integrals for Thrust and Bending Moment Coefficients». In: *Wind Energy Science* (2025). Vol. 10, Pag. 451–460, https://doi.org/10.5194/wes-10-451-2025 (cit. on p. 13).

[12] H. Lee, B. Sengupta, M. S. Araghizadeh, and R. S. Myong. «Review of Vortex Methods for Rotor Aerodynamics and Wake Dynamics». In: *Advances in Aerodynamics* (2022). Vol. 4, No. 1, Pag. 11, https://doi.org/10.1186/s42774-022-00111-3 (cit. on pp. 13, 14, 16, 17).

[13] H. Abedi, L. Davidson, and S. Voutsinas. «Vortex Method Application for Aerodynamic Loads on Rotor Blades». In: *Proceedings of the EWEA 2013 Conference*. https://publications.lib.chalmers.se/records/fulltext/185701/local_185701.pdf. Vienna, Austria, 2013 (cit. on pp. 14–16).

[14] A. Matus-Vargas, G. Rodriguez-Gomez, and J. Martinez-Carranza. «Ground Effect on Rotorcraft Unmanned Aerial Vehicles: A Review». In: *CEAS Aeronautical Journal* (2021). Vol. 12, Pag. 111–128, https://doi.org/10.1007/s11370-020-00344-5 (cit. on p. 18).

[15] J. Lighthill. «A Simple Fluid-Flow Model of Ground Effect on Hovering». In: *Journal of Fluid Mechanics* (1979). Vol. 93, No. 4, Pag. 745–758, https://doi.org/10.1017/S0022112079002032 (cit. on pp. 19, 24, 47).

[16] P. Sanchez-Cuevas, G. Heredia, and A. Ollero. «Characterization of the Aerodynamic Ground Effect and Its Influence in Multirotor Control». In: *International Journal of Aerospace Engineering* (2017). Vol. 2017, Pag. 1823056, https://doi.org/10.1155/2017/1823056 (cit. on pp. 21–23).

[17] H. Li, Z. Chen, and H. Jia. «Experimental Investigation on Hover Performance of a Ducted Coaxial-Rotor UAV». In: *Sensors* (2023). Vol. 23, No. 14, Pag. 6413, https://doi.org/10.3390/s23146413 (cit. on pp. 25, 26, 29–32, 61).

[18] F. Lucas. «Study of Contra-Rotating Coaxial Rotors in Hover: A Performance Model Based on Blade Element Theory Including Swirl Velocity». https://commons.erau.edu/db-theses/127. MA thesis. Daytona Beach, FL: Embry-Riddle Aeronautical University, 2007 (cit. on pp. 25, 33).

[19] T. Zhang, G. Qiao, D. A. Smith, G. N. Barakos, and A. Kusyumov. «Parametric Study of Aerodynamic Performance of Equivalent Ducted/Un-Ducted Rotors». In: *Aerospace Science and Technology* (2021). Vol. 117, Pag. 106984, https://doi.org/10.1016/j.ast.2021.106984 (cit. on pp. 25, 29).

[20] H. Zhu, S. Wei, H. Nie, Y. Du, and X. Wei. «Ground Effect on the Thrust Performance of Staggered Rotor System». In: *Drones* (2024). Vol. 8, No. 4, Pag. 118, https://doi.org/10.3390/drones8040118 (cit. on pp. 25, 95).

[21] W. Johnson. «A Quiet Helicopter for Air Taxi Operations». In: *AIAA Scitech 2020 Forum*. https://ntrs.nasa.gov/api/citations/20200000509/downloads/20200000509.pdf. NASA. Orlando, FL, USA, 2020 (cit. on p. 25).

[22] E. Branlard. *Wind Turbine Aerodynamics and Vorticity-Based Methods: Fundamentals and Recent Applications*. Chapter 13: Tip-Losses with Focus on Prandtl's Tip-Loss Factor, https://www.researchgate.net/publication/315858872_Tip-Losses_with_Focus_on_Prandlt's_Tip_Loss_Factor. Springer, 2017 (cit. on p. 40).

[23] S. F. Ramdin. «Prandtl Tip Loss Factor Assessed». Master's Thesis, Aerospace Engineering Faculty, Delft University of Technology, https://repository.tudelft.nl/file/File_8293b429-e8dc-430d-ba24-ca5c4274d7b0?preview=1. MA thesis. Delft, The Netherlands: Delft University of Technology, 2017 (cit. on p. 40).

[24] H. A. Oliveira, J. G. de Matos, L. A. dos S. Ribeiro, O. R. Saavedra, and J. R. P. Vaz. «Assessment of Correction Methods Applied to BEMT for Predicting Performance of Horizontal-Axis Wind Turbines». In: *Sustainability* (2023). Vol. 15, No. 8, Article 7021, https://doi.org/10.3390/su15087021 (cit. on p. 43).

[25] M. Tugnoli, D. Montagnani, M. Syal, G. Droandi, and A. Zanotti. «Mid-fidelity approach to aerodynamic simulations of unconventional VTOL aircraft configurations». In: *Aerospace Science and Technology* 118 (2021), p. 106804. DOI: 10.1016/j.ast.2021.106804 (cit. on p. 64).

[26] DUST Project. *DUST – An Aerodynamics Solution for Complex Configurations*. https://www.dust-project.org/. Accessed October 2025. 2025 (cit. on pp. 64, 65).

[27] DUST Group. *DUST Repository*. https://gitlab.com/dust_group/dust. Accessed October 2025. 2025 (cit. on pp. 64, 65).

[28] Politecnico di Milano. *DUST User Manual*. https://public.gitlab.polimi.it/DAER/dust/-/blob/master/doc/DUST_user_manual.pdf. Department of Aerospace Science and Technology. 2023 (cit. on pp. 65–68).

[29] Jielong Cai. «Changes in Propeller Performance Due to Ground and Partial Ground Proximity». http://rave.ohiolink.edu/etdc/view?acc_num=dayton1588164898961792. MA thesis. Dayton, Ohio: University of Dayton, 2020 (cit. on pp. 76, 79).

[30] X. Kan, J. Thomas, H. Teng, H. G. Tanner, V. Kumar, and K. Karydis. «Analysis of Ground Effect for Small-Scale UAVs in Forward Flight». In: *IEEE Robotics and Automation Letters* (2019). Vol. 4, No. 4, Pag. 3983–3990, https://doi.org/10.1109/LRA.2019.2928478 (cit. on pp. 97–99, 106, 108).

[31] Mor Gilad, Inderjit Chopra, and Omri Rand. «Performance Evaluation of a Flexible Rotor in Extreme Ground Effect». In: *AIAA SciTech Forum*. https://arc.aiaa.org/doi/10.2514/6.2019-1135. American Institute of Aeronautics and Astronautics. 2019. DOI: 10.2514/6.2019-1135 (cit. on p. 101).